STRANGENESS PRODUCTION IN AU+AU COLLISIONS AT $\sqrt{s_{NN}}$ = 19.6 GEV FROM STAR AT RHIC

Submitted in partial fulfilment of the requirements of the degree of

Doctor of Philosophy

by

Sameer Aslam
(1821PH11)

Under the supervision of

Dr. Neha Kiritkumar Shah

and co-supervision of

Dr. Arghya Choudhury

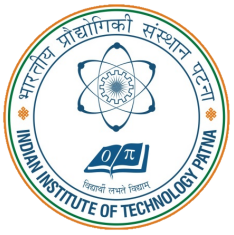

DEPARTMENT OF PHYSICS
INDIAN INSTITUTE OF TECHNOLOGY PATNA
BIHAR, INDIA - 801106, INDIA
December 2024

This page is intentionally left blank

This work is dedicated to

My beloved sister, Yasmeen Aslam

for her support, optimism, and love.

This page is intentionally left blank

भारतीय प्रोद्योगिकी संस्थान पटना
INDIAN INSTITUTE OF TECHNOLOGY PATNA
कनपा रोड, बिहटा, पटना-801106 [बिहार] भारत
Kanpa road, Bihta, Patna - 801106, Bihar, India

Date: 17/12/2024

CERTIFICATE OF APPROVAL

Certified that the thesis entitled **"Strangeness production in Au+Au collisions at $\sqrt{s_{NN}}$ = 19.6 GeV from STAR at RHIC"** submitted by **Mr. Sameer Aslam (Roll No. 1821ph11)** to Indian Institute of Technology Patna, for the award of the degree of Doctor of Philosophy has been accepted by the external examiners and that the student has successfully defended the thesis in the viva-voce examination held today i.e. **17/12/2024**

Dr. Raghavan K Easwaran
CHAIRPERSON of the DC/Viva-voce
HoD, Department of Physics
Indian Institute of Technology Patna

Dr. Neha Kiritkumar Shah
Supervisor
Department of Physics
Indian Institute of Technology Patna

Dr. Arghya Choudhury
Co-supervisor
Department of Physics
Indian Institute of Technology Patna

Dr. Jobin Jose
DC Member
Department of Physics
Indian Institute of Technology Patna

Dr. Devinder Yadav
DC Member
Departement of Physics
Indian Institute of Technology Patna

Dr. Utpal Roy
INTERNAL EXAMINER

Prof. Ankhi Roy
EXTERNAL EXAMINER

This page is intentionally left blank

DECLARATION BY THE SCHOLAR

I certify that:

- The work contained in this thesis is original and has been done by me under the guidance of my supervisor.
- The work has not been submitted to any other Institute for any degree or diploma.
- I have followed the guidelines provided by the Institute in preparing the thesis.
- I have conformed to the norms and guidelines given in the Ethical Code of Conduct of the Institute.
- Whenever I have used materials (data, theory, and text) from other sources, I have given due credit to them by citing them in the text of the thesis and giving their details in the reference section.
- The thesis has been checked by anti-plagiarism software.

Sameer Aslam

This page is intentionally left blank

INDIAN INSTITUTE OF TECHNOLOGY PATNA

Bihta, Patna

Certificate

This is to certify that the thesis entitled "**Strangeness production in Au+Au collisions at $\sqrt{s_{NN}}$ = 19.6 GeV from STAR at RHIC**", submitted by **Mr. Sameer Aslam** to Indian Institute of Technology Patna, is a record of bonafide research work under my supervision and I consider it worthy of consideration for the degree of Doctor of Philosophy of the Institute.

Neha 17/12/2024

Dr. Neha Kiritkumar Shah
Supervisor
Department of Physics
Indian Institute of Technology Patna

Arghya Choudhury 17.12.24

Dr. Arghya Choudhury
Co-supervisor
Department of Physics
Indian Institute of Technology Patna

This page is intentionally left blank

Acknowledgement

I am profoundly grateful to my supervisor, Dr. Neha Kiritkumar Shah, whose esteemed guidance and constant support have been influential throughout my academic journey. Her mentorship has shaped the direction of my research and significantly contributed to my scholarly development. Her rigorous evaluations and constructive feedback were invaluable in refining my thesis. Her open-minded approach and the freedom she granted me to explore various aspects of my research have been truly inspiring. I am immensely thankful for her dedication to providing the best possible guidance. I feel incredibly privileged to have had the opportunity to work under the guidance of Dr. Neha Kiritkumar Shah.

Sincere thanks also go to the members of my doctoral committee: Dr. Arghya Choudhury, Dr. Jobin Jose, Dr. Raghavan K Easwaran, and Dr. Devinder Yadav, with particular gratitude to Dr. Arghya Choudhury for his supportive role as co-supervisor. Dr. Choudhury's approachable and encouraging nature has greatly facilitated my academic endeavors and motivated me in my work.

I would like to thank all the STAR Physics Working Group (PWG) members for their discussions and suggestions that have helped in my analysis. Special thanks are due to past LFSUPC convenors Prof. Daniel Cebra, Dr. Daniel Brandenburg, Dr. Md Nasim, and current convenors Dr. Yue Hang Leung, Dr. Zaochen Ye, and Dr. Shuai Yang for their insightful suggestions. Further, my appreciation extends to Eugenia Khyzhniak, Ashik Iqbal, and Li-ke Liu for their indispensable support during my initial engagements with the QA board team in the STAR Collaboration. My experiences with the STAR collaboration have been enriched by the opportunity to interact with several experts, particularly within the LFSUPC group. As a Ph.D. student, observing the collaboration among hundreds of members worldwide and the successful execution of the STAR experiment programs was truly motivating. My heartfelt gratitude goes to the RHIC operations group for their invaluable contributions to the research conducted at the STAR experiment. I am also thankful to Ki Mi from CCNU for discussions on important topics on various occasions.

My participation in the ALICE-STAR-India Collaboration and interactions with eminent members Prof. Bedanga Mohanty and Prof. Zubayer Ahammed have been very inspiring. I am also thankful to the ALICE-STAR-India working committee for giving me the opportunity to present my work in the Collaboration meetings, where I discussed my work with various members of the group including Dr. Md Nasim, Dr. Ankhi Roy, Dr. Chitrasen Jena, Dr. Partha Pritam Bhaduri, Dr. Nihar Sahoo, and Dr. Lokesh Kumar. I would also like to extend my gratitude to Dukhishyam Mallick, Ashwini Kumar, Prabhupada Dixit, Ishu Aggarwal, Arushi Dhamija, Prinyanshi Sinha, Rishab Sharma, and Sharang Sharma, whom I had the pleasure of meeting during collaboration meetings and various conferences.

Thanks to my labmates - Puja Kumari, Subhasmita Kar, Ajay Kumar, and Shivani Rani for meaningful discussions and for creating a supportive working environment in the lab. My batchmates Rohit Kumar, Subhodeep Dutta, Dixit M, Puja Kumari, Itishree Pradhan, Jyotirekha Mallick, Mohak Shukla, and Dr. Nishant Kumar have also provided a cordial environment when I needed it most.

Special thanks to my juniors, Arpita Mondal and Subhadeep Sarkar. Our discussions on various topics were not only encouraging but also deeply valued.

A special mention goes to my elder sister, Yasmeen Aslam, who has been a pillar of strength and a constant source of encouragement throughout my life, always just a phone call away to listen to my problems despite her busy schedule. Her presence has been the foundation of emotional support, and I am heartily grateful for it. I also extend my deepest gratitude to all my family members, including my father, Mohd. Aslam, my mother Afroz Jahan, my brother Rameez Aslam, and my sister Kausar Aslam, whose relentless support has been crucial during my PhD journey.

Finally, I acknowledge the financial support provided by MHRD and IIT Patna through the fellowship that supported my research. My gratitude also goes out to all those not mentioned by name but who have contributed to the successful completion of my thesis.

Place: Indian Institute of Technology Patna Sameer Aslam
Date: July 19, 2024

Contents

Certificate of Approval iii

Declaration v

Certificate vii

Acknowledgment ix

List of Tables xiii

List of Figures xv

Abstract xxiii

1 Introduction 1

1.1 The Standard Model of elementary particles . . . 2

1.2 Quantum Chromodynamics . . . 2

1.2.1 QCD phase diagram . . . 4

1.3 Heavy-ion collisions . . . 5

1.3.1 Strangeness production in heavy-ion collision . . . 7

1.4 The Beam Energy Scan (BES) Program . . . 8

1.5 Experimental Observables . . . 11

1.5.1 Strangeness enhancement . . . 11

1.5.2 Jet quenching . . . 12

1.5.3 Anisotropic flow . . . 14

1.5.3.1 Directed flow . . . 15

1.5.3.2 Elliptic flow . . . 15

1.5.4 Quarkonia suppression . . . 17

1.5.5 Global Spin Polarization of hyperons . . . 19

1.6 Thesis outline . . . 20

2 Experimental setup 23

2.1 Relativistic Heavy Ion Collider (RHIC) . . . 23

2.2 The Solenoidal Tracker At RHIC (STAR) . . . 25

2.2.1 The Time Projection Chamber . . . 27

2.2.1.1 Upgrade in iTPC . . . 30

3 Experimental analysis details and techniques 33

3.1 Dataset and Event Selection . . . 33

3.2 Strange hadrons reconstruction . . . 35
3.2.1 Strange V0 reconstruction using Helix Method . . . 36
3.2.1.1 Acceptance . . . 39
3.2.1.2 Signal extraction . . . 41
3.2.2 Strange V0 reconstruction using KFParticle Method . . . 43
3.2.2.1 Uncorrected p_T spectra . . . 43
3.2.3 Multi-strange hyperons reconstruction . . . 45
3.2.3.1 Acceptance . . . 49
3.2.3.2 Signal extraction . . . 51
3.2.3.3 Uncorrected p_T spectra . . . 52

3.3 Efficiency correction . . . 52

3.4 Estimation of Systematic Uncertainties . . . 57

3.5 Feed-down correction for Λ . . . 60

3.6 Corrected p_T spectra . . . 62

4 Results and discussions 69

4.1 Rapidity spectra . . . 69

4.2 Particle yield . . . 71

4.3 Nuclear Modification Factor (R_{cp}) . . . 73

4.4 Baryon-to-meson ratio . . . 75

5 Conclusion and outlook 81

Proceedings, conferences, and workshops 85

A Appendix 87

A.1 Acceptance × Reconstruction Efficiency . . . 87

Bibliography 91

List of Tables

3.1 Strange V0 particles and their weak decay channels [95]. 37
3.2 Topological cuts used for the reconstruction of V0 particles (K^0_s, Λ, $\overline{\Lambda}$). $\vec{p}_{V0}$ and $\vec{r}_{V0}$ represent the momentum and the position vector of the V0 particles respectively and $\vec{r}_{PV}$ denote the primary vertex position vector. 39
3.3 Selection criteria used for the reconstruction of $\Lambda(\overline{\Lambda})$ in Au+Au collisions at $\sqrt{s_{NN}} = 19.6$ GeV in the KFParticle package. 44
3.4 Weak decay channel of $\Xi^-(\overline{\Xi}^+)$ and $\Omega^-(\overline{\Omega}^+)$ [95]. 45
3.5 Topological selection criteria are applied for the reconstruction of $\Xi^-(\overline{\Xi}^+)$ and $\Omega^-(\overline{\Omega}^+)$. In this context, $\vec{r}_{Xi}$, $\vec{r}_{\Lambda}$, and $\vec{r}_{PV}$ refer to the decay vertex position vectors of $\Xi^-(\overline{\Xi}^+)$, $\Omega^-(\overline{\Omega}^+)$, and Λ, as well as the primary vertex position vector, respectively. The momentum vectors of $\Xi^-(\overline{\Xi}^+)$, $\Omega^-(\overline{\Omega}^+)$, and Λ are represented by $\vec{p}_{Xi}$ and $\vec{p}_{\Lambda}$, respectively 50
3.6 Default cuts and their variations for K^0_s and Λ ($\overline{\Lambda}$). 61
3.7 Default cuts and their variations for Ξ^- ($\overline{\Xi}^+$) and Ω^- ($\overline{\Omega}^+$). 61

This page is intentionally left blank

List of Figures

1.1 Unified strong coupling constant covering perturbative and non-perturbative QCD regimes. Non-perturbative processes have been absorbed into the definition of α_{g1} which obeys the limit, $lim_{Q\to 0}\alpha_{g1}(\mathrm{Q}) = \pi$. Figure is taken from [9]. 4

1.2 Schematic QCD phase diagram illustrating the experimental and theoretical exploration of the QCD matter. Figure is taken from [10]. . . 5

1.3 The figure provides a schematic representation of the space-time evolution in a heavy-ion collision. Figure is taken from [15]. 6

1.4 The relative yield ratios of K, ϕ, $\bar{\Lambda}$, and $\bar{\Xi} + \Xi$, normalized to $\langle N_{part}\rangle$, compared to the yields in inelastic p+p collisions are presented as functions of $\langle N_{part}\rangle$ at $\sqrt{s_{NN}} = 62.4$ and 200 GeV for Cu+Cu and Au+Au collisions. This figure is sourced from [43]. 12

1.5 R_{AA} of inclusive charge hadron relative to NN reference spectrum in different collision centralities in Au+Au collisions at $\sqrt{s_{NN}} = 130$ GeV. Figure is taken from [47]. 13

1.6 Schematic diagram illustrating the conversion of initial spatial anisotropy in the early stage of the collision to final state momentum anisotropy in the produced particles. Figure is taken from [53]. 15

1.7 Directed flow of charged hadrons as a function of rapidity is shown. The lower figure provides a more detailed view of the mid-pseudorapidity region from the upper figure. The figure is taken from [55]. 16

1.8 The elliptic flow (v_2) of identified hadrons, plotted against transverse momentum (p_T) in minimum bias Au+Au collisions at $\sqrt{s_{NN}} = 200$ GeV, is depicted. Solid and dotted lines in the figure represent model predictions for this system and energy level. The figure is taken from [65]. 17

1.9 v_2/n as a function of p_t/n, where n is the number of constituent quarks measured by the STAR experiment for various hadrons. Figure is taken from [65]. 18

1.10 R_{AA} of J/ψ as a function of $\langle\ N_{part}\ \rangle$ at midrapidity in Pb-Pb collisions at $\sqrt{s_{NN}} = 2.76$ TeV compared with PHENIX result at $\sqrt{s_{NN}} = 200$ GeV. Figure is taken from [75]. 19

2.1 An overhead view of the RHIC complex highlighting the positions of the STAR and sPHENIX detectors at Brookhaven National Laboratory. The figure is taken from [85]. 24

2.2 A schematic illustration of the STAR detector. This image is taken from [89]. . . . 26
2.3 A schematic figure of the STAR TPC showing the IFC, OFC, CM and 12 sectors on both sides of the TPC. Figure is taken from [92]. . . . 27
2.4 The layout of the STAR TPC anode sector showing the inner and the outer section. The outer section has more number of pads than the inner section. Figure is taken from [92]. . . . 28
2.5 Ionization energy loss of charged particles plotted as a function of rigidity (charge times momentum) within the TPC during Au+Au collisions at $\sqrt{s_{NN}}$ = 19.6 GeV. . . . 30

3.1 Fig. (a) on the left illustrates the V_z distribution for Au+Au collisions at $\sqrt{s_{NN}}$ = 19.6 GeV, while Fig. (b) on the right depicts the V_r distribution in the same collision settings. . . . 34
3.2 Fig. (a), displayed on the left, presents the correlation between the number of tracks matched with the TOF and those registered by the TPC. Events falling below the red line are categorized as pile-up and are excluded from the analysis. Fig. (b) on the right demonstrates the reference multiplicity distribution as measured by the TPC. Here, the blue line represents data before the exclusion of pile-up events, while the red line indicates the data after these events have been removed. . 35
3.3 The topology of strange V0 decay is described, where P_+ denotes positively charged particles and P_- denotes negatively charged particles. Figure is taken from [96]. . . . 38
3.4 Invariant mass distribution for K^0_s with p_T>0 in the 0-5% centrality range at mid-rapidity (|y|<0.5) during Au+Au collisions at $\sqrt{s_{NN}}$ = 19.6 GeV. The combinatorial background has been estimated using the rotational method. . . . 40
3.5 Invariant mass distributions for Λ and $\overline{\Lambda}$ at p_T>0.2 GeV/c within the 20-30% centrality and at mid-rapidity (|y|<0.5) in Au+Au collisions at $\sqrt{s_{NN}}$ = 19.6 GeV. The estimation of the combinatorial background was performed using the rotational method. . . . 40
3.6 The phase space distribution of K^0_s, Λ and $\overline{\Lambda}$ in Au+Au collisions at $\sqrt{s_{NN}}$ = 19.6 GeV. . . . 41
3.7 K^0_s, Λ and $\overline{\Lambda}$ invariant mass distributions in Au+Au collisions at $\sqrt{s_{NN}}$ = 19.6 GeV. The dashed lines represent the function fit results. The horizontal dashed lines are the fitted background contributions. The grey area shows the corresponding rotational background. . . . 42
3.8 The invariant mass distribution of K^0_s within the transverse momentum bins of [4.4, 5.0] GeV/c for 20-30% centrality at mid-rapidity (|y|<0.5) in Au+Au collisions at $\sqrt{s_{NN}}$ = 19.6 GeV. . . . 43
3.9 The invariant mass distribution of Λ and $\overline{\Lambda}$ at mid-rapidity (|y|<0.5) obtained using KFParticle Package in Au+Au collision at $\sqrt{s_{NN}}$ = 19.6 GeV. . . . 44

3.10 Comparison of uncorrected p_T spectra of Λ and ($\bar{\Lambda}$) for different centrality range at mid-rapidity (|y|<0.5) for Au+Au collisions at $\sqrt{s_{NN}}$ = 19.6 GeV from KFParticle and Helix method. 45
3.11 The uncorrected transverse momentum spectra of K^0_s under the rapidity range [-1.5, -0.75] and [0.75, 1.5] in different collision centralities in Au+Au collisions at $\sqrt{s_{NN}}$ = 19.6 GeV. 46
3.12 The uncorrected transverse momentum spectra of K^0_s under the rapidity range [-0.75, 0.75] in different collision centralities in Au+Au collisions at $\sqrt{s_{NN}}$ = 19.6 GeV. 46
3.13 The uncorrected transverse momentum spectra of Λ under the rapidity range [-1,1] in different collision centralities in Au+Au collisions at $\sqrt{s_{NN}}$ = 19.6 GeV. 47
3.14 The uncorrected transverse momentum spectra of $\overline{\Lambda}$ under the rapidity range [-1,1] in different collision centralities in Au+Au collisions at $\sqrt{s_{NN}}$ = 19.6 GeV. 47
3.15 The Ξ^- decay topology with all the cuts shown in the plot. The decay topology of Ω^- is similar to Ξ^- where the bachelor particle is kaon. Figure is taken from [96]. 48
3.16 Invariant mass distributions for Ξ^- and $\overline{\Xi}^+$ at $p_T > 0.4$ GeV/c within the 10-20% centrality at mid-rapidity ($|y| < 0.5$) in Au+Au collisions at $\sqrt{s_{NN}}$ = 19.6 GeV. The estimation of the combinatorial background was performed using the rotational method. 50
3.17 Invariant mass distributions for Ω^- and $\overline{\Omega}^+$ at $p_T > 0.7$ GeV/c within the 20-30% centrality at mid-rapidity ($|y| < 0.5$) in Au+Au collisions at $\sqrt{s_{NN}}$ = 19.6 GeV. The estimation of the combinatorial background was performed using the rotational method. 51
3.18 The phase space distribution of multi-strange hyperons $\Xi^-(\overline{\Xi}^+)$, $\Omega^-(\overline{\Omega}^+)$ in Au+Au collisions at $\sqrt{s_{NN}}$ = 19.6 GeV. 52
3.19 Ξ^-, $\overline{\Xi}^+$, Ω^-, and $\overline{\Omega}^+$ invariant mass distributions in Au+Au collisions at $\sqrt{s_{NN}}$ = 19.6 GeV. The dashed lines represent the function fit results (double Gaussian plus polynomial). The horizontal dashed lines are the fitted background contributions. The grey area shows the corresponding rotational background. 53
3.20 The invariant mass distribution of $\overline{\Xi}^+$ and Ω^- within the transverse momentum bins of [4.1, 4.9] GeV/c for 0-5% centrality and [3.8, 4.6] GeV/c for 0-10% centrality, respectively, at mid-rapidity (|y|<0.5) in Au+Au collisions at $\sqrt{s_{NN}}$ = 19.6 GeV. 54
3.21 The uncorrected transverse momentum spectra of Ξ^- under the rapidity range [-1,1] in different collision centralities in Au+Au collisions at $\sqrt{s_{NN}}$ = 19.6 GeV. 54
3.22 The uncorrected transverse momentum spectra of $\overline{\Xi}^+$ under the rapidity range [-1,1] in different collision centralities in Au+Au collisions at $\sqrt{s_{NN}}$ = 19.6 GeV. 55

3.23 The uncorrected transverse momentum spectra of Ω^- under the rapidity range [-0.9,0.9] in different collision centralities in Au+Au collisions at $\sqrt{s_{NN}}$ = 19.6 GeV. 55

3.24 The uncorrected transverse momentum spectra of $\overline{\Omega}^+$ under the rapidity range [-0.9,0.9] in different collision centralities in Au+Au collisions at $\sqrt{s_{NN}}$ = 19.6 GeV. 56

3.25 The acceptance × reconstruction efficiencies of K^0_s, Λ, Ξ^-, Ω^- at mid-rapidity (|y|<0.5) in 0-5% central Au+Au collisions at $\sqrt{s_{NN}}$ = 19.6 GeV. The open circles in each panel represent the acceptance × reconstruction efficiencies of particles from BES-II analysis, and the solid red circles represent the acceptance × reconstruction efficiencies of particles from BES-I analysis [37]. The lower panels of each plot provide a comparison between these two datasets. The selection cuts in BES-I and BES-II are the same. 57

3.26 The acceptance × reconstruction efficiency of K^0_s in Au+Au collisions at $\sqrt{s_{NN}}$ = 19.6 GeV in rapidity range [-1.5,-0.75] and [0.75,1.5]. . . . 58

3.27 The acceptance × reconstruction efficiency of K^0_s in Au+Au collisions at $\sqrt{s_{NN}}$ = 19.6 GeV in rapidity range [-0.75,0.75]. 58

3.28 The figures show the percentage of the systematic errors plotted against the default statistical error for different systematic sources for K^0_s in the rapidity range [1.0, 1.25] in Au+Au collisions at $\sqrt{s_{NN}}$ = 19.6 GeV. 60

3.29 Fig. (a) shows the feed-down fraction for Λ. The plot shows the corrections applied due to the contributions from both Ξ^- and Ξ^0 particles. Fig. (b) shows feed-down fractions for $\overline{\Lambda}$. The plot shows the corrections applied due to the contributions from both $\overline{\Xi}^+$, $\overline{\Xi}^0$ particles. Fig. (c) shows feed-down fractions for $\overline{\Lambda}$. The plot shows the corrections applied due to the contributions from both $\overline{\Omega}^+$. 62

3.30 The corrected transverse momentum spectra of K^0_s at mid-rapidity (|y|<0.5) in Au+Au collisions at $\sqrt{s_{NN}}$ = 19.6 GeV. The open circles represent K^0_s corrected transverse momentum spectra from BES-II analysis, and the solid circles represent the corrected transverse momentum spectra from BES-I analysis. The lower panel provides a comparison between these two datasets. 63

3.31 The corrected transverse momentum spectra of Λ and $\overline{\Lambda}$ at mid-rapidity (|y|<0.5) in Au+Au collisions at $\sqrt{s_{NN}}$ = 19.6 GeV. The open circles in both the panels represent Λ and $\overline{\Lambda}$ corrected transverse momentum spectra from BES-II analysis, and the solid circles represent the corrected transverse momentum spectra from BES-I analysis. The lower panels provide a comparison between these two datasets. The square boxes in case of $\overline{\Lambda}$ show systematic errors. 64

3.32 The corrected transverse momentum spectra of Ξ^- and $\overline{\Xi}^+$ at mid-rapidity (|y|<0.5) in Au+Au collisions at $\sqrt{s_{NN}}$ = 19.6 GeV. The open circles in both the panels represent Ξ^- and $\overline{\Xi}^+$ corrected transverse momentum spectra from BES-II analysis and the solid circles represent the corrected transverse momentum spectra from BES-I analysis. The lower panels provide a comparison between these two datasets. . . . 64

3.33 The corrected transverse momentum spectra of K^0_s in rapidity range [-1.5,-0.75] and [0.75,1.5] in Au+Au collisions at $\sqrt{s_{NN}}$ = 19.6 GeV. The vertical bars represent the statistical error, and the vertical bands represent the systematic errors. . . . 65

3.34 The corrected transverse momentum spectra of K^0_s in rapidity range [-0.75,0.75] in Au+Au collisions at $\sqrt{s_{NN}}$ = 19.6 GeV. The vertical bars represent the statistical error, and the vertical bands represent the systematic errors. . . . 65

3.35 The corrected transverse momentum spectra of Λ in rapidity range [-1,1] in Au+Au collisions at $\sqrt{s_{NN}}$ = 19.6 GeV. The vertical bars represent the statistical error, and the vertical bands represent the systematic errors. . . . 66

3.36 The corrected transverse momentum spectra of $\overline{\Lambda}$ in rapidity range [-1,1] in Au+Au collisions at $\sqrt{s_{NN}}$ = 19.6 GeV. The vertical bars represent the statistical error, and the vertical bands represent the systematic errors. . . . 66

3.37 The corrected transverse momentum spectra of Ξ^- in rapidity range [-1,1] in Au+Au collisions at $\sqrt{s_{NN}}$ = 19.6 GeV. The vertical bars represent the statistical error, and the vertical bands represent the systematic errors. . . . 67

3.38 The corrected transverse momentum spectra of $\overline{\Xi}^+$ in rapidity range [-1,1] in Au+Au collisions at $\sqrt{s_{NN}}$ = 19.6 GeV. The vertical bars represent the statistical error, and the vertical bands represent the systematic errors. . . . 67

3.39 The corrected transverse momentum spectra of Ω^- in rapidity range [-0.9,0.9] in Au+Au collisions at $\sqrt{s_{NN}}$ = 19.6 GeV. The vertical bars represent the statistical error, and the vertical bands represent the systematic errors. . . . 68

3.40 The corrected transverse momentum spectra of $\overline{\Omega}^+$ in rapidity range [-0.9,0.9] in Au+Au collisions at $\sqrt{s_{NN}}$ = 19.6 GeV. The vertical bars represent the statistical error, and the vertical bands represent the systematic errors. . . . 68

4.1 Rapidity spectra of K^0_s, Λ, $\overline{\Lambda}$, Ξ^-, $\overline{\Xi}^+$, Ω^-, and $\overline{\Omega}^+$ for different centrality ranges in Au+Au collisions at $\sqrt{s_{NN}}$ = 19.6 GeV. Vertical bands indicate systematic errors. . . . 71

4.2 Particle yields denoted as $dN/dy/(\langle N_{\rm part}\rangle/2)$ as a function of the average number of participating nucleon pairs $\langle N_{\rm part}\rangle$ for K^0_s, Λ, Ξ^-, and Ω^- in Au+Au collisions at $\sqrt{s_{NN}}$ = 19.6 GeV. The left panels in the above figure represent $dN/dy/(\langle N_{\rm part}\rangle/2)$ in the negative rapidity region [-1.5,0] for K^0_s, [-1.0,0] for Λ, Ξ^-, and [-0.9,0] for Ω^-. The right panels represent $dN/dy/(\langle N_{\rm part}\rangle/2)$ in the positive rapidity region [0,1.5] for K^0_s, [0,1.0] for Λ, Ξ^-, and [0,0.9] for Ω^-. Systematic uncertainties are indicated by vertical bands. 72
4.3 Particle yields denoted as $dN/dy/(\langle N_{\rm part}\rangle/2)$ as a function of the average number of participating nucleon pairs $\langle N_{\rm part}\rangle$ for $\overline{\Lambda}$, $\overline{\Xi}^+$, $\overline{\Omega}^+$ in Au+Au collisions at $\sqrt{s_{NN}}$ = 19.6 GeV. The left panels in the above figure represent $dN/dy/(\langle N_{\rm part}\rangle/2)$ in the negative rapidity region [-1.0,0] for $\overline{\Lambda}$, $\overline{\Xi}^+$, and [-0.9,0] for $\overline{\Omega}^+$. The right panels represent $dN/dy/(\langle N_{\rm part}\rangle/2)$ in the positive rapidity region [0,1.0] for $\overline{\Lambda}$, $\overline{\Xi}^+$, and [0,0.9] for $\overline{\Omega}^+$. Systematic uncertainties are indicated by vertical bands. 73
4.4 The R_{cp} values for K^0_s, Λ+$\overline{\Lambda}$, Ξ^-+$\overline{\Xi}^+$, and Ω^-+$\overline{\Omega}^+$ at mid-rapidity (|y|<0.5) and higher rapidity (0.5<|y|<1.0) in Au+Au collisions at $\sqrt{s_{NN}}$ = 19.6 GeV. 74
4.5 Fig. (a), Fig. (b), and Fig. (c) show the R_{cp} values for π^+, π^-, K^+, K^-, p, and $\overline{p}$ taken from [103]. Fig. (d), Fig. (e), Fig. (f) show the R_{cp} of Λ, $\overline{\Lambda}$, Ξ^-, $\overline{\Xi}^+$, Ω^-, $\overline{\Omega}^+$ in Au+Au collisions at $\sqrt{s_{NN}}$ = 19.6 GeV. The bottom panel shows ratio of antiparticle to particle. 75
4.6 The R_{cp} of Λ, $\overline{\Lambda}$ at different collision energies from $\sqrt{s_{NN}}$ = 200 GeV, 39 GeV, 27 GeV, and 19.6 GeV. The lower panel compares the ratio of R_{cp} of Λ and $\overline{\Lambda}$. 76
4.7 The R_{cp} of Ξ^-, $\overline{\Xi}^+$ at different collision energies from $\sqrt{s_{NN}}$ = 2.76 TeV, 200 GeV, 39 GeV, 27 GeV, and 19.6 GeV. The lower panel compares the ratio of R_{cp} of Ξ^- and $\overline{\Xi}^+$. 77
4.8 Λ/K^0_s, Ξ^-/K^0_s, Ω^-/K^0_s ratios at mid-rapidity (|y|<0.5) and higher rapidity (0.5<|y|<1.0), as a function of p_T in Au+Au collisions at $\sqrt{s_{NN}}$ = 19.6 GeV. 78
4.9 $\overline{\Lambda}/K^0_s$, $\overline{\Xi}^+/K^0_s$, $\overline{\Omega}^+/K^0_s$ ratios at mid-rapidity (|y|<0.5) and higher rapidity (0.5<|y|<1.0), as a function of p_T in Au+Au collisions at $\sqrt{s_{NN}}$ = 19.6 GeV. 79

A.1 The acceptance × reconstruction efficiencies of Λ under the rapidity range [-1,1] in different collision centralities in Au+Au collisions at $\sqrt{s_{NN}}$ = 19.6 GeV. 87
A.2 The acceptance × reconstruction efficiencies of $\overline{\Lambda}$ under the rapidity range [-1,1] in different collision centralities in Au+Au collisions at $\sqrt{s_{NN}}$ = 19.6 GeV. 87
A.3 The acceptance × reconstruction efficiencies of Ξ^- under the rapidity range [-1.0,1.0] in different collision centralities in Au+Au collisions at $\sqrt{s_{NN}}$ = 19.6 GeV. 88

A.4 The acceptance × reconstruction efficiencies of $\overline{\Xi}^{+}$ under the rapidity range [-1.0,1.0] in different collision centralities in Au+Au collisions at $\sqrt{s_{NN}}$ = 19.6 GeV. 88
A.5 The acceptance × reconstruction efficiencies of Ω^{-} under the rapidity range [-0.9, 0.9] in different collision centralities in Au+Au collisions at $\sqrt{s_{NN}}$ = 19.6 GeV. 89
A.6 The acceptance × reconstruction efficiencies of $\overline{\Omega}^{+}$ under the rapidity range [-0.9, 0.9] in different collision centralities in Au+Au collisions at $\sqrt{s_{NN}}$ = 19.6 GeV. 89

This page is intentionally left blank

Abstract

The primary aim of high-energy heavy-ion collisions is to investigate the characteristics of quantum chromodynamics (QCD) matter under extreme conditions. This involves studying the behavior and interactions of partons (quarks and gluons) generated in these collisions. The Relativistic Heavy Ion Collider (RHIC) at Brookhaven National Laboratory (BNL) conducts heavy-ion collisions to explore a deconfined state of matter known as the Quark-Gluon Plasma (QGP). At such high temperatures and energy densities, quarks and gluons are freed from their confinement within hadrons and exist in a free state, yet they continue to interact strongly with one another.

Strange and multi-strange particles play a crucial role in these studies as their production rates and behavior provide sensitive probes of QCD matter. The presence of strange quarks, which are not typically found in ordinary nuclear matter, can offer insights into the conditions and dynamics within the QGP. The study of strange hadron production helps in understanding the mechanisms of particle interaction and the properties of the medium created in such collisions.

This thesis explores the production of strange and multi-strange particles (K^0_s, Λ, $\overline{\Lambda}$, Ξ^-, $\overline{\Xi}^+$, Ω^-, $\overline{\Omega}^+$) in Au+Au collisions at $\sqrt{s_{NN}}$ = 19.6 GeV, conducted as part of the Beam Energy Scan (BES) phase-II (BES-II) program. Utilizing the enhanced capabilities of the upgraded inner Time Projection Chamber (iTPC) in BES-II, we extended the analysis from mid-rapidity (|y|<0.5) in BES-I to a larger rapidity range (0.5<|y|<1.0), providing a more comprehensive investigation of strangeness production. Apart from this, we compared the spectra results from the previous BES-I analysis with that of the BES-II analysis in order to check the consistency between the two analyses.

The transverse momentum (p_T) spectra provide information about the integrated particle yields ($\frac{dN}{dy}$) of the particles. We studied the spectra of particles under different rapidity ranges, ranging from |y|<1.5 for K^0_s, |y|<1.0 for $\Lambda(\overline{\Lambda})$, $\Xi^-(\overline{\Xi}^+)$, and |y|<0.9 for $\Omega^-(\overline{\Omega}^+)$. The integrated yields ($\frac{dN}{dy}$) were utilized to study the rapidity spectra of the particles. We observed that the rapidity spectra of K^0_s, antibaryons like $\overline{\Lambda}$, and $\overline{\Xi}^+$ show Gaussian-like distributions, while the rapidity spectra of baryons like Λ and Ξ^- show wider distributions. This could be attributed to baryon-stopping mechanisms, where baryons are more likely to be stopped in the collision zone, leading to a flatter

rapidity distribution.

The nuclear modification factor (R_{cp}) of strange and multi-strange particles was studied at mid-rapidity (|y|<0.5) as well as at a larger rapidity range (0.5<|y|<1.0). The combined R_{cp} of particles and antiparticles shows minor rapidity dependence. Additionally, the R_{cp} of baryons (Λ, Ξ^-, Ω^-) and antibaryons ($\overline{\Lambda}$, $\overline{\Xi}^+$, $\overline{\Omega}^+$) were also studied separately at mid-rapidity (|y|<0.5). We observed that the R_{cp} of antibaryons is lower than that of baryons at low p_T, indicating the possible annihilation of antibaryons in a baryon-rich environment at $\sqrt{s_{NN}} = 19.6$ GeV.

The study also analyzed baryon-to-meson ratios (Λ/K^0_s, Ξ^-/K^0_s, Ω^-/K^0_s) and antibaryon-to-meson ratios ($\overline{\Lambda}/K^0_s$, $\overline{\Xi}^+/K^0_s$, $\overline{\Omega}^+/K^0_s$) at mid-rapidity (|y|<0.5) and larger rapidity range (0.5<|y|<1.0). An enhancement in the baryon-to-meson ratios and antibaryon-to-meson ratios was observed at intermediate p_T in most central collisions compared to peripheral collisions. This enhancement decreased progressively from Λ/K^0_s ($\overline{\Lambda}/K^0_s$) ratio to Ξ^-/K^0_s ($\overline{\Xi}^+/K^0_s$), and Ω^-/K^0_s ($\overline{\Omega}^+/K^0_s$). This trend suggests a hierarchy in baryon production relative to meson production, influenced by the varying masses and quark compositions of these particles. Further, a clear rapidity dependence was observed between mid-rapidity (|y|<0.5) and the larger rapidity range (0.5<|y|<1.0) in both baryon-to-meson ratios and antibaryon-to-meson ratios.

Chapter 1

Introduction

To explore the strongly interacting matter under extreme conditions in the laboratory set-up, heavy ions are collided at relativistic speed. The Bevalac at Lawrence Berkeley National Laboratory (LBNL) was one of the first facilities to perform heavy-ion collisions, operational in the late 1970s and early 1980s. Facilities including the Alternating Gradient Synchrotron (AGS) at Brookhaven National Laboratory, the Heavy Ion Synchrotron (SIS) at the Helmholtz Center for Heavy Ion Research, and the Super Proton Synchrotron (SPS) at the European Organization for Nuclear Research (CERN) achieved collision energies in the range of a few GeV per nucleon. These experiments were essential in studying nuclear matter at high densities and temperatures. Advanced Collider Facilities, such as the Relativistic Heavy Ion Collider (RHIC) at BNL and the Large Hadron Collider (LHC) at CERN, with enhanced technology and upgraded detectors, have significantly extended this energy range from a few GeV to hundreds of GeV. RHIC has effectively conducted collisions involving Cu+Cu, Zr+Zr, Ru+Ru, and Au+Au at $\sqrt{s_{NN}} = 200$ GeV, which stands as the highest energy per nucleon pair achieved in heavy-ion collisions at this facility. The LHC has successfully performed Pb+Pb collisions and Xe-Xe collisions at $\sqrt{s_{NN}} = 5.02$ TeV and $\sqrt{s_{NN}} = 5.44$ TeV respectively.

The most significant characteristic of relativistic heavy-ion collisions is the immense amount of energy deposited in a very small volume for a very short period of time. Within these nuclei, nucleons - composed of quarks and gluons - experience

extreme temperatures and densities during collisions. This leads to a deconfined state where quarks and gluons are no longer bound within hadrons but instead, interact freely in a strongly coupled plasma. This state is known as the Quark-Gluon Plasma (QGP) [1], a unique form of matter believed to have existed shortly after the Big Bang. The creation of QGP in collider experiments like RHIC helps study a state of matter that mimics early universe conditions, hence these experiments are often referred to as 'Mini Big Bangs'.

1.1 The Standard Model of elementary particles

The Standard Model of particle physics describes three of the fundamental forces: electromagnetic, weak, and strong interactions. It classifies all known elementary particles and explains their interactions through these three forces. It does not model gravity and makes no prediction regarding neutrino mass, baryon asymmetry, and dark matter or dark energy.

The foundational steps toward the Standard Model began in 1961 when Sheldon Glashow unified the electromagnetic and weak interactions [2]. The model was significantly advanced in 1967 by Steven Weinberg and Abdus Salam, who each independently incorporated the Higgs mechanism into Glashow's electroweak theory, giving the model its present structure [3][4]. This theory predicted the existence of the Higgs boson (H), a particle essential for imparting mass to various fermions and the massive gauge bosons through interactions with the space-time permeating Higgs field. The existence of this boson was confirmed by experiments conducted at the Large Hadron Collider in 2012 [5][6].

1.2 Quantum Chromodynamics

Quantum Chromodynamics (QCD) is the theory that describes the strong interaction in the Standard Model of elementary particles. It is a crucial part of the Standard Model of particle physics, addressing the color charges responsible for the behavior

of the strong force. In QCD, quarks interact with each other through the exchange of particles called gluons, which act as the carriers of the strong force.

The coupling constant (α_s) in QCD determines the strength of the interaction between quarks and gluons. Unlike the electromagnetic coupling constant, which is basically a fine-structure constant ($\alpha = 1/137$ for low energy), the QCD coupling constant is not a fixed quantity but varies with energy. This variation is a key feature in QCD and is described by the renormalization equation as -

$$\alpha_s(Q^2) \approx \frac{12\pi}{(11n_C - 2n_f)\ln\left(\frac{|Q^2|}{\Lambda^2}\right)} \tag{1.1}$$

where Q^2 denotes the momentum transfer squared, n_C indicates the total number of quark colors, n_f represents the total number of quark flavors, and Λ is the scaling parameter typically found in the range from 100 MeV to 500 MeV.

At very high energies (or equivalently, very short distances), the QCD coupling constant (α_s) becomes small. In this regime of QCD, quarks and gluons interact very weakly with each other. This property of QCD is called *asymptotic freedom* [7]. This was a groundbreaking discovery by David Gross, Frank Wilczek, and H. David Politzer in 1974, for which they were awarded the Nobel Prize in 2004. Asymptotic freedom explains why quarks behave almost as free particles in high-energy processes, such as those occurring in particle colliders like RHIC and LHC.

At low energies (or larger distances), the coupling constant (α_s) becomes large. In this regime of QCD, the interaction between quarks and gluons becomes so strong that they are permanently bound within hadronic states such as protons and neutrons. This property in QCD is called *confinement* [8]. The confinement explains why quarks and gluons are never observed individually but are always found within composite particles. In theoretical physics, the precise mechanism of confinement is one of the major unresolved problems, but lattice QCD calculations provide evidence of its validity. Figure 1.1 shows the coupling constant at different regimes in the QCD.

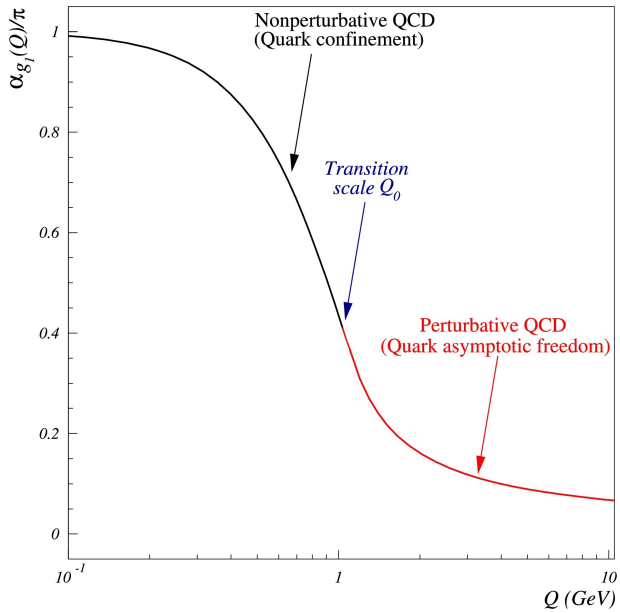

Figure 1.1: Unified strong coupling constant covering perturbative and non-perturbative QCD regimes. Non-perturbative processes have been absorbed into the definition of α_{g1} which obeys the limit, $lim_{Q\to 0}\alpha_{g1}(\mathrm{Q}) = \pi$. Figure is taken from [9].

1.2.1 QCD phase diagram

The QCD phase diagram represents different phases of strongly interacting matter as a function of temperature (T) and baryon chemical potential (μ_B). At low temperatures and low baryon chemical potential, matter mainly exists in the form of hadrons (protons, neutrons, and mesons). This phase is characterized by confinement, where quarks and gluons are tightly bound together in their hadronic states. In this regime, the value of the QCD coupling constant is large, and the interactions are described using non-perturbative QCD. At high temperatures and baryon chemical potentials, the value of the coupling constant becomes small. As a result, the interactions between quarks and gluons become weaker due to asymptotic freedom, leading to a phase transition. At these extreme conditions, the interactions are described using perturbative QCD. Figure 1.2 presents the phase diagram of strongly interacting matter within the framework of QCD.

The transition from the hadronic state to QGP is a smooth crossover at high temperatures and nearly zero μ_B values, as achieved at the LHC, where energies reach

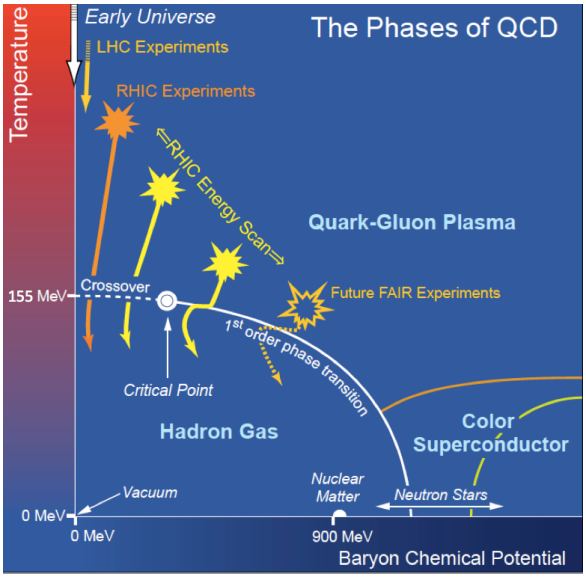

Figure 1.2: Schematic QCD phase diagram illustrating the experimental and theoretical exploration of the QCD matter. Figure is taken from [10].

several TeV, and at the top energy of RHIC, $\sqrt{s_{NN}} = 200$ GeV. In this region of the QCD phase diagram, matter and antimatter are produced in nearly equal amounts, supporting the smooth crossover transition from hadronic matter to QGP. However, at higher finite values of μ_B, Lattice QCD predicts a first-order phase transition. This transition is suggested to end at a critical point [11][12][13], beyond which it becomes a smooth crossover.

Experimentally, it is possible to transition from the hadronic phase to QGP by colliding heavy ions at relativistic speeds. RHIC is ideally suited for this purpose, as it can vary the collision energies of the heavy ions to systematically probe different regions of the QCD phase diagram. For this purpose, RHIC launched the Beam Energy Scan (BES) program, which aims to scan the QCD phase diagram at various regions, focusing particularly on higher baryon chemical potential regions where theoretical models face significant challenges.

1.3 Heavy-ion collisions

Figure 1.3 shows the space-time evolution of the system under two different scenarios. First, if the energy of the colliding nuclei is not high enough to create a QGP medium,

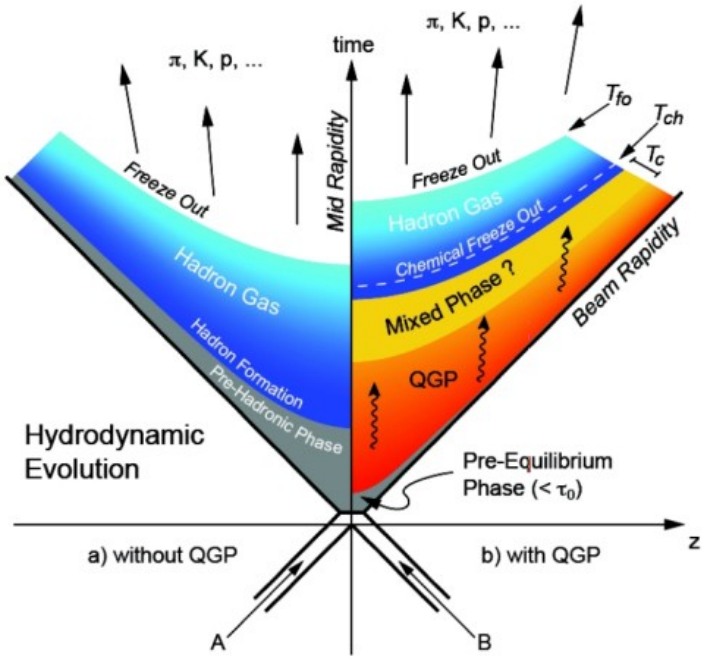

Figure 1.3: The figure provides a schematic representation of the space-time evolution in a heavy-ion collision. Figure is taken from [15].

the system consists of the gas of hadrons, as shown on the left-hand side of the figure. On the other hand, if the energy of the colliding nuclei is high enough, a QGP medium is created, as shown on the right-hand side of the figure [14]. The QGP medium rapidly expands and cools down, and a mixed phase containing the QGP and the hadron gas occurs. As the system further expands and cools down, the mixed phase ends up with only the hadron gas. During this time, the particles continue inelastic interaction with decay and formation of new particles. After a certain temperature, the inelastic interaction ceases, and the abundance and species of the particles are fixed. This stage is known as chemical freeze-out. However, the particles share momentum with each other. With further expansion, the medium becomes so dilute that even the elastic collisions cease, and the momentum of the particles gets fixed. This stage is called the kinetic freeze-out. After this stage, the particle flows towards the detector.

To understand the dynamic of the collisions, first thing one needs to find out is whether all the nucleons of the heavy-ion or only few of the nucleons participated in

the interactions. This is done by defining a observable centrality of a collision. It represents the impact parameter (b), a perpendicular distance between the centers of the colliding nuclei. A collision is a central when the impact parameter is close to zero. On the other hand, collisions with a larger impact parameter are termed peripheral, involving only portions of the nuclei in the interaction. The section of the colliding nuclei that does not participate in the collisions is called the spectator. However, in experiments the impact parameter is difficult to determine, so the centrality of the colliding nuclei is determined using the reference multiplicities which are the number of charged particles produced in the collisions.

1.3.1 Strangeness production in heavy-ion collision

Particles containing strange quarks are known as strange particles, such as the K_s^0 meson and Ξ baryon. These particles may contain one or more strange quarks; for instance, the Λ baryon (uds) has a net strangeness of 1 due to its single strange quark, while the Ω^- baryon (sss) contains three strange quarks, each contributing to a total strangeness of -3. Initially, the colliding nuclei are comprised of nucleons (protons and neutrons), which consist of up and down quarks, with no net strangeness present. Upon collision, the energy released is sufficient to produce strange quarks, which are significantly lighter than heavier quarks, such as the top and bottom. While top quarks decay almost instantaneously and do not form hadrons, strange quarks can be produced in abundance and are observed in hadronic form. These strange quarks can form in the medium through processes such as gluon-gluon fusion and quark-antiquark pair production [16]. As the quark-gluon plasma created in the collision cools and expands, these strange quarks hadronize by combining with each other or with up and down quarks, resulting in the formation of various strange mesons and baryons.

For example, a strange quark produced in the medium through gluon fusion or quark anti-quark annihilation can combine with an up quark (u) and a down quark (d) to form a Λ baryon (Λ) while a strange quark (s) can pair up with another strange

quark (s) and a down quark (d) to form negatively charge Ξ^-, as follows -

$$g + g \longrightarrow s + \bar{s} \text{ (gluon fusion)}$$

$$q + \bar{q} \longrightarrow s + \bar{s} \text{ (quark anti-quark annihilation)}$$

$$s + u + d \longrightarrow \Lambda \quad \text{(hadronization)}$$

$$s + s + d \longrightarrow \Xi^- \text{ (hadronization)}$$

The production of these particles in heavy-ion collisions reflects that the strangeness is created during the collisions or during the evolution of the fireball, which was absent before the collisions. Production of these strange particles serve as an essential probe in studying the medium created in heavy-ion collisions, offering insights into the early-stage conditions and medium density.

At low collision energies, such as those explored by the BES program at RHIC, hadronic interactions dominate over partonic interactions. In this scenario, there may be an interplay between partonic and hadronic interactions, or the medium produced in the collisions may be entirely hadronic. In such hadronic interactions, quark-antiquark annihilation processes are more significant compared to gluon fusion, and $s\bar{s}$ pairs can be formed through quark-antiquark annihilation, leading to the production of strange and multi-strange particles.

1.4 The Beam Energy Scan (BES) Program

The first decade of RHIC, since its operation in 2000, was dedicated to creating and studying the QGP at different collision energies, including its top energy at $\sqrt{s_{NN}}$ = 200 GeV. During this decade, RHIC made significant achievements that advanced our understanding of QGP and its properties [17].

The enhanced production of strange hadrons, such as kaons and hyperons, was observed in heavy-ion collisions, supporting the QGP formation hypothesis [18]. The suppression of high transverse momentum (p_T) hadrons in heavy-ion collisions was

observed, providing evidence for the parton energy loss effects in the dense QGP medium, commonly referred to as jet quenching [19][20][21][22]. The elliptic flow (v_2) studies provided evidence that the QGP behaves like a perfect fluid with extremely low viscosity [17][23]. Furthermore, the elliptic flow (v_2) studies demonstrated strong azimuthal anisotropy, indicating significant collective behavior and early thermalization of the produced medium [24][25][26]. Measurements of higher harmonics of azimuthal anisotropy contributed to a deeper understanding of the initial geometry and fluctuations in collision dynamics [27]. Measurements of direct photons provided information on the initial temperature and thermal properties of the QGP [28]. Many significant contributions focused on QGP formation and its properties were made in the first decade of RHIC operation.

In the second decade, RHIC launched the Beam Energy Scan (BES) program [29] to explore various regions of the QCD phase diagram, with a focus on the higher baryon chemical potential region, which was accessed by lowering the center of mass energy from $\sqrt{s_{NN}}$ = 200 GeV to 7.7 GeV in the collider mode. Measurements from BES phase-I (BES-I) indicate changes in medium properties at lower collision energies, but their precision is insufficient to draw definitive conclusions. Many observables in BES-I, such as critical points, first-order phase transitions, and the onset of deconfinement, were affected by factors that influenced the precision of the results. These factors include statistical precision, detector capabilities, the limited energy range, and beam quality and luminosity [30].

During BES-I, STAR measured the moments of the net-proton and net-charge multiplicities for different collision energies. The higher-order moments and their cumulant ratios, such as Sσ and $\kappa\sigma^2$, were examined for non-monotonic behavior. The STAR data showed that there were deviations from Poisson expectations, and the cumulant ratio exhibited non-monotonic behavior. However, the statistical significance of these deviations was not strong enough to make definitive conclusions about the critical point. The monotonic trends were suggestive but required higher statistics and reduced systematic uncertainties for confirmation [31][32][33].

STAR measured the directed flow (v_1) of identified hadrons such as protons, antiprotons, and pions [34]. The non-monotonic behavior in the slope of directed flow dv_1/dy for protons as a function of collision energy suggests the presence of a first-order phase transition. The slope of the directed flow (dv_1/dy) of protons is sensitive to the early stage dynamics of heavy-ion collisions and can provide insights into the equation of state of QGP. However, BES-I statistics need to be more comprehensive in order to map out the apparent strong centrality dependence of the phenomenon. The elliptic flow, represented by the parameter v_2, is the second harmonic component of the Fourier expansion of the azimuthal particle distribution with respect to the event plane [35]. The measurement of elliptic flow (ν_2) for various identified particles (e.g., pions, kaons, protons) across a range of beam energies $\sqrt{s_{NN}}$ = 7.7 - 62.4 GeV were observed to decrease with decreasing collision energy. This trend indicates that the degree of anisotropic flow is reduced at lower energies, which can be attributed to a change in the medium properties from a partonic phase to a hadronic phase [36].

STAR also measured the nuclear modification factor (R_{cp}) for inclusive charged hadrons, as well as for strange and multi-strange hadrons, across various collision energies ($\sqrt{s_{NN}}$ = 7.7 to 62.4 GeV) during BES-I [37][38]. The measurements indicated a reduction in partonic energy loss with decreasing collision energy. However, the limited p_T reach restricted the study of the interplay between the hard scatterings, which dominate at high p_T, and the effects of soft physics, which are more prominent at low p_T.

Since 2018, STAR has implemented the BES-II program, collecting comprehensive Au+Au collision data at multiple energies below $\sqrt{s_{NN}}$ = 27 GeV [39]. The BES-II aimed to further explore the QCD phase diagram of nuclear matter with higher statistics, improved detector capabilities, especially the inner section of the TPC (iTPC) [40], and a wider range of collision energies, including the fixed target energies to expand its reach towards the higher baryon chemical potential region in the QCD phase diagram [41]. The upgrade in iTPC in BES phase-II presents the opportunity to study new physics at STAR regarding the rapidity dependence of different observables.

1.5 Experimental Observables

In relativistic heavy-ion collisions at facilities such as RHIC and LHC, the quark-gluon plasma (QGP) undergoes a complex evolution process before hadronizing into particles that are detected by the detectors. The final state particles emerging from this evolution provide critical information about the dynamics and properties of the medium. These particles can be produced during the initial hard scatterings, from the thermalized QGP, and during the hadronization process. They help study various observables such as strangeness enhancement, jet quenching, and flow patterns. Each observable carries unique information about the medium, from its initial formation and thermal properties to the interactions and energy loss mechanisms of high-energy partons traversing the medium.

In the subsequent sections, we will discuss various signals of QGP formation along with the defining features of the medium.

1.5.1 Strangeness enhancement

Strangeness enhancement refers to the increased production of strange quarks and strange hadrons in heavy-ion collisions compared to proton-proton (p+p) collisions. In high-energy nuclear collisions, a dense partonic medium, known as the QGP, can be formed. This medium facilitates the production of strange quarks due to the high energy densities through processes such as gluon fusion ($gg \longrightarrow s\bar{s}$) and quark annihilation ($q\bar{q} \longrightarrow s\bar{s}$). Thus, strangeness enhancement serves as an important probe for studying the properties of the medium produced in heavy-ion collisions [16]. Figure 1.4 shows the yield of K, ϕ, $\bar{\Lambda}$, and $\bar{\Xi} + \Xi$ normalized by the average number of participating nucleons in Cu+Cu and Au+Au collisions at $\sqrt{s_{NN}} = 62.4$ and 200 GeV [42][43][44][45]. The enhancement of ϕ meson is observed to be higher at $\sqrt{s_{NN}} = 200$ GeV compared to 62.4 GeV in both Cu+Cu and Au+Au collisions. Also, the enhancement of ϕ mesons follows a different trend than those of strange baryons. These observations suggest that the increased presence of strange hadrons is related to the creation of a dense partonic medium during collisions at these energy

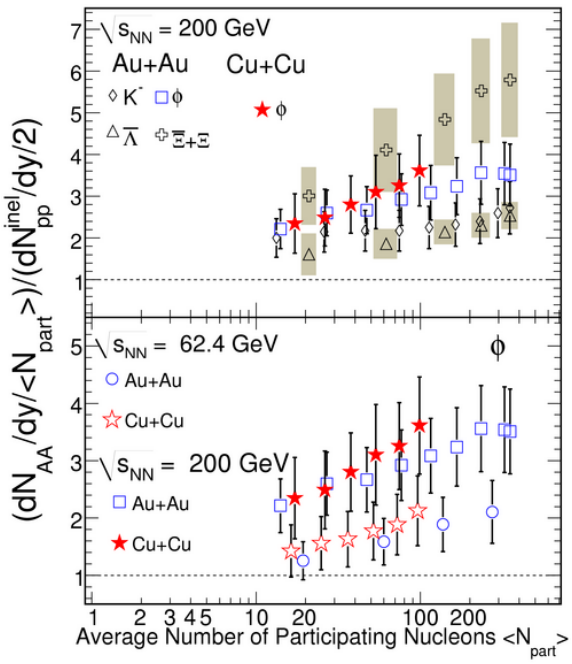

Figure 1.4: The relative yield ratios of K, ϕ, $\bar{\Lambda}$, and $\bar{\Xi} + \Xi$, normalized to $\langle N_{part} \rangle$, compared to the yields in inelastic p+p collisions are presented as functions of $\langle N_{part} \rangle$ at $\sqrt{s_{NN}} = 62.4$ and 200 GeV for Cu+Cu and Au+Au collisions. This figure is sourced from [43].

levels.

1.5.2 Jet quenching

Highly energetic particles produced by parton hard scattering lose energy by radiating gluons as they traverse the hot, dense medium created in heavy-ion collisions. This energy loss leads to the suppression of high transverse momentum particles, a phenomenon known as jet quenching. Jet quenching studies rely heavily on high-p_T particles, and the suppression of these particles indicates the presence of QGP [46]. Jet quenching can be quantified by the nuclear modification factor (R_{AA}), which is calculated as the ratio of particle yields in heavy-ion collisions to those in proton-proton collisions, normalized by the number of binary nucleon-nucleon collisions.

$$R_{AA}(p_T, \eta) = \frac{1}{T_{AA}} . \frac{d^2 N_{AA}/dp_T d\eta}{d^2 \sigma_{pp}/dp_T d\eta} \tag{1.2}$$

where T_{AA} represents the effective number of binary nucleon-nucleon collisions in

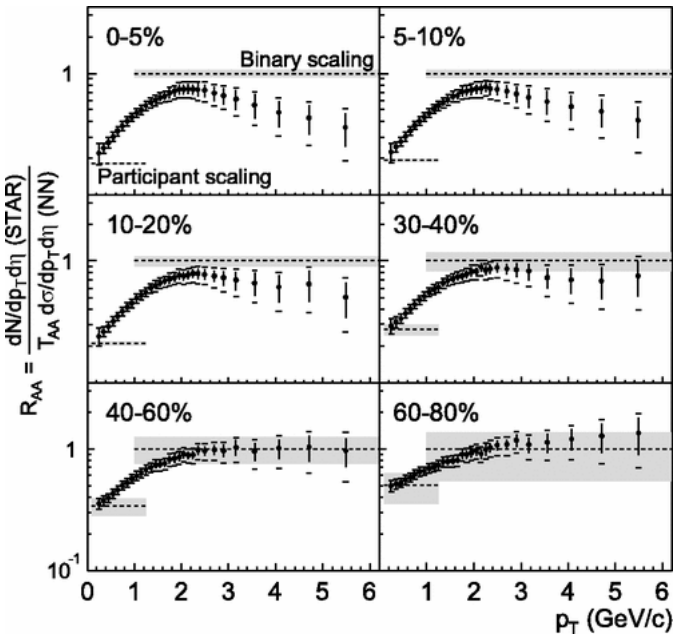

Figure 1.5: R_{AA} of inclusive charge hadron relative to NN reference spectrum in different collision centralities in Au+Au collisions at $\sqrt{s_{NN}}$ = 130 GeV. Figure is taken from [47].

the overlapping region of the two colliding nuclei. A significant suppression (i.e., R_{AA} < 1) at high p_T is a clear signature of parton energy loss in the QGP, indicating the presence of a dense and hot medium.

Figure 1.5 shows the R_{AA} for different centralities in Au+Au collisions at $\sqrt{s_{NN}}$ = 130 GeV [47]. The value of R_{AA} is significantly below unity for p_T < 6 GeV/c across all collision centralities. This suppression is most pronounced in the most central collisions, where the in-medium effects are most substantial. The reduction of R_{AA} for high p_T particles in central collisions is considered a key signature of the deconfined phase [48][49][46].

Measurement in dihadron angular correlation is another tool for studying jet quenching in heavy-ion collisions. STAR measured the dihadron angular correlations for p+p, d+Au, and Au+Au collisions at $\sqrt{s_{NN}}$ = 200 GeV [50][51].

The nuclear modification factor is also studied using another variable, defined as R_{cp}, which is the ratio of the particle yield in the most central collisions to the yield

in the peripheral collisions scaled by the average number of inelastic binary collisions.

$$R_{cp} = \frac{[(dN/dp_T)/\langle N_{bincoll}\rangle]_{central}}{[(dN/dp_T)/\langle N_{bincoll}\rangle]_{peripheral}} \tag{1.3}$$

where $\langle N_{bincoll}\rangle$ is the average number of inelastic binary collisions. In this thesis, we have studied the R_{cp} of strange and multi-strange particles.

1.5.3 Anisotropic flow

In non-central heavy-ion collisions, the overlapped region of the colliding nuclei takes on an oval shape after the collision. This creates a spatial anisotropy in the medium produced. In this anisotropic medium, particles along the short axis experience a greater force than those along the long axis. The variation in pressure gradients arising from initial spatial configurations translates into momentum anisotropy in the final state [52]. Consequently, the collective expansion of the medium is expected to provide valuable information about the QGP in non-central heavy-ion collisions. Figure 1.6 illustrates the transition from initial-state anisotropy to momentum anisotropy in the overlap zone of a collision geometry in non-central collisions. The azimuthal anisotropy is defined by the azimuthal distribution of produced particles with respect to the reaction plane, which contains the beam axis and the direction of the impact parameter. The azimuthal distribution of particles can be expressed as a Fourier series:

$$E\frac{d^3N}{d^3p} = \frac{1}{2\pi}\frac{d^2N}{p_T dp_T dy}\left(1 + \sum_{n=1}^{\infty} 2v_n \cos(n[\phi - \psi_r])\right) \tag{1.4}$$

where v_n is the n^{th} order harmonic flow coefficient and ψ_r is the reaction plane angle. The first term describes the isotropic flow, the first harmonic v_1 is referred to as the directed flow, and the second harmonic v_2 is referred to as the elliptic flow [54].

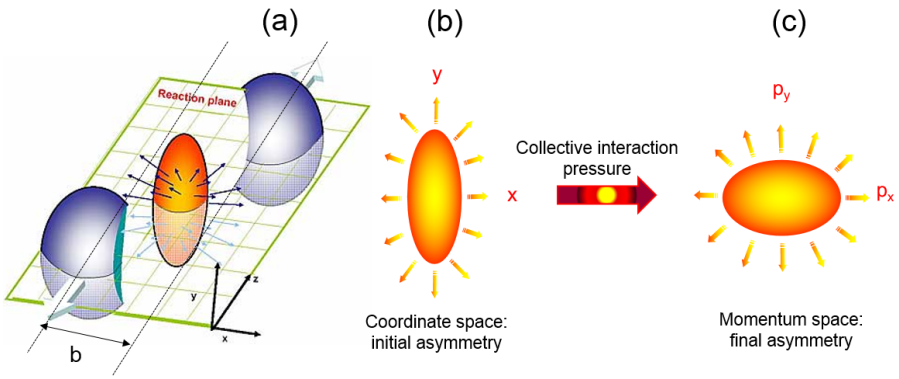

Figure 1.6: Schematic diagram illustrating the conversion of initial spatial anisotropy in the early stage of the collision to final state momentum anisotropy in the produced particles. Figure is taken from [53].

1.5.3.1 Directed flow

The pressure generated at the intersection of colliding nuclei mainly affects the particles at mid-rapidity. Directed flow (v_1) measures the sideward motion of the particles produced in the collisions. A minimum in the directed flow as a function of beam energy serves as an experimental indicator of changes in the equation of state. The softening of the equation of state is correlated with a first-order phase transition. Observing a minimum in the directed flow as a function of beam energy is indicative of such a transition [56][57][58].

Figure 1.7 presents the data for directed flow, v_1, of charged particles in 10-70% centrality Au+Au collisions at $\sqrt{s_{NN}} = 62.4$ GeV, as a function of pseudorapidity (η) [55]. These results are obtained using three different methods, showing consistency with each other. The results are also compared with Model calculations such as AMPT [59][60], RQMD [61], and UrQMD [62][63].

1.5.3.2 Elliptic flow

Elliptic flow (v_2) measures the non-uniformity in the azimuthal distribution of particle momentum in heavy-ion collisions. It is sensitive to the early-stage dynamics of the medium since the spatial anisotropy is maximum at the very beginning of the collision. Elliptic flow arises at an early time and persists until hadronization; there-

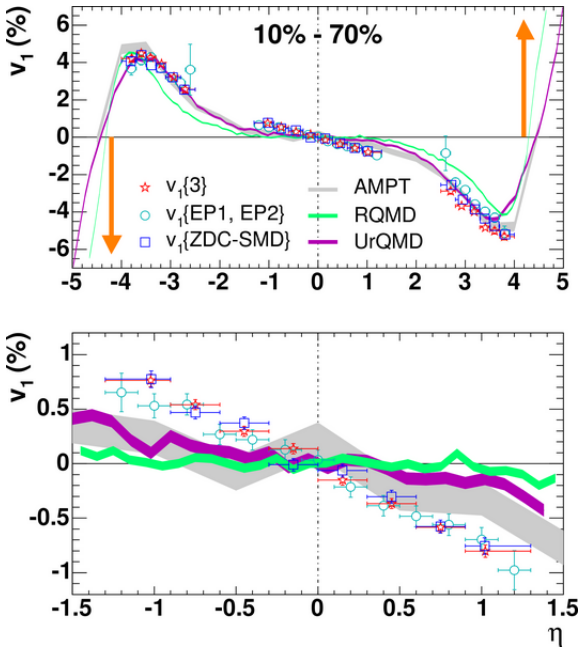

Figure 1.7: Directed flow of charged hadrons as a function of rapidity is shown. The lower figure provides a more detailed view of the mid-pseudorapidity region from the upper figure. The figure is taken from [55].

fore, the measurement of v_2 provides information about both partonic and hadronic interactions [64]. Elliptic flow is measured from transverse momentum and azimuthal angle of the detected particles.

$$v_2(p_T) = \langle cos(2(\phi - \psi_2)) \rangle_{p_T} \tag{1.5}$$

Figure 1.8 shows the measurement of v_2 for identified hadrons in Au+Au collisions at $\sqrt{s_{NN}} = 200$ GeV [65]. The experimental results are compared with hydrodynamic model predictions [52][66][67]. For $p_T >$ GeV/c, the value of v_2 remains almost constant for mesons. There is a noticeable split in the saturation levels of v_2 between mesons and baryons, which provides significant information about the flow properties of these particles. The concept of NCQ (number of constituent quarks) scaling is relevant here, where the value of v_2 is divided by the number of constituent quarks (n) in each particle. For mesons, n=2, as they consist of two quarks, and for baryons, n=3, as they consist of three quarks. Figure 1.9 shows the results from STAR in Au+Au collisions at $\sqrt{s_{NN}} = 200$ GeV, with a polynomial fit depicted as a dashed

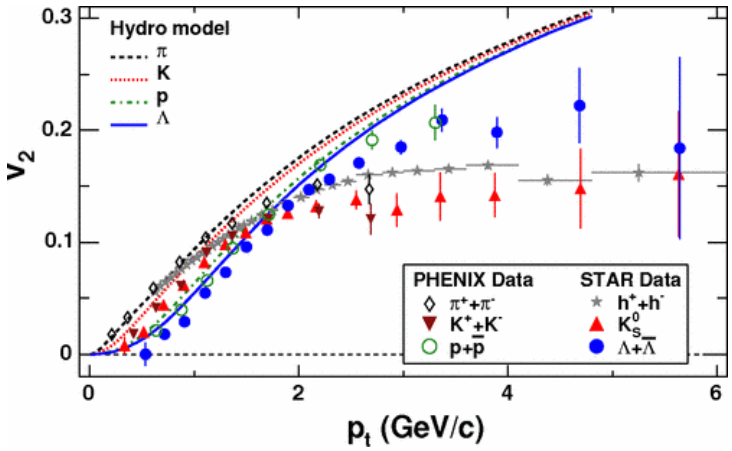

Figure 1.8: The elliptic flow (v_2) of identified hadrons, plotted against transverse momentum (p_T) in minimum bias Au+Au collisions at $\sqrt{s_{NN}} = 200$ GeV, is depicted. Solid and dotted lines in the figure represent model predictions for this system and energy level. The figure is taken from [65].

line [65]. The lower panel of the figure illustrates the data normalized by the fit function, to examine the scaling. From the figure, except for the v_2 of pions, the v_2 of all particles follows the constituent quark scaling. This NCQ scaling indicates the presence of a QGP medium and supports the idea that hadrons are generated via the coalescence of constituent quarks [68].

1.5.4 Quarkonia suppression

Heavier quarks, such as charm (c) and bottom (b), are much heavier than strange quarks. Therefore, the production of charm quarks requires high threshold energy, which is typically only present at the initial moments of a collision. When a Quark-Gluon Plasma (QGP) is formed, the $c\bar{c}$ and $b\bar{b}$ pairs find themselves immersed in a dense soup of lighter quarks and gluons. This abundance of surrounding particles disrupts the binding forces between the charm and anti-charm quarks (or bottom and anti-bottom quarks), an effect referred to as Debye color screening [69]. These conditions lead to various bound states known as quarkonia, such as J/ψ and Υ. The pronounced suppression of quarkonia in heavy-ion collisions, a phenomenon first proposed by Tetsuo Matsui and Helmut Satz [70], is a prominent indication of QGP, known as quarkonia suppression.

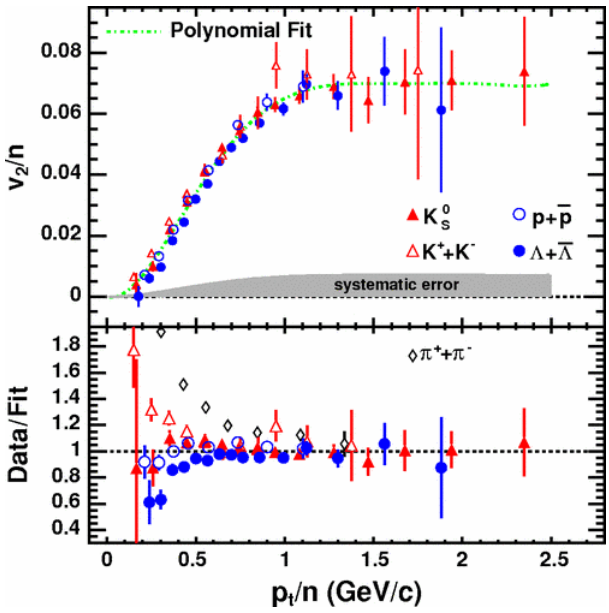

Figure 1.9: v_2/n as a function of p_t/n, where n is the number of constituent quarks measured by the STAR experiment for various hadrons. Figure is taken from [65].

In particular, the J/ψ meson, which consists of a charm quark and its antiparticle, is an essential tool for investigating the QGP. The extent of quarkonia suppression is influenced by both the binding energy of these particles and the temperature within the QGP. As a result, instead of recombining into $c\bar{c}$ or $b\bar{b}$ bound states, open charm and bottom quarks are more likely to pair with other quarks during the final stages of the collision.

Figure 1.10 shows the R_{AA} for J/ψ as a function of $\langle\ N_{part}\ \rangle$ in Pb-Pb collisions at $\sqrt{s_{NN}}$ = 2.76 TeV in the ALICE experiment at the LHC [71][72][73], along with comparisons to PHENIX results at the RHIC [74]. The R_{AA} of J/ψ is less than unity, indicating the suppression of J/ψ at both RHIC and LHC energies. The R_{AA} of J/ψ is centrality-dependent at PHENIX, while at LHC energies, it shows no centrality dependence. These observations support the formation of a QGP medium that suppresses J/ψ production while a fraction of $c\bar{c}$ pairs recombine, enhancing J/ψ production.

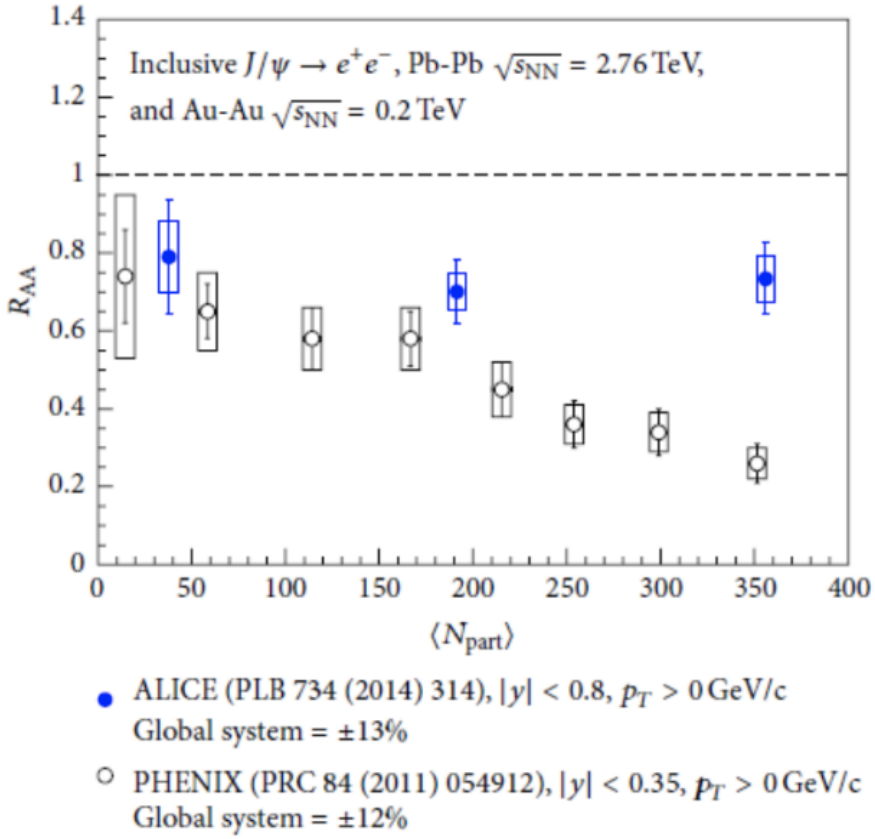

Figure 1.10: R_{AA} of J/ψ as a function of $\langle\ N_{part}\ \rangle$ at midrapidity in Pb-Pb collisions at $\sqrt{s_{NN}} = 2.76$ TeV compared with PHENIX result at $\sqrt{s_{NN}} = 200$ GeV. Figure is taken from [75].

1.5.5 Global Spin Polarization of hyperons

As discussed in earlier sections that directed and elliptic flow measurements at RHIC provide information about the QGP phase transition and fluidity of the matter created in the heavy ion collisions, respectively. Measurement of global spin polarization of hyperons in non-central collisions provides information about the fluid properties of the matter. In non-central collisions, the colliding nuclei carry a large angular momentum ($O(10^3) - O(10^5)$), which can be transferred to the medium created at the time of collision. The spin of the particles produced in the collision will interact with the system angular momentum and as a result one should observe spin polarization of the produced particles. For the experimental measurements weakly decaying hyperons plays an important role as their decay daughter have preferential direction

as the parent spin direction, which is polarized along the system angular momentum direction. The measurement of global spin polarization of Λ ($\overline{\Lambda}$) hyperons from the STAR experiment has observed non-zero polarization in 20-50 % Au+Au collisions and its value increases as the center of mass energy decreases [76] [77] [78]. A detailed study of differential measurement of spin polarization of Λ ($\overline{\Lambda}$) hyperons for transverse momentum, centrality and rapidity dependence is reported in [79] [80]. Within the detector acceptance and uncertainties no transverse momentum and rapidity was observed.

1.6 Thesis outline

The results presented in this thesis analyze the data of Au+Au collisions at $\sqrt{s_{NN}}$ = 19.6 GeV recorded by the STAR detector at RHIC in the year 2019 under the BES-II program. The thesis particularly focuses on the measurement of strange and multi-strange particles (K^0_s, Λ, $\overline{\Lambda}$, Ξ^-, $\overline{\Xi}^+$, Ω^-, $\overline{\Omega}^+$) to study the properties and dynamics of the medium created in the collisions. These particles are particularly interesting because strange quarks are relatively heavy compared to up and down quarks, the primary constituents of protons and neutrons. As a result, the energy required to create strange quarks is comparatively higher. Therefore, all strange hadrons must be formed from the medium created after the collision. This characteristic makes strangeness an excellent probe for studying the extreme conditions and dense matter generated in these high-energy collisions. For this purpose, different observables such as nuclear modification factor (R_{cp}), ratio plots including baryon-to-meson ratios, and rapidity spectra of strange and multi-strange particles are studied.

Despite significant advances in understanding the quark-gluon plasma (QGP) and the dynamics of heavy-ion collisions, the mechanisms underlying strangeness production remain incompletely understood, particularly at intermediate energies like $\sqrt{s_{NN}}$ =19.6 GeV [37]. This energy regime, accessible via the STAR experiment, is critical for probing the properties of the QGP near the threshold energy where the transition from hadronic matter to QGP is expected to occur. Existing studies from the BES-I

program have provided insights into the medium properties at low collision energies.

The results from BES-I on strange and multi-strange particles have indicated potential medium changes. The R_{cp} ratio compares the particle yields in central collisions to that in peripheral collisions, normalized by the average number of inelastic binary collisions. The R_{cp} results on strange and multi-strange particles at $\sqrt{s_{NN}}$ = 7.7 - 19.6 GeV from BES-I hints at decreasing partonic energy loss effect with decreasing beam energies [37]. The enhancement of the baryon-to-meson ratio at intermediate p_T in central to peripheral collisions is interpreted as a consequence of hadron formation through parton recombination [37]. Therefore, they are expected to be sensitive to parton dynamics of the collision system. The $\overline{\Lambda}/K^0_s$ ratio from BES-I shows the baryon enhancement at intermediate p_T [37]. However, these results are constrained by limited statistics and are only applicable at mid-rapidity (|y|<0.5) due to limited detector acceptance.

The BES-II program, with high statistics and detector upgrades, especially the iTPC, allows to further explore the results on strange and multi-strange particles in Au+Au collisions at $\sqrt{s_{NN}}$ =19.6 GeV with extended p_T reach and rapidity coverage. With the upgrade to the iTPC in BES-II, the rapidity-dependent study of different observables became possible, allowing to study the new insights on the collision dynamics, unlike the previous measurements that were restricted to mid-rapidity (|y|<0.5). In this context, we studied the rapidity dependence of nuclear modification factor (R_{cp}), ratio plots such as baryon-to-meson ratios (Λ/K^0_s, Ξ/K^0_s, Ω/K^0_s), and integrated yield ($\frac{dN}{dy}$), along with cross-checking the transverse momentum (p_T) spectra with BES-I measurements at mid-rapidity (|y|<0.5). Moreover, at low collision energies, such as $\sqrt{s_{NN}}$ = 19.6 GeV, the p_T spectra of particles are different from those of antiparticles. Therefore, we studied the R_{cp} of particles and antiparticles separately, unlike the previous measurements from BES-I, where the R_{cp} for particles and antiparticles were combined, possibly due to low statistics.

The rapidity density of strange baryons may give insight into the baryon stopping mechanism [81]. In order to study the rapidity spectra of particles and antiparticles,

we took rapidity bin width $\Delta y = 0.25$ for K^0_s, Λ, $\overline{\Lambda}$, Ξ^-, $\overline{\Xi}^+$, and $\Delta y = 0.3$ for Ω and $\overline{\Omega}^+$ within the total rapidity range of $|y|<1.5$ for K^0_s, $|y|<1.0$ for Λ, $\overline{\Lambda}$, Ξ^-, $\overline{\Xi}^+$, and $|y|<0.9$ for Ω^- and $\overline{\Omega}^+$. We studied the R_{cp} and baryon-to-meson ratios of these particles at mid-rapidity ($|y|<0.5$) as well as at extended rapidities at $0.5<|y|<1.0$, Moreover, the high statistics in BES-II allow for the extension of the p_T reach in the high p_T region, and the upgrade in iTPC helps in accessing the low p_T reach for different particles.

The plan of this thesis is as follows: In Chapter 2, the technical details of the STAR experiment are discussed. Chapter 3 discusses the strange hadron reconstruction. In Chapter 4, we discuss the results obtained from BES-II. The summary and future prospects are discussed in Chapter 5.

Chapter 2

Experimental setup

2.1 Relativistic Heavy Ion Collider (RHIC)

The Relativistic Heavy Ion Collider (RHIC) complex, situated at Brookheaven National Laboratory (BNL), in USA, is a world-class facility for particle acceleration at relativistic speed. It started operation in 2000 in the collider mode with Au+Au collisions. It was designed to operate at high collision luminosity over a diverse range of beam energies. It is not only constrained to Au+Au collision, but it is the most versatile particle collider that includes the collisions from polarized p+p and p+Au to heavy-ion collisions such as d+Au, Cu+Cu, Zr+Zr, Ru+Ru, U+U, etc., at the varying center of mass energies. It can also operate in both the collider as well as the fixed target mode. These variations in colliding particle species at different center of mass energies make RHIC a reasonable particle collider to scan the QCD phase diagram at different regions of interest. The highest energy achieved at RHIC for heavy-ion beam e.g., $^{197}_{79}Au$ ions is 100 GeV/u and that for polarized protons is 250 GeV/u. In early days there were four experiments STAR, PHENIX [82], PHOBOS [83] and BRAHMS [84]. The PHOBOS and BRAHMS experiments finished data taking between the years 2000-2006. The PHENIX experiment ended its operations in 2018. The STAR experiment is the longest running experiment at RHIC.

Figure 2.1 shows the schematic of particle accelerators that make up the RHIC complex. The initial stage starts with the Electron Beam Ion Source (EBIS) [86][87]

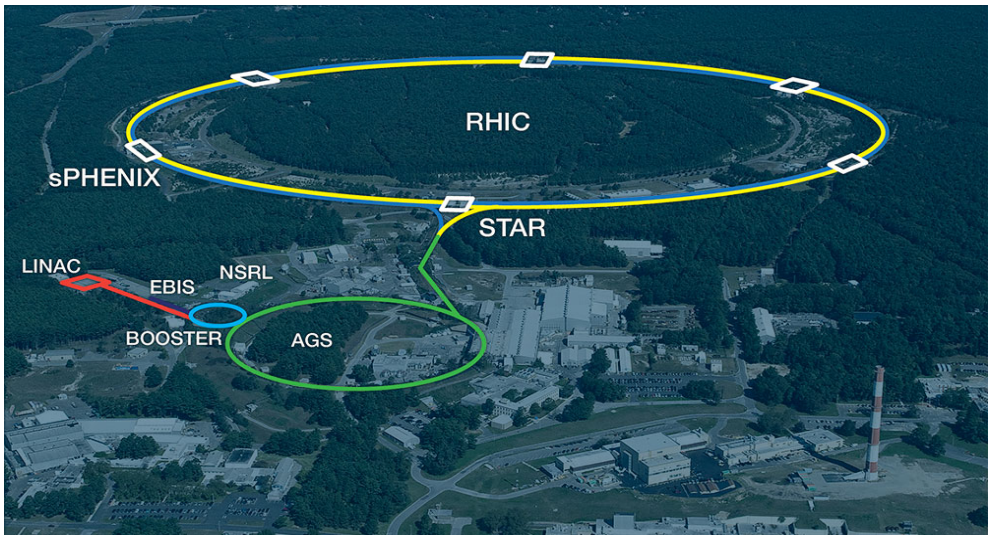

Figure 2.1: An overhead view of the RHIC complex highlighting the positions of the STAR and sPHENIX detectors at Brookhaven National Laboratory. The figure is taken from [85].

which acts as the pre injector system for RHIC. The EBIS is simpler to operate and easier to maintain than the Tandem Van de Graff generator which was previously used as RHIC pre-injector. Unlike the Tandem Van de Graff generators, the EBIS does not require stripping before the Booster which results in more stable beams. The EBIS is capable of producing high charge state ion beams from any heavy-ion species. These ion beams are first accelerated by two small linear accelerators and then passed to the Booster synchrotron for further acceleration.

The Booster synchrotron, a potent circular accelerator, accelerates the ions to 37% of the speed of light. As $^{197}_{79}$Au ions leave the Booster, they achieve a charged state of Au^{77+}. The ions are then transferred from the Booster to the much larger Alternating Gradient Synchrotron (AGS). In the AGS, ions accelerate further to 8.86 GeV/u, achieving up to 99.7% of the speed of light. Once the ions attain their maximum speed in the AGS, they are directed through a beam line to the RHIC, where they are completely stripped of electrons to stabilize at a charge state of Au^{77+}. At the end of this beam line, switching magnets route the ion beams to travel either clockwise or counterclockwise within the RHIC rings, which have a circumference of 2.4 miles and are equipped with 1740 helium-cooled superconducting magnets to keep the ions

on their circular track.

2.2 The Solenoidal Tracker At RHIC (STAR)

The STAR detector was designed to record the aftermath of the relativistic collisions. The purpose was to search for the signatures of QGP and investigate its properties and thus enhance the understanding of the QCD phase diagram [88]. The STAR detector is a massive detector system with excellent particle identification capabilites that consists of many sub-detectors each of which perform a specific task. Figure 2.2 shows the schematic view of the STAR detector.

The STAR detector is capable of tracking and identifying a large number of particles, both charged and neutral, that are produced in the collisions. The STAR sub-detectors can broadly be divided into two categories - the fast detectors and the slow detectors. The fast detector category includes the Vertex Position Detector (VPD), Beam-Beam Counters (BBC), Zero Degree Calorimeter (ZDC), Barrel Electromagnetic Calorimenter (BEMC), End-cap Electromagnetic Calorimeter (EEMC) etc. The slow detector category includes the Time Projection Chamber (TPC), Time of-Flight (TOF) etc. In the STAR detector system, the fast detectors primarily serve as the trigger detectors as they control events selection by triggering the slow detectors. The main utility of such trigger detectors is to select an event where an interaction of interest occurred. The slow detectors like the TPC, on the other hand, cannot record every collision but provide detailed information on the charged particles when triggered.

The TPC is a cylindrical detector which covers a pseudo-rapidity range of $|\eta|\leq 1.5$.[1] The TOF, completed in 2010, is installed immediate top of the TPC covering $|\eta|\leq 1$. Both the TPC and the TOF cover complete azimuthal angle ($\Delta\phi = 2\pi$). The BEMC, outside of the TOF, completely covers the TPC with an area of $60m^2$, covering $|\eta|\leq 1$,

[1] the upgrade in iTPC in BES phase-II enhances the previous range of η from 1 to 1.5, discussed more in section 2.2.1.1

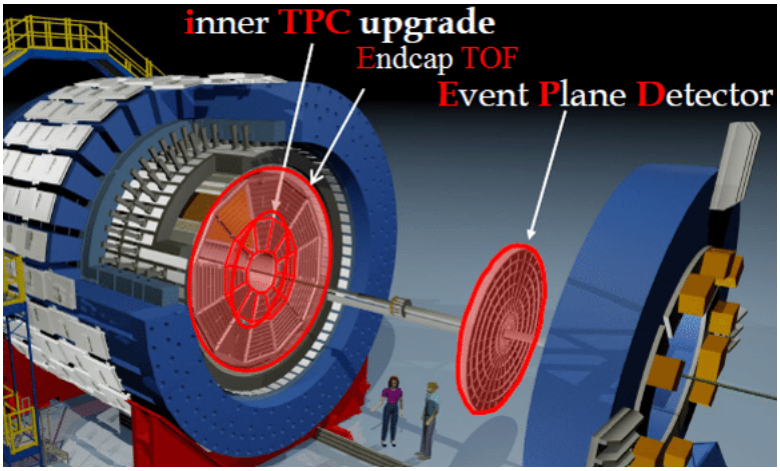

Figure 2.2: A schematic illustration of the STAR detector. This image is taken from [89].

$\Delta\phi = 2\pi$. It is used to trigger high p_T events and makes it possible to reconstruct π^0 and direct photons upto 25-30 GeV/c [90]. The EEMC, mounted at one side of the STAR, extends the rapidity coverage of BEMC with $1.086<\eta<2.0$ and $\Delta\phi = 2\pi$. All these detectors are encased within the STAR magnet coils and the Iron Yoke, which generate a consistent magnetic field of ± 0.5 T along the beamline. The trajectories of the charged particles produced after the collisions are bended under the influence of the magnetic field. This bending of the charged particles is used to measure the momentum of the particles.

A pair of sub-detectors like the ZDCs, BBCs, VPDs, are positioned on either side of the center of the detector. These detectors apart from triggering the events, also used for beam monitoring. The ZDCs are basically the hadron calorimeters used to detect neutrons [91]. They are located 18m away on either sides from the interaction point. The VPDs, components of the TOF system, deliver the initial timing of the collision necessary for measuring particle flight times. These detectors are positioned 5.6 meters from the center of the detector on either side. The BBCs, on the other hand, ideal for low multiplicity events in p+p collisions, consist of scintillator detectors located 3.5 meters from each side of the detector. Among the various detectors, the Time Projection Chamber (TPC) serves as the primary device for tracking and identifying particles.

2.2.1 The Time Projection Chamber

The Time Projection Chamber (TPC) is one of the main detectors in the STAR detector system [92]. It can detect both primary as well as the secondary charged particles that are produced from the decay of short-lived primary particles. The TPC is a cylindrical volume which is 4.2m long and 4m in diameter. It is filled with P10 gas which is a mixture of 10% methane and 90% argon regulated at 2mbar above the atmospheric pressure [93]. Methane is a good absorber of energy whereas argon is stable and relatively less expensive and is a primary source of ionization electron in the TPC. Also, argon is an inert gas, which ensures that it does not chemically interact with the materials used in the detector. The TPC is located at the center in the STAR detector system which covers the interaction vertex where the collision takes place. It covers the entire azimuthal angle around the beamline in the x-y plane. Figure 2.3 shows a schematic diagram of the TPC.

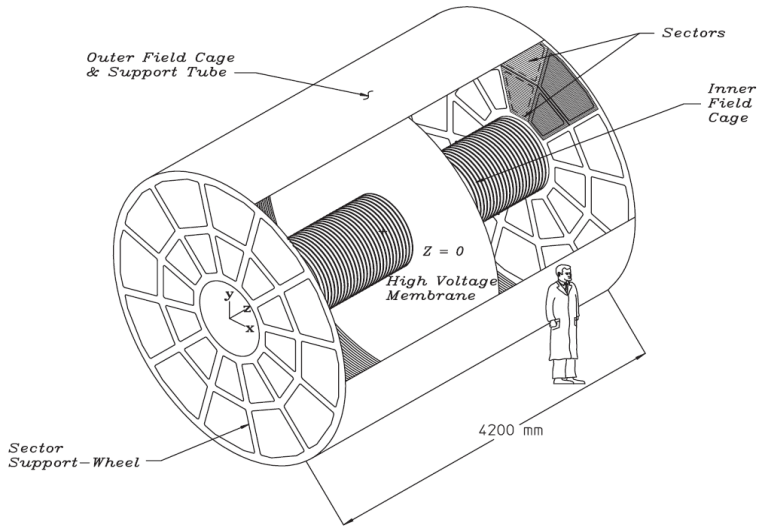

Figure 2.3: A schematic figure of the STAR TPC showing the IFC, OFC, CM and 12 sectors on both sides of the TPC. Figure is taken from [92].

The TPC features two concentric field cage cylinders: the Inner Field Cage (IFC) with a radius of 0.5m, and the Outer Field Cage (OFC) with a radius of 2m. The TPC is divided into two equal sections of 2.1 cm each by a conductive central membrane (CM) at the core. This membrane is maintained at a negative potential of 28kV,

while the end-caps at both ends of the TPC are grounded. These elements collectively generate a uniform electric field of 135 V/cm within the chamber.

The Multi-Wire Proportional Chambers (MWPC) with readout pads form the readout system of the TPC. At both ends of the TPC, there are 12 sectors in trapezoidal shape arranged along the ϕ direction. In each sector, there are MWPC, gating grids and the readout pads. These sectors are broadly divided into inner sector and the outer sector. The inner sector has 13 discrete padrows where pads of size 2.85mm×11.5mm are used. Unlike the inner sector, the outer sector is more densely packaged forming a continuos pad coverage, where pads of comparatively bigger size 6.2mm×19.5mm are used. The outer sector has continuous pad coverage in order to improve the tracking resolution as well as to optimize the dE/dx resolution. The inner sectors, however, use smaller pad size to optimize for a good two-hit resolution in high track density region in the TPC [92].

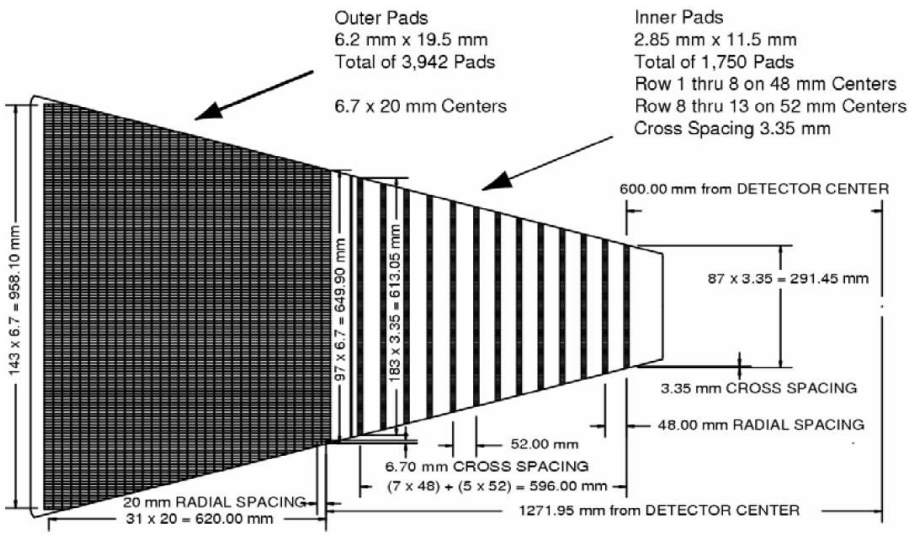

Figure 2.4: The layout of the STAR TPC anode sector showing the inner and the outer section. The outer section has more number of pads than the inner section. Figure is taken from [92].

The central membrane serves as the cathode, while the ends of the TPC, equipped with pad planes, function as the anode. Under the influence of the electric field, the clusters of secondary electrons, produced through ionization, drift towards the anode.

As the drifting electrons reach a grid of 20 μm anode wires, they create an avalanche of charge. The positive ions generated during this avalanche induce a temporary image charge on the pad plane beneath the anode wires. This image charge is then detected by the readout electronics.

The x and y coordinates of the ionization clusters are obtained by analyzing the signals from adjacent pads within a single row. The z-coordinate is determined by measuring the drift time from the origin of the cluster to the end-caps and then dividing this time by the average drift velocity of the electrons. After determining the x, y, and z coordinates, a helical fit is executed using the TPC track reconstruction algorithm to determine the trajectory of the particle and calculate its momentum.

Within the TPC, charged particles lose energy due to their interactions with the gas, and this process of energy loss, quantified as dE/dx, serves as a critical method for identifying types of particles. The Bethe-Bloch formula, referenced below, mathematically describes this energy loss [94]:

$$\left\langle -\frac{dE}{dx}\right\rangle = Kz^2\frac{Z}{A}\frac{1}{\beta^2}\left[\frac{1}{2}In\frac{2m_ec^2\beta^2\gamma^2T_{max}}{I^2} - \beta^2 - \frac{\delta(\beta\gamma)}{2}\right] \tag{2.1}$$

In the above equation, z represents the charge of the particle, while Z and A are its atomic number and mass number, respectively. β = v/c, defined as v/c (velocity of the particle relative to the speed of light), m_e represents mass of electron, T_{max} the maximum kinetic energy transferable to a free electron in a collision, and $\delta(\beta\gamma)$ is the associated correction term.

From equation 2.1, it is clear that the kinetic energy deposition is different for particles of different masses. The particle identification works very well for low momentum particles but for high momentum particles, the energy loss becomes less mass dependent. Pions and kaons can be distinguished from each other up to approximately 0.7 GeV/c, and pions and kaons can be separated from protons up to around 1.1 GeV/c. Beyond these points, the bands start to overlap, making it difficult to identify particles using only the TPC. Figure 2.5 shows the energy loss of

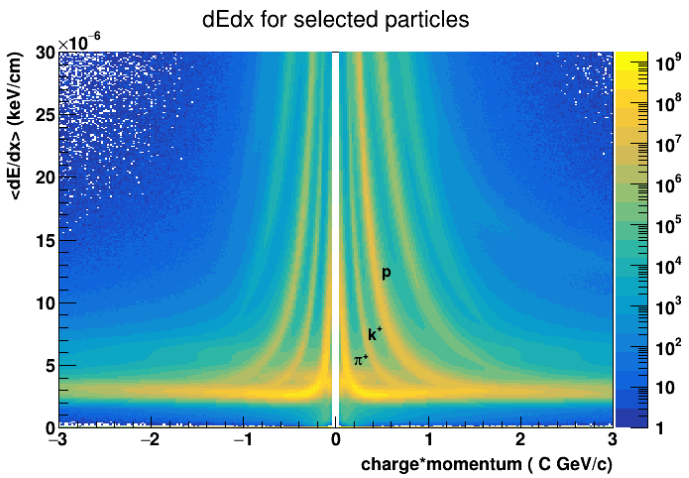

Figure 2.5: Ionization energy loss of charged particles plotted as a function of rigidity (charge times momentum) within the TPC during Au+Au collisions at $\sqrt{s_{NN}} = 19.6$ GeV.

different particles in Au+Au collisions at $\sqrt{s_{NN}} = 19.6$ GeV.

2.2.1.1 Upgrade in iTPC

For the BES-II program, the inner sector of the Time Projection Chamber (iTPC) was upgraded [40]. Initially, there were 13 pad rows on the inner sectors of the TPC. There were a total of 1750 pads, with each pad measuring 2.85 mm × 11.5 mm. Now, with upgrades in iTPC, there are a total of 3370 pads per sector which is roughly double the number of pads in the previous TPC inner sectors. These additional pad rows enhance the tracking of charged particles at small angles relative to the beam-line. The upgrades in iTPC also provide better acceptance of low momentum tracks along with better resolution for dE/dx. Apart from lowered transverse moementum (p_T) thresholds and better dE/dx resolution, the upgrade in iTPC also enhances the rapidity coverage upto $|\eta| \leq 1.5$ as compared to the previous TPC coverage of $|\eta| \leq 1$. The enhanced rapidity coverage in BES-II makes completely new physics analysis possible for the first time in STAR.

The improved acceptance of the iTPC at low p_T and the improved track efficiency is of particular interest for the reconstruction of strange and multi-strange particles such as K^0_s, $\Lambda(\overline{\Lambda})$, $\Xi^-(\overline{\Xi}^+)$, $\Omega^-(\overline{\Omega}^+)$. The enhanced measurement capabilities of the

TPC after the iTPC upgrades extend the previous results from mid-rapidity $|y|<0.5$ to higher rapidity ranges and hence allow the study of the rapidity density distribution of strange and multi-strange particles. This became possible because with the upgrade in iTPC, low momentum particles as well as those particles that are very close to the beamline, can also be identified. In this thesis, we present the rapidity density distribution of strange and multi-strange particle yields as a function of rapidity, along with cross-checking the previous results from BES-I at mid-rapidity $|y|<0.5$.

This page is intentionally left blank

Chapter 3

Experimental analysis details and techniques

This chapter of the thesis explains the technical details involved in analyzing Au+Au collisions at $\sqrt{s_{NN}}$=19.6 GeV. The dataset used for the analysis, event selection criteria, and quality assurance plots are discussed in detail here. Further, it discusses the strange hadrons (K^0_s, Λ, $\overline{\Lambda}$, Ξ^-, $\overline{\Xi}^+$, Ω^-, $\overline{\Omega}^+$) reconstruction, their decay topology, selection criteria based on decay topology, invariant mass distribution, signal extraction, estimation of systematic uncertainties, and transverse momentum spectra.

3.1 Dataset and Event Selection

The analysis for the production of strange and multi-strange particles starts with the selection of the minimum bias trigger followed by the vertex cuts for good events selection. The minimum bias trigger (or trigger with as little bias as possible without imposing any specific selection criteria on data collection) corresponds to the trigger condition where a coincidence of the signals from the vertex position detectors (VPDs), zero-degree calorimeter (ZDCs) and/or beam counters is obtained.

A vertex position cut was set at $|V_z|$<145 cm along the beam direction from the center of the TPC, and a radial distance cut of V_r<2 cm was applied. The variable V_r represents the distance from the collision vertex to the beam pipe in the transverse

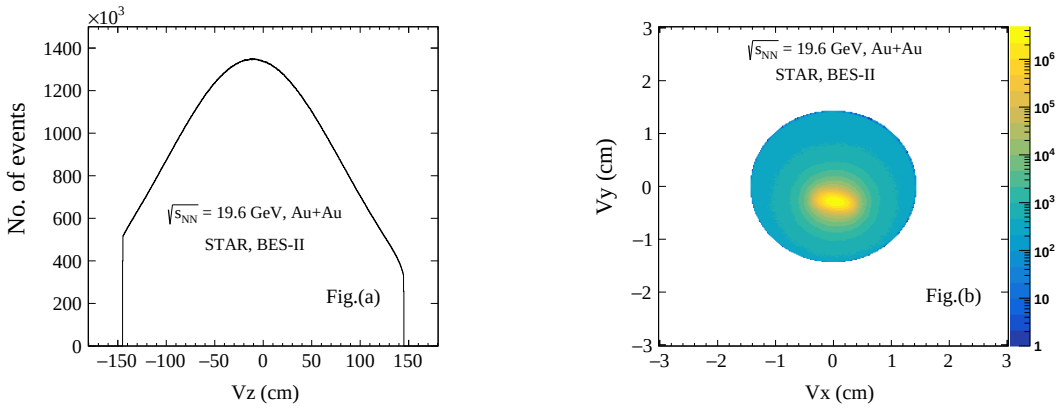

Figure 3.1: Fig. (a) on the left illustrates the V_z distribution for Au+Au collisions at $\sqrt{s_{NN}}$ = 19.6 GeV, while Fig. (b) on the right depicts the V_r distribution in the same collision settings.

plane and is defined as $V_r = \sqrt{V_x^2 + V_y^2}$. The V_r cut is crucial to eliminate any event contamination from interactions occurring with the beam pipe, which has a radius of 3 cm. Figure 3.1 shows V_z and V_r distributions after applying the cuts in Au+Au collisions at $\sqrt{s_{NN}}$ = 19.6 GeV.

The higher beam luminosity in BES-II increases the probability of event pile-up. The pile-up of events occurs when the remnants of multiplicities from previous events contribute in the measured multiplicity of the current event. In other words, pile-up events occur when two or more events are reconstructed as a single event. To remove such pile-up events, the correlation between the number of tracks measured by the TPC and the TOF-matched tracks (TPC tracks that are matched to the TOF detector) is studied. Figure 3.2 shows the correlation between the reference multiplicity measured by the TPC and the TOF-matched tracks and the reference multiplicity distribution before and after the pile-up cut in Au+Au collisions at $\sqrt{s_{NN}}$ = 19.6 GeV.

After the good events selection, the strange and multi-strange hadrons were reconstructed. The next section discusses about the properties, decay topology and selection criteria for the reconstruction of strange and multi-strange hadrons.

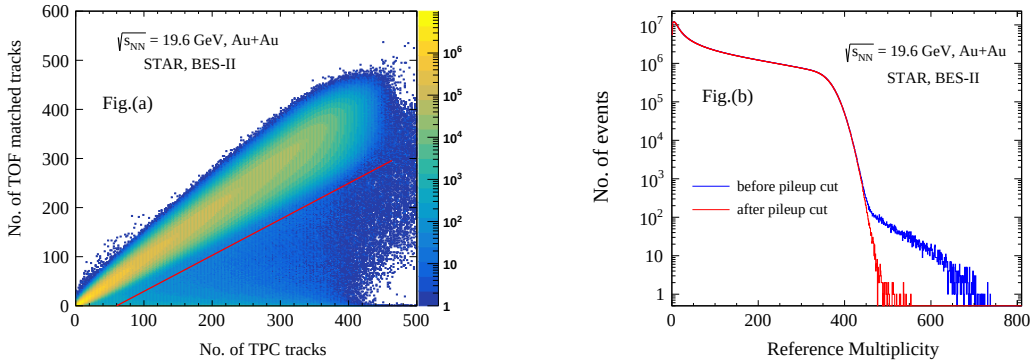

Figure 3.2: Fig. (a), displayed on the left, presents the correlation between the number of tracks matched with the TOF and those registered by the TPC. Events falling below the red line are categorized as pile-up and are excluded from the analysis. Fig. (b) on the right demonstrates the reference multiplicity distribution as measured by the TPC. Here, the blue line represents data before the exclusion of pile-up events, while the red line indicates the data after these events have been removed.

3.2 Strange hadrons reconstruction

In heavy-ion collisions like the Au+Au collisions, a large number of particles are produced. These particles can be broadly divided into two categories: long-lived particles and short-lived particles. Long-lived particles have enough lifetime to be tracked by tracking detector systems like the STAR TPC, TOF, etc. The particles in this group are generally stable particles which include (anti-)proton p($\overline{p}$), electrons and positrons ($e^{\pm}$), and other particles which have large decaylength (cτ) like mesons which include muon $\mu^{\pm}$, $\pi^{\pm}$ and $K^{\pm}$. On the other hand, short-lived particles are those particles that decay within the tracking detector system and hence can only be reconstructed indirectly using their decay constituents. Such particles include meson like K^0_s, strange hyperons (Λ, $\overline{\Lambda}$, Ξ^-, $\overline{\Xi}^+$, Ω^-, $\overline{\Omega}^+$), hypernuclei ($^3_{\Lambda}$H, $^4_{\Lambda}$H, $^4_{\Lambda}$He) etc. The strange hadrons (K^0_s, Λ, $\overline{\Lambda}$, Ξ^-, $\overline{\Xi}^+$, Ω^-, $\overline{\Omega}^+$), created in heavy-ion collisions, are of particular interest as they serve as an important probe to witness the evolution process of the medium created in the collision. These particles are created at the interaction vertex, travel a certain distance, and then undergo a weak decay into their daughter constituents, for instance, $K^0_s \rightarrow \pi^+ + \pi^-$. In case of multi-strange hyperons decay such as $\Xi^-(\overline{\Xi}^+)$, $\Omega^-(\overline{\Omega}^+)$, a neutral daughter $\Lambda(\overline{\Lambda})$ is formed which

further decays weakly into a pair of charged particles $p(\bar{p})$, $\pi^-(\pi^+)$. These strange hadrons can be reconstructed via the topology of their charged decay products by identifying the tracks that they form in the volume of the TPC.

In general, the tracks of the charged particles produced in a collision can be divided into two groups: primary tracks and secondary tracks. The primary tracks are tracks of particles that are produced directly in the collisions, while secondary tracks originate from the decay vertex of the short-lived particles. The strange hadrons (K^0_s, Λ, $\overline{\Lambda}$, Ξ^-, $\overline{\Xi}^+$, Ω^-, $\overline{\Omega}^+$) are reconstructed by selecting the secondary tracks. One of the effective ways to select the secondary tracks is to take the distance of the closest approach (DCA) of the tracks away from the primary vertex. This helps in selecting the tracks coming from the decay vertex of mother particles and not from the primary vertex. In the STAR experiment, currently, two methods are used for the reconstruction of short-lived strange particles - the Helix method and the KFParticle. The work presented in this thesis is done using the Helix method. We also did a comparison study of two methods for the Λ, $\overline{\Lambda}$, and the outcome of the study is discussed here.

3.2.1 Strange V0 reconstruction using Helix Method

Strange particles such as K^0_s, Λ, $\overline{\Lambda}$ are reconstructed via the detection of their weak decay channels $K^0_s \rightarrow \pi^+ + \pi^-$, $\Lambda(\overline{\Lambda}) \rightarrow \mathrm{p}(\overline{p}) + \pi^-(\pi^+)$. Table 3.1 lists the properties and weak decay channels of the V0 particles (K^0_s, Λ, $\overline{\Lambda}$) [95]. After being produced at the primary vertex, these particles travel a certain distance and then undergo a weak decay into a pair of charged particles, forming a V-shaped topology (V0 decay). The reconstruction of these particles is carried out by combining the positive and negative tracks measured by the TPC. Figure 3.3 shows the decay topology of the strange V0 particles [96].

The central value of the truncated mean of the ionization energy loss <dE/dx> measured by the TPC is well defined by the Bichsel function [97] for each particle

Table 3.1: Strange V0 particles and their weak decay channels [95].

V0 particles	Weak decay channels	Branching Ratio	$c\tau$ (cm)
K^0_s	$\pi^+\pi^-$	$69.20 \pm 0.05\%$	2.6942
$\Lambda(\overline{\Lambda})$	$p(\overline{p}) + \pi^-(\pi^+)$	$63.9 \pm 0.5\%$	7.89

species. The quantity $n\sigma_{par}$ defined as,

$$n\sigma_{par} = \frac{1}{\sigma_{par}} log \frac{< dE/dx >_{measured}}{< dE/dx >_{predicted}} \tag{3.1}$$

estimates the deviation of the measured $< dE/dx >$ from the theoretical calculations in terms of the number of standard deviations where σ_{par} represents the <dE/dx> resolution of the TPC, $< dE/dx >_{measured}$ represents the observed ionization energy loss for a specific particle species, $< dE/dx >_{predicted}$ denotes the theoretical value calculated using the Bichsel function. For the reconstruction of V0 particles, a selection criterion of $|n\sigma_{par}| < 4.0$ was applied to include all charged daughter particles. Further, the charged tracks measured by the TPC were required to consist of more than 15 hit points for the reconstruction of strange V0 particles. A DCA between the identified positive and negative tracks is calculated assuming they are originated from the decay vertex of the V0 candidate. Apparently, the distance between the closest points of the two daughter tracks must be zero because the two daughters originated from a V0 decay vertex. Due to the position resolution of the tracks, a certain distance tolerance is accepted [98]. The decay vertex of the V0 candidate is identified by calculating the average position of the closest approach points of the two daughter tracks.

A DCA is calculated from the primary vertex to the V0 helix which helps in rejecting the random combination of charged tracks. It also helps in selecting the primary V0 candidates as secondary V0 reconstruction is also done in case of multi-strange hyperons (Ξ^-, $\overline{\Xi}^+$, Ω^-, $\overline{\Omega}^+$) reconstruction. The decaylength of the V0 candidate is calculated by measuring the distance from the primary vertex to the decay vertex. A cut on decaylength is set to reduce the combinatorial background from the primary

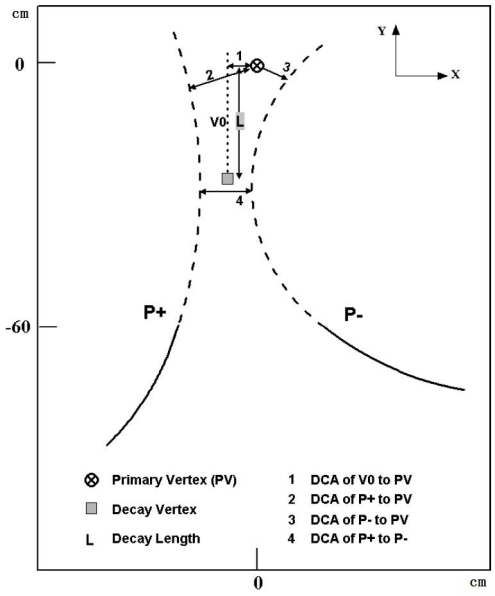

Figure 3.3: The topology of strange V0 decay is described, where P_+ denotes positively charged particles and P_- denotes negatively charged particles. Figure is taken from [96].

tracks. Since the V0 daughters do not directly come from the primary vertex, where the interaction takes place, but are produced at the decay vertex, a cut on DCA between each daughter track and the primary vertex (PV) is also applied to reduce the combinatorial background. Table 3.2 shows the default topological cuts used for K^0_s, $\Lambda(\overline{\Lambda})$ reconstruction in this analysis.

To exclude the residual background arising due to the particle misidentification, veto cuts were also considered for the reconstruction of K^0_s. A proton from Λ decay may be misidentified as π^+ and combined with π^- daughter of Λ. This contributes in the residual background in K^0_s reconstruction. To avoid such residual background in K^0_s reconstruction, the π^+ daughter from K^0_s was treated as the proton daughter of Λ for invariant mass calculations. In a similar approach, the π^- daughter from K^0_s was treated as the antiproton daughter of $\overline{\Lambda}$. If these combinations fell within the invariant mass range of [1.1057, 1.165] GeV/c^2, the K^0_s candidate was excluded.

A critical topological criterion for identifying V0 weak decays involves the pointing angle. This angle is characterized by the deviation between the momentum vector of

Table 3.2: Topological cuts used for the reconstruction of V0 particles (K^0_s, Λ, $\overline{\Lambda}$). $\vec{p}_{V0}$ and $\vec{r}_{V0}$ represent the momentum and the position vector of the V0 particles respectively and $\vec{r}_{PV}$ denote the primary vertex position vector.

Cuts	K^0_s	$\Lambda(\overline{\Lambda})$
DCA of V0 to PV	< 0.8 cm	< 0.8 cm
DCA of daughters to PV	> 0.7 cm	> 1.0 cm
DCA between daughters	> 0.8 cm	> 0.8 cm
V0 decay length	> 2.5 cm	> 3.0 cm
$(\vec{r}_{V0} - \vec{r}_{PV}) \cdot \vec{p}_{V0}$	> 0	> 0

the reconstructed parent particle and the line drawn from the generation vertex to the decay vertex. For V0 particle reconstruction, the pointing angle must be strictly positive, as established by the applied cut.

Even after applying all the cuts mentioned above, some background is still left in the invariant mass peak of K^0_s, Λ and $\overline{\Lambda}$. To estimate this background, the rotational method was used in which one daughter track was rotated by angle π in the transverse plane. The generated rotational background imitates the random combination contribution in K^0_s, Λ and $\overline{\Lambda}$ reconstruction. Figure 3.4 and Figure 3.5 show the invariant mass distribution of K^0_s and Λ, $\overline{\Lambda}$ after applying all the topological cuts discussed above.

3.2.1.1 Acceptance

The enhanced measurement capabilities of STAR after the iTPC upgrade are an important part of the BES-II program. The iTPC upgrade extends the rapidity coverage from $|\eta|<1$ to $|\eta|<1.5$ [40]. This provides a major benefit for extending the previous BES results from mid-rapidity ($|y|<0.5$) to higher rapidity ranges in case of strange and multi-strange hadrons production. Figure 3.6 shows the acceptance of strange V0 particles where p_T is plotted as a function of rapidity in Au+Au collisions at $\sqrt{s_{NN}} = 19.6$ GeV. The upgrade in iTPC enhances the measurement of the particles towards the high rapidity region. On the other hand, the high statistics in BES-II increases the high p_T reach of different particles.

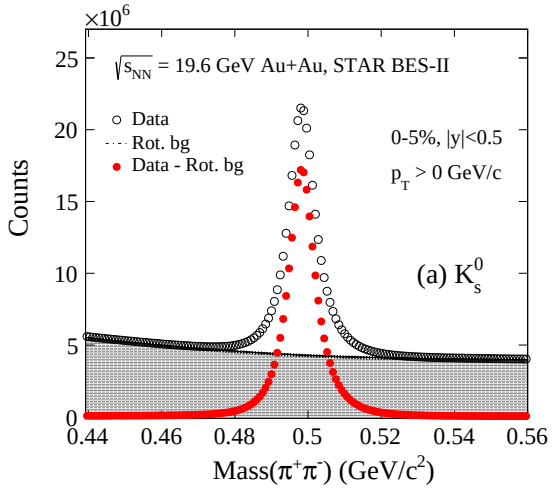

Figure 3.4: Invariant mass distribution for K^0_s with p_T>0 in the 0-5% centrality range at mid-rapidity (|y|<0.5) during Au+Au collisions at $\sqrt{s_{NN}}$ = 19.6 GeV. The combinatorial background has been estimated using the rotational method.

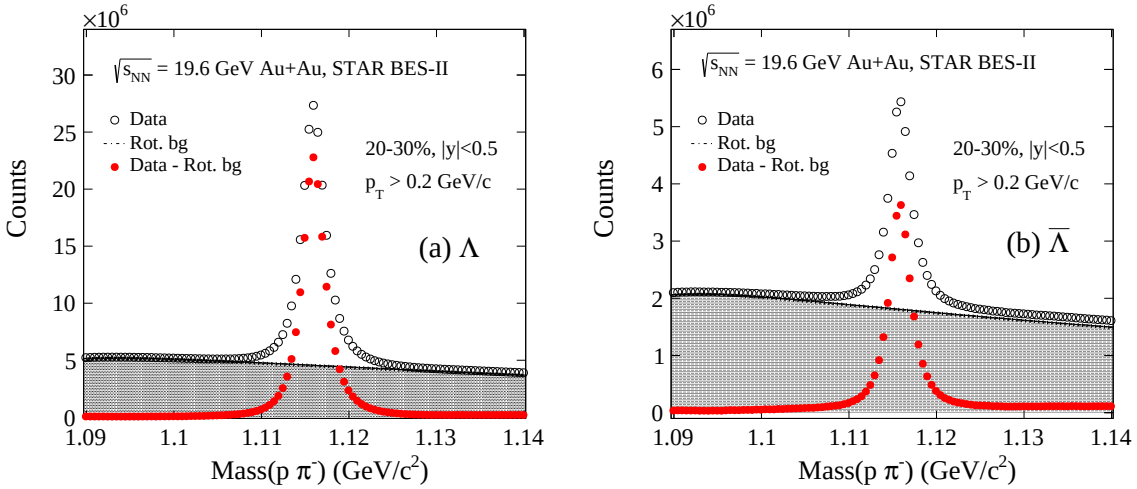

Figure 3.5: Invariant mass distributions for Λ and $\overline{\Lambda}$ at p_T>0.2 GeV/c within the 20-30% centrality and at mid-rapidity (|y|<0.5) in Au+Au collisions at $\sqrt{s_{NN}}$ = 19.6 GeV. The estimation of the combinatorial background was performed using the rotational method.

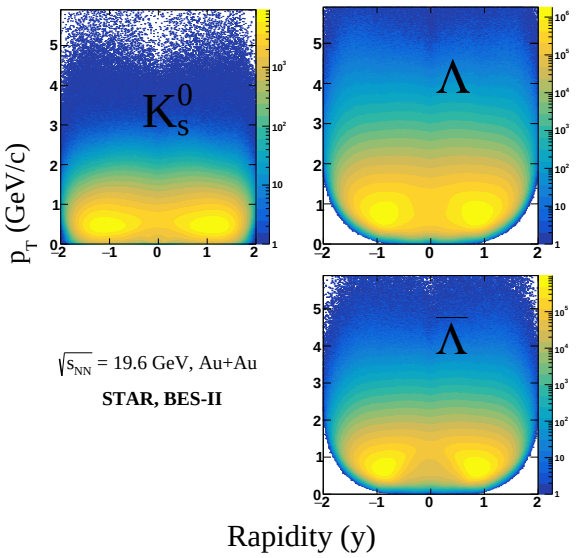

Figure 3.6: The phase space distribution of K^0_s, Λ and $\overline{\Lambda}$ in Au+Au collisions at $\sqrt{s_{NN}} = 19.6$ GeV.

3.2.1.2 Signal extraction

For signal extraction, the invariant mass distribution of strange V0 particles was subtracted from the corresponding rotational background. The resulting invariant mass distribution was fitted with a double Gaussian plus polynomial function defined by equation 3.2.

$$f(x) = a_0 + a_1 x + a_2 x^2 + \frac{Y_1}{\sqrt{2\pi}\sigma_1} exp(\frac{-(x-m_0)^2}{2\sigma_1^2}) + \frac{Y_2}{\sqrt{2\pi}\sigma_2} exp(\frac{-(x-m_0)^2}{2\sigma_2^2}) \quad (3.2)$$

where a_0, a_1, a_2 are coefficients of the polynomial terms, σ_1 and σ_2 are the standard deviations of the first and second Gaussian respectively, Y_1 and Y_2 are the amplitudes of the first and second Gaussian respectively, m_0 is the invariant mass of the particle. It determines the width of the signal peak as well as the shape of the remaining background in the distribution. The total counts inside the signal peak were then subtracted from that of the background inside the peak to obtain the total number of signal candidates. The background counts were estimated using the polynomial fit and subsequently subtracted from the total counts in the range 4σ to get signal counts. Due to limited statistics at high p_T region, the sideband method was used

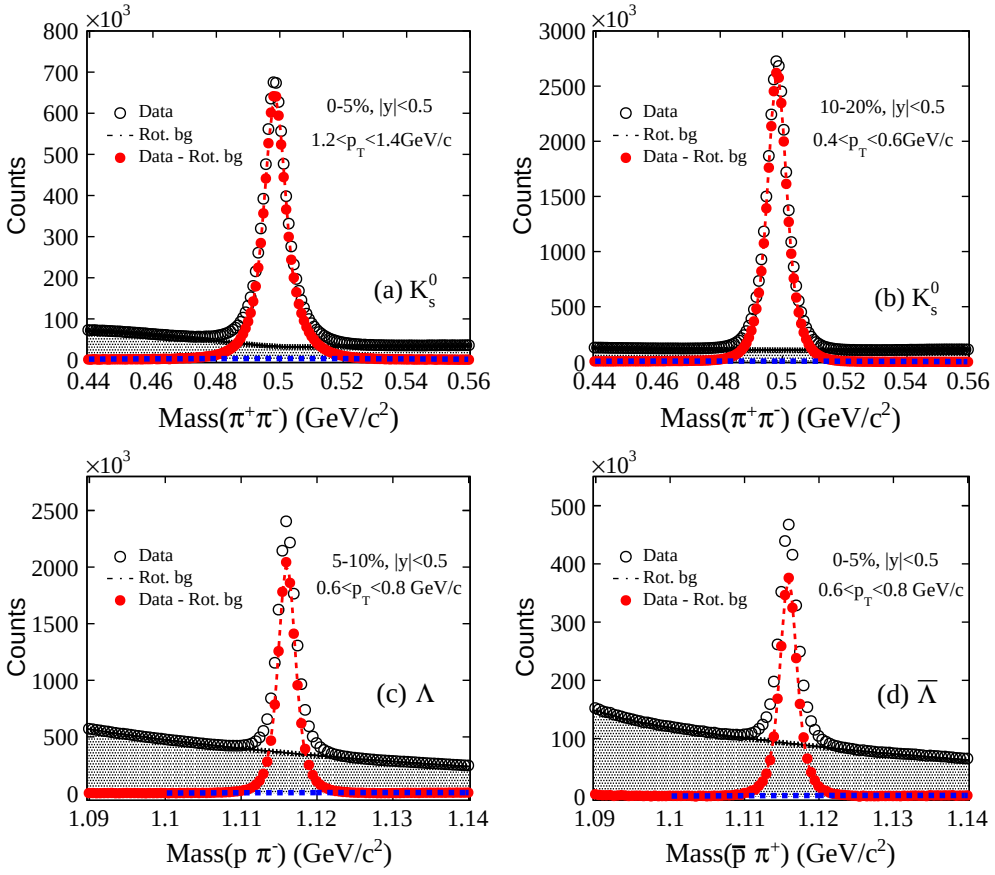

Figure 3.7: K^0_s, Λ and $\overline{\Lambda}$ invariant mass distributions in Au+Au collisions at $\sqrt{s_{NN}}$ = 19.6 GeV. The dashed lines represent the function fit results. The horizontal dashed lines are the fitted background contributions. The grey area shows the corresponding rotational background.

on either side of the signal peak. Figure 3.7 shows the invariant mass distribution of K^0_s, Λ, and $\overline{\Lambda}$ and the fitting results after the rotational background subtraction at different p_T bins (in GeV/c) in different centralities at mid-rapidity (|y|<0.5) in Au+Au collisions at $\sqrt{s_{NN}}$ = 19.6 GeV.

Figure 3.8 shows the invariant mass distribution of K^0_s as an example of the side band method in p_T bin [4.4-5.0] GeV/c in 20-30% centrality at mid-rapidity (|y|<0.5) in Au+Au collisions at $\sqrt{s_{NN}}$ = 19.6 GeV.

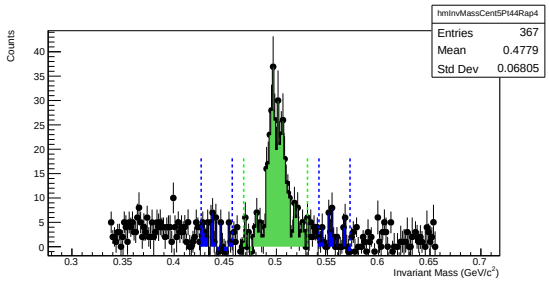

Figure 3.8: The invariant mass distribution of K^0_s within the transverse momentum bins of [4.4, 5.0] GeV/c for 20-30% centrality at mid-rapidity (|y|<0.5) in Au+Au collisions at $\sqrt{s_{NN}}$ = 19.6 GeV.

3.2.2 Strange V0 reconstruction using KFParticle Method

KFParticle is a C++ package developed for the reconstruction of short-lived strange baryons. It is based on the Kalman filter approximation [99]. The charged tracks detected in the experiment are given as input to the KFParticle. These charged tracks are classified into primary and secondary tracks, i.e., they identify whether the track comes from the primary vertex where the collision takes place or tracks come from the secondary vertex. It uses the χ^2 criterion for this purpose, which is given by

$$\chi^2 = \Delta\vec{r}^{\mathrm{T}}(C_{\mathrm{Track}} + C_{\mathrm{PV}})^{-1}\Delta\vec{r} \tag{3.3}$$

where $\Delta\vec{r}$ is the difference between the track and the primary vertex position and $\Delta\vec{r}^{\mathrm{T}}$ is the transpose of the distance vector, C_{Track} and C_{PV} are covariance matrices of the track and primary vertex, respectively. It was developed by the CBM experiment. Table 3.3 shows the selection criteria used for the $\Lambda(\bar{\Lambda})$ reconstruction. Figure 3.9 shows the invariant mass distribution of Λ and $\bar{\Lambda}$ in Au+Au collisions at $\sqrt{s_{NN}}$ = 19.6 GeV using the KFParticle package.

3.2.2.1 Uncorrected p_T spectra

After obtaining the signal candidates for each particle in each p_T and centrality bin, the raw spectra of the particles are obtained using the following equation 3.4

Table 3.3: Selection criteria used for the reconstruction of $\Lambda(\overline{\Lambda})$ in Au+Au collisions at $\sqrt{s_{NN}} = 19.6$ GeV in the KFParticle package.

Cuts on parameters	**Description**
$l > 5\,\text{cm}$	cut on a distance to PV
$l/dl > 5\,\text{cm}$	cut on a distance to PV normalised on the error
$\chi^2_{\text{geom}} < 10\,\text{cm}$	χ^2 of the track to the secondary track
$\chi^2_{\text{prim}} > 18.6\,\text{cm}$	cut on χ^2 of the track to PV
$\chi^2_{\text{topo}} < 5\,\text{cm}$	cut on χ^2 of the mother particle
$d_{\text{max}} < 1\,\text{cm}$	maximal separation between secondary tracks

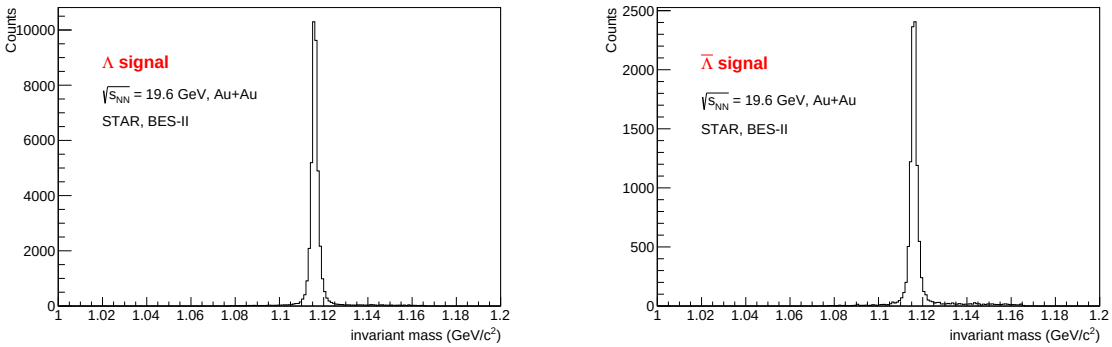

Figure 3.9: The invariant mass distribution of Λ and $\overline{\Lambda}$ at mid-rapidity (|y|<0.5) obtained using KFParticle Package in Au+Au collision at $\sqrt{s_{NN}} = 19.6$ GeV.

$$Y_{raw} = \frac{1}{N_{event}} \frac{N}{2\pi p_T \Delta p_T \Delta y\, br} \tag{3.4}$$

where N is the number of signal candidates, Y_{raw} is the raw yield in each centrality and p_T bin, N_{event} is the total number of events in the collisions, Δy is the rapidity bin width, p_T and Δp_T represent the center and width of the p_T bin, br is the branching ratio of the particles. Figure 3.10 shows the comparison of uncorrected spectra obtained for Λ and $\overline{\Lambda}$ for different centrality at mid-rapidity. We found that both methods give consistent results. The KFpaticle method is used for the measurement of global polarization of Λ and $\overline{\Lambda}$ hyperons in Au+Au collisions at $\sqrt{s_{NN}} = 19.6$ and 27 GeV [79][80]. The work discussed in this thesis is done using the Helix method. Figures 3.11 to 3.14 show the uncorrected p_T spectra of K^0_s, Λ, $\overline{\Lambda}$ in different rapidity bins in Au+Au collisions at $\sqrt{s_{NN}} = 19.6$ GeV using the Helix method.

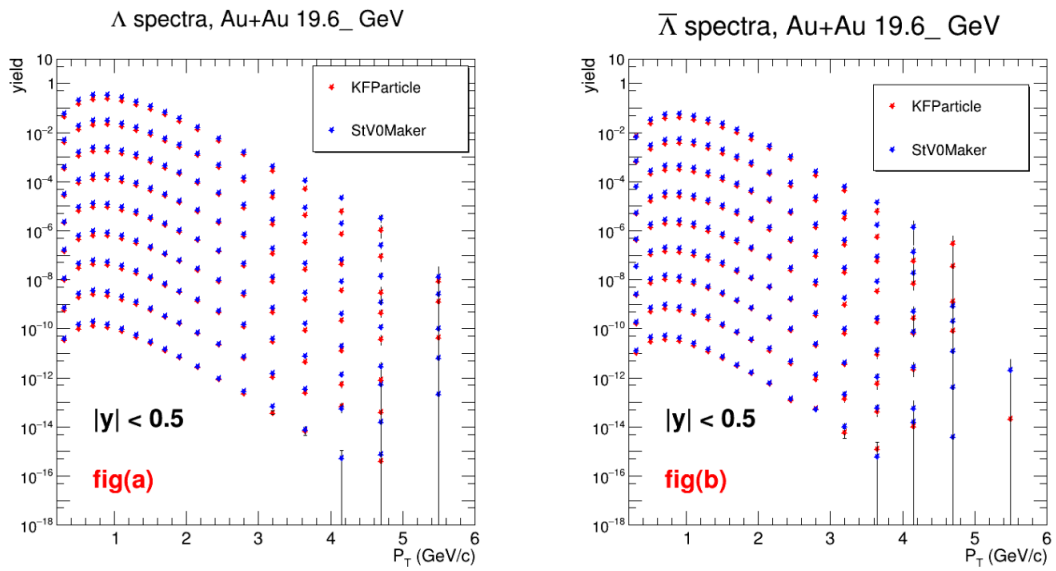

Figure 3.10: Comparison of uncorrected p_T spectra of Λ and ($\bar{\Lambda}$) for different centrality range at mid-rapidity (|y|<0.5) for Au+Au collisions at $\sqrt{s_{NN}}$ = 19.6 GeV from KFParticle and Helix method.

3.2.3 Multi-strange hyperons reconstruction

The multi-strange hyperons such as $\Xi^-(\overline{\Xi}^+)$, $\Omega^-(\overline{\Omega}^+)$ are reconstructed by finding the two decay vertices - one for the reconstruction of daughter $\Lambda(\overline{\Lambda})$ candidate and the other for the reconstruction of mother hyperon. The decay daughter $\Lambda(\overline{\Lambda})$ of strange hyperons further decays into charged particles $p^{\pm}$ and $\pi^{\pm}$ forming the V0 decay topology and can be reconstructed using the similar topological reconstruction process as described in section 3.2.1. Table 3.4 lists the properties and weak decay channels of the $\Xi^-(\overline{\Xi}^+)$, $\Omega^-(\overline{\Omega}^+)$ [95]. Figure 3.15 shows the decay topology of $\Xi^-(\overline{\Xi}^+)$, $\Omega^-(\overline{\Omega}^+)$ [96].

Table 3.4: Weak decay channel of $\Xi^-(\overline{\Xi}^+)$ and $\Omega^-(\overline{\Omega}^+)$ [95].

Particles	Weak decay channels	Branching Ratio	$c\tau$ (cm)
$\Xi^-(\overline{\Xi}^+)$	$\Lambda(\overline{\Lambda})\pi^-(\pi^+), \Lambda(\overline{\Lambda}) \rightarrow p(\overline{p}) + \pi^-(\pi^+)$	$99.887 \pm 0.035\%$	2.6942
$\Omega^-(\overline{\Omega}^+)$	$\Lambda(\overline{\Lambda})K^-(K^+), \Lambda(\overline{\Lambda}) \rightarrow p(\overline{p}) + \pi^-(\pi^+)$	$67.8 \pm 0.7\%$	2.461

The reconstructed $\Lambda(\overline{\Lambda})$ candidates can be combined with bachelor charged particle tracks, $\pi^{\pm}$ or $K^{\pm}$ to reconstruct the mother hyperons. This combination further

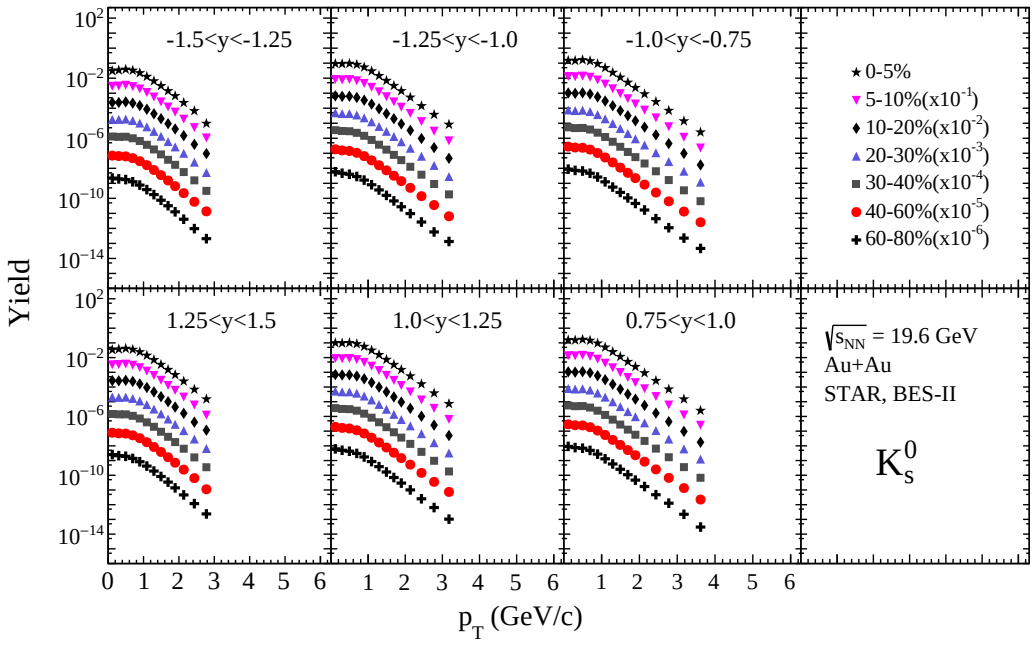

Figure 3.11: The uncorrected transverse momentum spectra of K_s^0 under the rapidity range [-1.5, -0.75] and [0.75, 1.5] in different collision centralities in Au+Au collisions at $\sqrt{s_{NN}} = 19.6$ GeV.

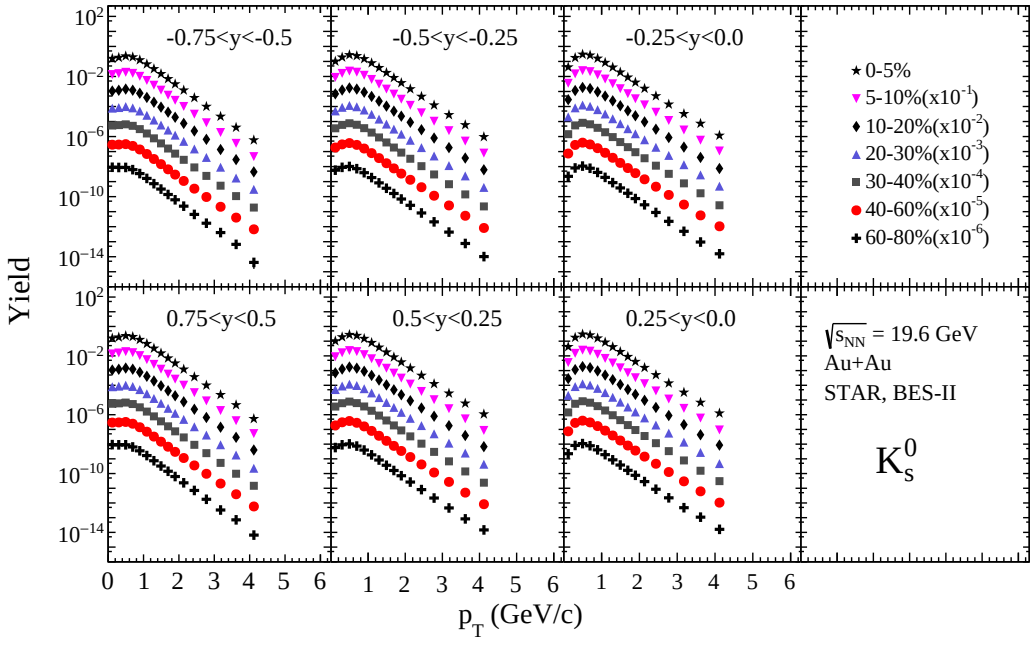

Figure 3.12: The uncorrected transverse momentum spectra of K_s^0 under the rapidity range [-0.75, 0.75] in different collision centralities in Au+Au collisions at $\sqrt{s_{NN}} = 19.6$ GeV.

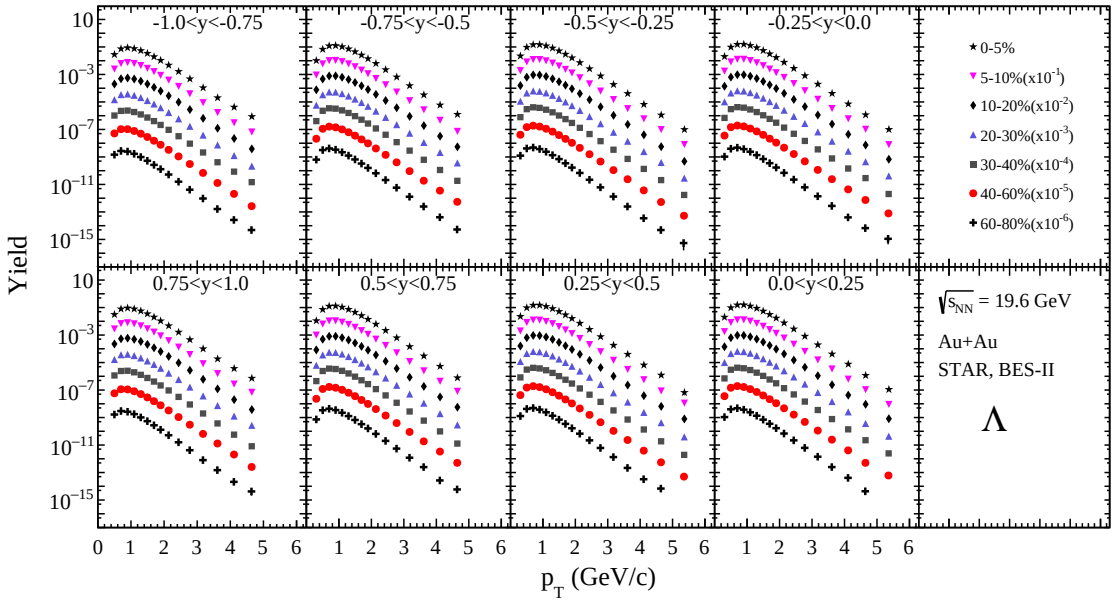

Figure 3.13: The uncorrected transverse momentum spectra of Λ under the rapidity range [-1,1] in different collision centralities in Au+Au collisions at $\sqrt{s_{NN}}$ = 19.6 GeV.

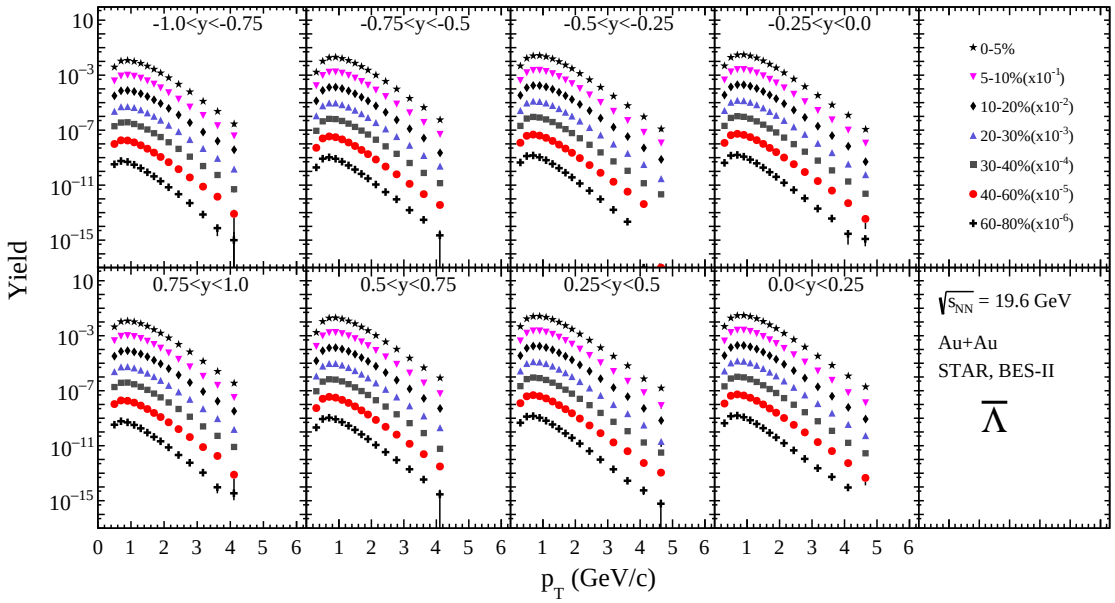

Figure 3.14: The uncorrected transverse momentum spectra of $\overline{\Lambda}$ under the rapidity range [-1,1] in different collision centralities in Au+Au collisions at $\sqrt{s_{NN}}$ = 19.6 GeV.

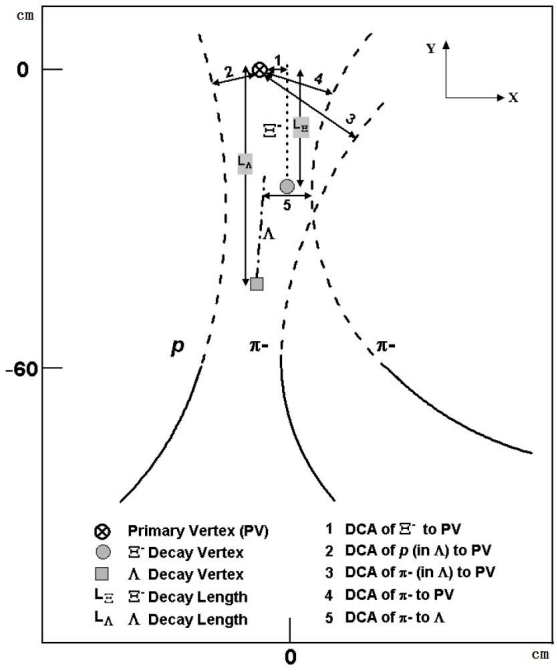

Figure 3.15: The Ξ^- decay topology with all the cuts shown in the plot. The decay topology of Ω^- is similar to Ξ^- where the bachelor particle is kaon. Figure is taken from [96].

requires a DCA cut between the $\Lambda(\overline{\Lambda})$ candidate and the bachelor charged particle track, $\pi^{\pm}$ or $K^{\pm}$. As the $\Lambda(\overline{\Lambda})$ candidate is produced at the decay vertex of the mother hyperon Ξ^- ($\overline{\Xi}^+$) or Ω^- ($\overline{\Omega}^+$), a threshold for DCA of $\Lambda(\overline{\Lambda})$ to the primary vertex is set to distinguish the decay $\Lambda(\overline{\Lambda})$ candidate from the primary $\Lambda(\overline{\Lambda})$ candidates. This helps to exclude the combinatorial background arising from primary $\Lambda(\overline{\Lambda})$ candidates in the invariant mass distribution of parent hyperons. Further, for the reconstruction of $\Xi^-(\overline{\Xi}^+)$ and $\Omega^-(\overline{\Omega}^+)$, cuts are also applied on decaylength of $\Lambda(\overline{\Lambda})$ candidates and mother hyperons, the DCA of $\Xi^-(\overline{\Xi}^+)$, $\Omega^-(\overline{\Omega}^+)$ to the primary vertex, DCA of bachelor $\pi^{\pm}$ or $K^{\pm}$ to the PV. These cuts greatly reduce the combinatorial background in the invariant mass distribution of mother hyperons. A cut of $|n\sigma_{par}|$<4.0 and Nhits>15 were used for all the corresponding charged particles except for Ω^- ($\overline{\Omega}^+$) where, to reduce the combinatorial background, a tighter cut of $|n\sigma_{par}|$<3.0 was applied. Table 3.5 shows the default cuts used for $\Xi^-(\overline{\Xi}^+)$ and $\Omega^-(\overline{\Omega}^+)$ reconstruction in this analysis.

The residual background arising due to particle misidentification was also considered for the reconstruction of multi-strange hyperons. A proton decaying from a real Λ may be combined with a random π^- to form Λ candidate and then combined with π^- daughter of real Λ to form a fake Ξ^- particle. Similarly, in Ω^- reconstruction, the bachelor π^- of a cascade can be misidentified as kaon. The residual background arising due to these particle misidentification can be removed by considering the veto cuts. For cascade reconstruction, the p daughter was combined with bachelor π to calculate the invariant mass distribution. If the calculated invariant mass falls inside the Λ invariant mass peak, the Ξ candidate was rejected.

The decay topology of $\Xi^-(\overline{\Xi}^+)$ and $\Omega^-(\overline{\Omega}^+)$ is very similar. As a result, the mis-identified $\Xi^-(\overline{\Xi}^+)$ significantly contributes in the background of $\Omega^-(\overline{\Omega}^+)$ due to their larger production cross-section. One way to exclude the mis-identified $\Xi^-(\overline{\Xi}^+)$ is to change the mass of kaon with π^- and reconstruct mis-identified $\Xi^-(\overline{\Xi}^+)$. If it falls in the invariant mass peak on Ξ, the Ω candidate was rejected.

Even after applying all the cuts mentioned above, some background is still left in the invariant mass peak of $\Xi^-(\overline{\Xi}^+)$ and $\Omega^-(\overline{\Omega}^+)$. To estimate this background, rotational method was used in which one daughter track was rotated by angle π in the transverse plane. The generated rotational background imitates the random combination contribution in $\Xi^-(\overline{\Xi}^+)$ and $\Omega^-(\overline{\Omega}^+)$ reconstruction. Figure 3.16 and Figure 3.17 show the invariant mass distribution of Ξ^-, $\overline{\Xi}^+$ and Ω^-, $\overline{\Omega}^+$ respectively, after applying all the topological cuts discussed above.

3.2.3.1 Acceptance

Figure 3.18 shows the acceptance of $\Xi^-(\overline{\Xi}^+)$, $\Omega^-(\overline{\Omega}^+)$ where p_T is plotted as a function of rapidity in Au+Au collisions at $\sqrt{s_{NN}} = 19.6$ GeV. The upgrade in iTPC enhances the measurement of the particles towards the high rapidity region. On the other hand, the high statistics in BES-II increases the high p_T reach of different particles.

Table 3.5: Topological selection criteria are applied for the reconstruction of $\Xi^-(\overline{\Xi}^+)$ and $\Omega^-(\overline{\Omega}^+)$. In this context, $\vec{r}_{Xi}$, $\vec{r}_{\Lambda}$, and $\vec{r}_{PV}$ refer to the decay vertex position vectors of $\Xi^-(\overline{\Xi}^+)$, $\Omega^-(\overline{\Omega}^+)$, and Λ, as well as the primary vertex position vector, respectively. The momentum vectors of $\Xi^-(\overline{\Xi}^+)$, $\Omega^-(\overline{\Omega}^+)$, and Λ are represented by $\vec{p}_{Xi}$ and $\vec{p}_{\Lambda}$, respectively

Cuts	Ξ^- and $\overline{\Xi}^+$ (cm)	Ω^- and $\overline{\Omega}^+$ (cm)
DCA of Xi to PV	< 0.8	< 0.4
DCA of bachelor π/K to PV	> 0.8	> 1.0
DCA of Λ to PV	[0.2,5.0]	> 0.4
DCA of proton to PV	> 0.5	> 0.6
DCA of π to PV	> 1.0	> 2.0
DCA between Λ and bachelor π/K	< 0.8	< 0.7
DCA between Λ daughters	< 0.8	< 0.7
Xi decay length	> 3.4	> 3.0
V0 decay length	> 5.0	> 4.0
$(\vec{r}_{\Lambda}$ - $\vec{r}_{PV}) \cdot \vec{p}_{\Lambda}$	> 0	> 0
$(\vec{r}_{\Lambda}$ - $\vec{r}_{Xi}) \cdot \vec{p}_{\Lambda}$	> 0	> 0
$(\vec{r}_{Xi}$ - $\vec{r}_{PV}) \cdot \vec{p}_{Xi}$	> 0	> 0
$(\vec{r}_{Xi}$ - $\vec{r}_{PV}) \times \vec{p}_{Xi}$ / $\mid \vec{r}_{Xi}$ - $\vec{r}_{PV} \mid$ / $\mid \vec{p}_{Xi}\mid$	< 0.2	< 0.12

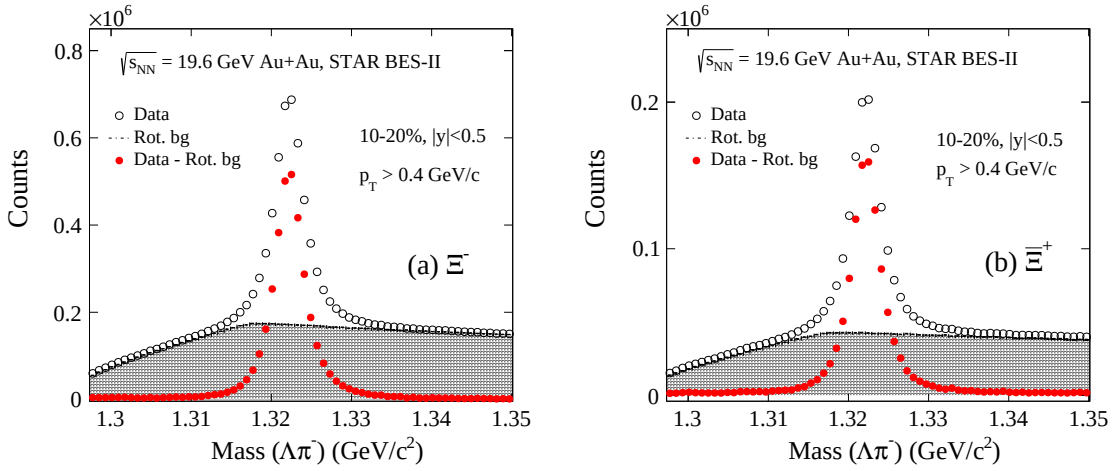

Figure 3.16: Invariant mass distributions for Ξ^- and $\overline{\Xi}^+$ at $p_T > 0.4$ GeV/c within the 10-20% centrality at mid-rapidity ($|y| < 0.5$) in Au+Au collisions at $\sqrt{s_{NN}} = 19.6$ GeV. The estimation of the combinatorial background was performed using the rotational method.

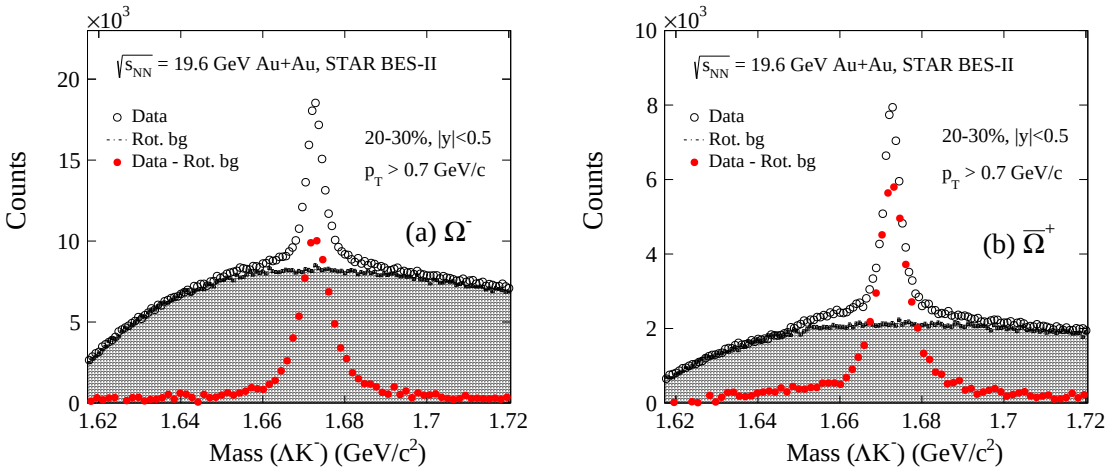

Figure 3.17: Invariant mass distributions for Ω^- and $\overline{\Omega}^+$ at $p_T > 0.7$ GeV/c within the 20-30% centrality at mid-rapidity ($|y| < 0.5$) in Au+Au collisions at $\sqrt{s_{NN}} =$ 19.6 GeV. The estimation of the combinatorial background was performed using the rotational method.

3.2.3.2 Signal extraction

The invariant mass distribution of multi-strange hyperons was subtracted from the corresponding rotational background for the signal extraction. The resulting invariant mass distribution was fitted with a double Gaussian plus polynomial function defined by equation 3.2. It specifies the width of the signal peak and the form of the background remaining in the distribution. The total counts inside the signal peak were then subtracted from that of the background inside the peak to obtain the total number of signal candidates. The background counts were estimated using the polynomial fit and subsequently subtracted from the total counts in the range 4σ to get signal counts. Due to limited statistics at high p_T region, the sideband method was used on either side of the signal peak.

Figure 3.19 shows the invariant mass distribution of Ξ^-, $\overline{\Xi}^+$, Ω^-, and $\overline{\Omega}^+$ and the fitting results after the rotational background subtraction at different p_T bins (in GeV/c) in different centralities at mid-rapidity (|y|<0.5) in Au+Au collisions at $\sqrt{s_{NN}} = 19.6$ GeV.

Figure 3.20 shows the invariant mass distribution of $\overline{\Xi}^+$ and Ω^- as an example

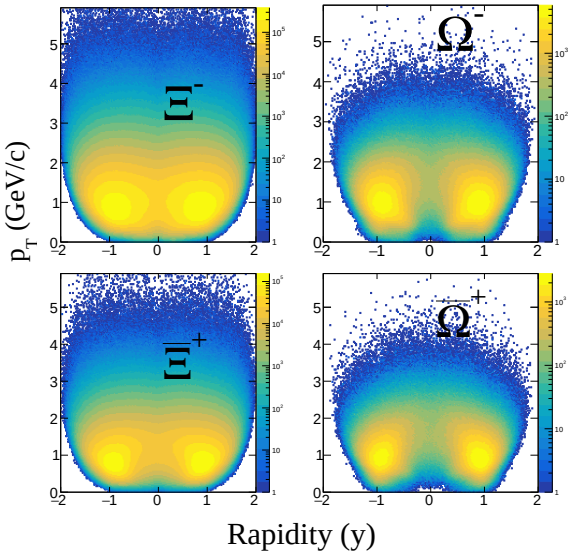

Figure 3.18: The phase space distribution of multi-strange hyperons $\Xi^-(\overline{\Xi}^+)$, $\Omega^-(\overline{\Omega}^+)$ in Au+Au collisions at $\sqrt{s_{NN}}$ = 19.6 GeV.

of the side band method in p_T bin [4.1-4.9] GeV/c in 0-5% centrality and [3.8,4.6] GeV/c in 0-10% centrality respectively at mid-rapidity (|y|<0.5) in Au+Au collisions at $\sqrt{s_{NN}}$ = 19.6 GeV.

3.2.3.3 Uncorrected p_T spectra

The uncorrected spectra of multi-strange hyperons are obtained using equation 3.4 under different centralities and p_T bins. The p_T spectra of Ξ^-, $\overline{\Xi}^+$ are obtained in the rapidity range [-1.0,1.0] with bin width Δy=0.25 and the p_T spectra of Ω^-, $\overline{\Omega}^+$ is obtained in the rapidity range [-0.9,0.9] with bin width Δy=0.3. Figures 3.21 to 3.24 show the uncorrected p_T spectra of Ξ^-, $\overline{\Xi}^+$, Ω^-, and $\overline{\Omega}^+$ in different rapidity bins in Au+Au collisions at $\sqrt{s_{NN}}$ = 19.6 GeV.

3.3 Efficiency correction

In experimental particle physics, not all the particles created in a collision are detected by the detectors. The detectors have finite efficiency in detecting and reconstructing particles. Therefore, in order to accurately determine the true production rates of

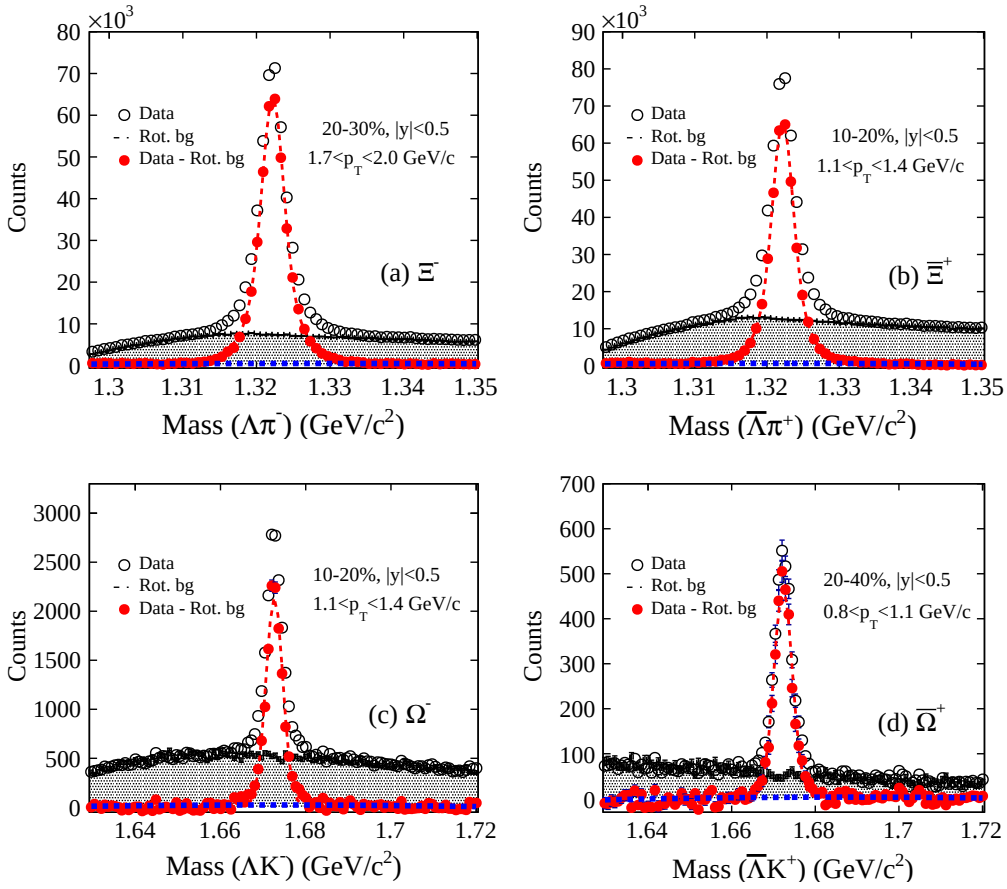

Figure 3.19: Ξ^-, $\overline{\Xi}^+$, Ω^-, and $\overline{\Omega}^+$ invariant mass distributions in Au+Au collisions at $\sqrt{s_{NN}}$ = 19.6 GeV. The dashed lines represent the function fit results (double Gaussian plus polynomial). The horizontal dashed lines are the fitted background contributions. The grey area shows the corresponding rotational background.

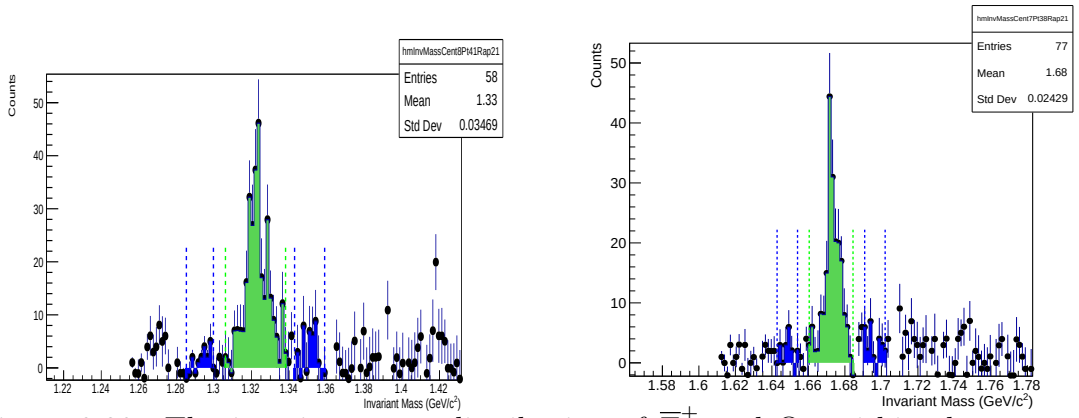

Figure 3.20: The invariant mass distribution of $\overline{\Xi}^{+}$ and Ω^{-} within the transverse momentum bins of [4.1, 4.9] GeV/c for 0-5% centrality and [3.8, 4.6] GeV/c for 0-10% centrality, respectively, at mid-rapidity (|y|<0.5) in Au+Au collisions at $\sqrt{s_{NN}}$ = 19.6 GeV.

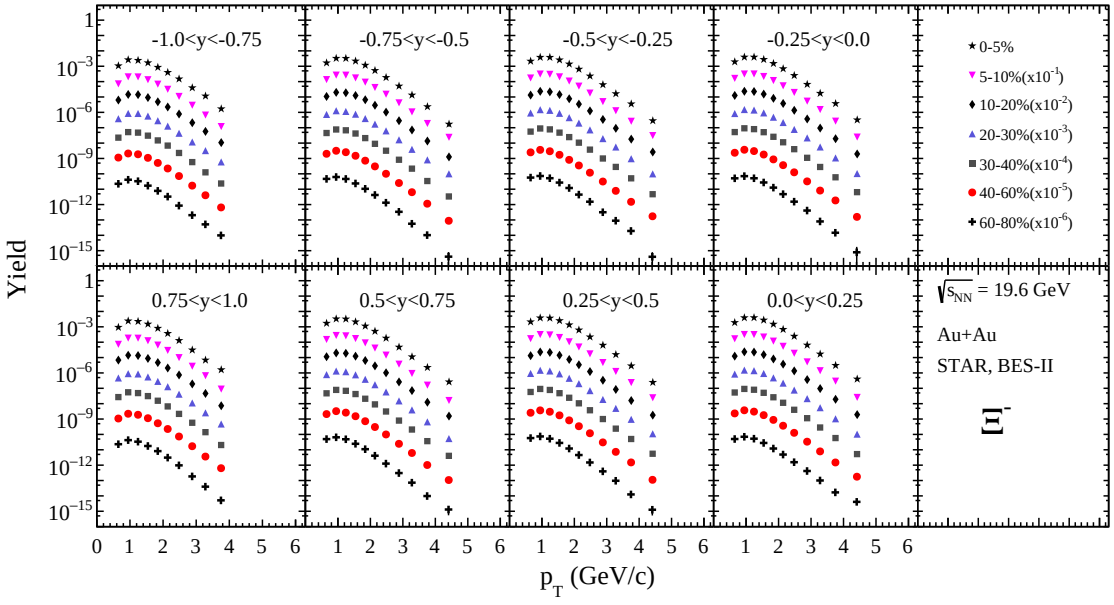

Figure 3.21: The uncorrected transverse momentum spectra of Ξ^{-} under the rapidity range [-1,1] in different collision centralities in Au+Au collisions at $\sqrt{s_{NN}}$ = 19.6 GeV.

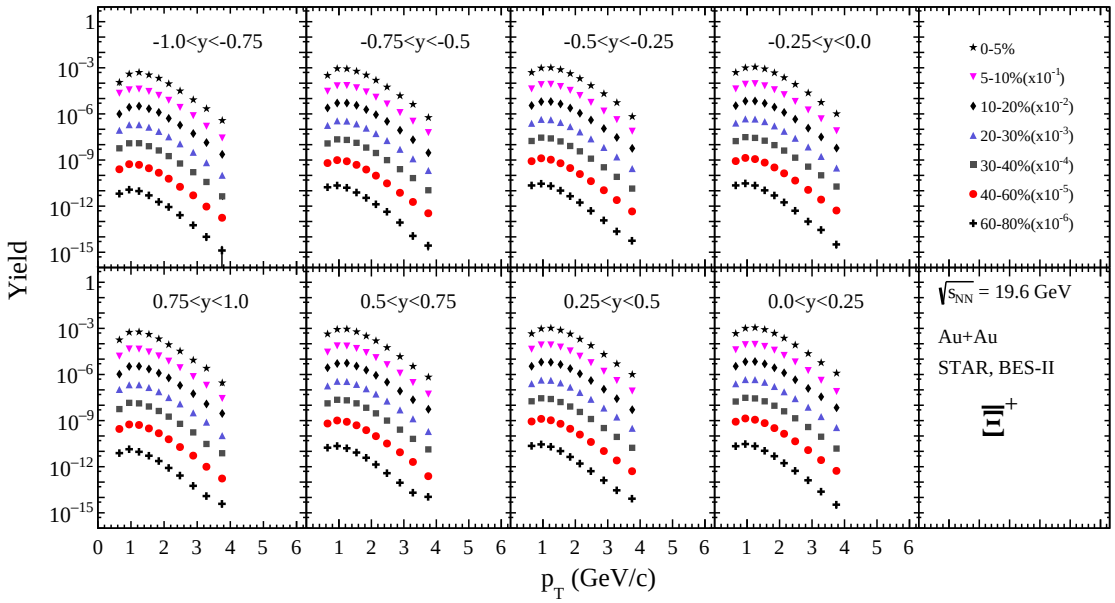

Figure 3.22: The uncorrected transverse momentum spectra of $\bar{\Xi}^{+}$ under the rapidity range [-1,1] in different collision centralities in Au+Au collisions at $\sqrt{s_{NN}}$ = 19.6 GeV.

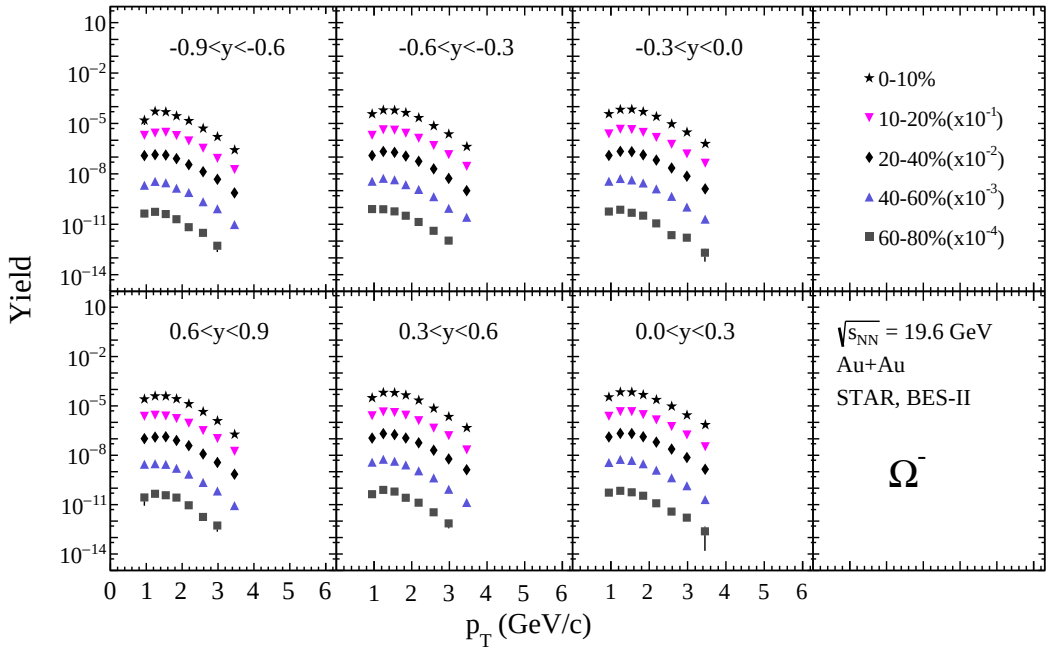

Figure 3.23: The uncorrected transverse momentum spectra of Ω^{-} under the rapidity range [-0.9,0.9] in different collision centralities in Au+Au collisions at $\sqrt{s_{NN}}$ = 19.6 GeV.

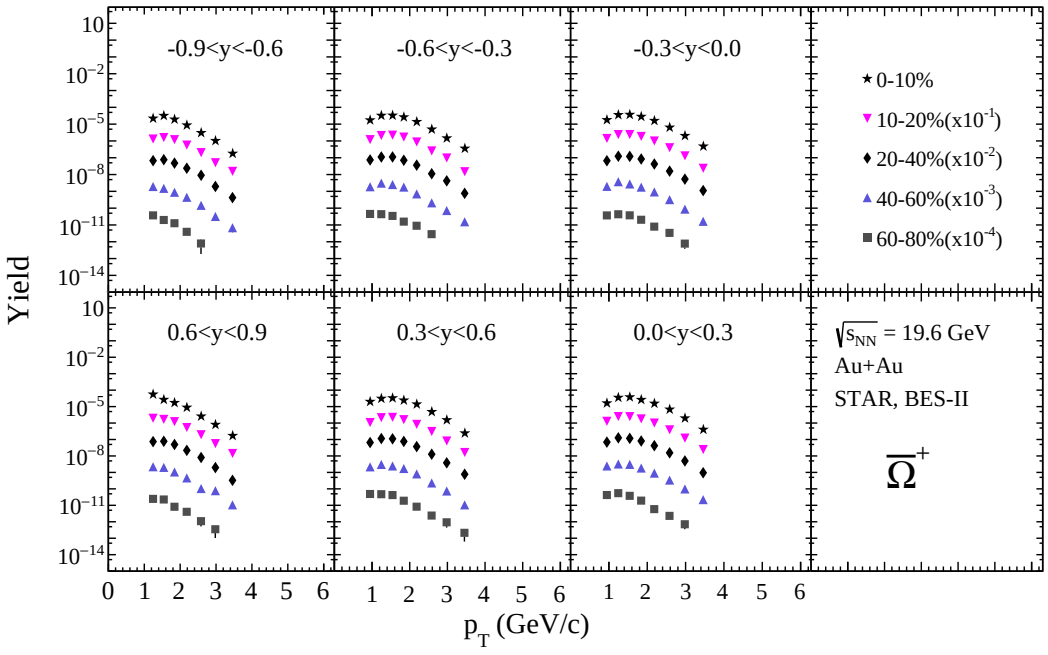

Figure 3.24: The uncorrected transverse momentum spectra of $\overline{\Omega}^{+}$ under the rapidity range [-0.9,0.9] in different collision centralities in Au+Au collisions at $\sqrt{s_{NN}}$ = 19.6 GeV.

particles in each collision, we need to correct the tracking efficiency for each particle.

To study the tracking efficiency, embedding data are used in the STAR experiment where simulated particles are embedded into real events and passed through the STAR detector environment simulated by the GEANT package [100]. The acceptance and reconstruction efficiency is calculated by dividing the number of reconstructed Monte Carlo (MC) strange hadrons by that of input MC ones. The same event and track selection cuts were applied to the embedding data as those used in data analysis. Figure 3.25 shows the acceptance × reconstruction efficiencies of strange and multistrange particles plotted against p_T (in GeV/c) in 0-5% central Au+Au collisions at mid-rapidity (|y|<0.5). It also shows a comparison of the reconstruction efficiencies with that of BES-I analysis [37]. From the figure, it is clear that the iTPC upgrade significantly improves the reconstruction efficiency towards the low p_T region.

Both flat and exponential p_T samples were used for the analysis. The reconstructed

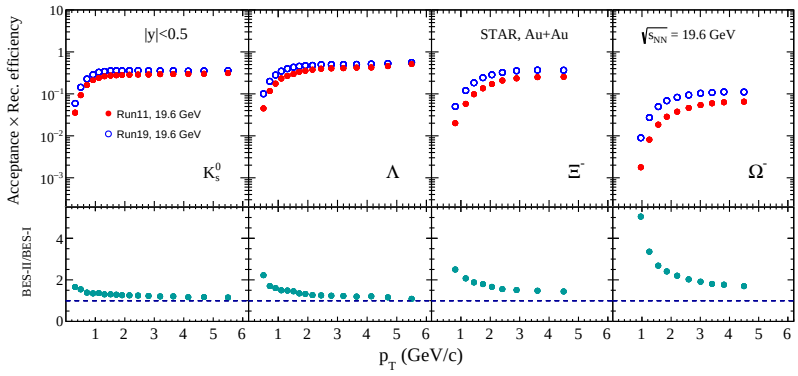

Figure 3.25: The acceptance × reconstruction efficiencies of K^0_s, Λ, Ξ^-, Ω^- at mid-rapidity (|y|<0.5) in 0-5% central Au+Au collisions at $\sqrt{s_{NN}}$ = 19.6 GeV. The open circles in each panel represent the acceptance × reconstruction efficiencies of particles from BES-II analysis, and the solid red circles represent the acceptance × reconstruction efficiencies of particles from BES-I analysis [37]. The lower panels of each plot provide a comparison between these two datasets. The selection cuts in BES-I and BES-II are the same.

efficiencies have lower statistics towards low p_T region and, therefore, show large statistical errors at that region. The exponential sample, $dN/dp_T \propto p_T \exp(-p_T/T)$, where T = 350 MeV, increases the statistics at lower p_T region significantly and therefore help in reducing the statistical fluctuation. In this analysis, the p_T binning used in efficiency calculation is the same as that in uncorrected spectra. Each MC particle was assigned a weight obtained from the fit to the corrected p_T spectra. The efficiencies at each p_T bin were calculated separately with flat p_T distribution and exponential p_T distribution. Figures 3.26 and 3.27 show the reconstruction efficiencies of K^0_s in the rapidity range [-1.5,1.5] in Au+Au collisions at $\sqrt{s_{NN}}$ = 19.6 GeV. For reconstruction efficiencies of Λ, $\overline{\Lambda}$, Ξ^-, $\overline{\Xi}^+$, Ω^-, and $\overline{\Omega}^+$ in different rapidity bins in Au+Au collisions at $\sqrt{s_{NN}}$ = 19.6 GeV, refer to Appendix A.

3.4 Estimation of Systematic Uncertainties

Systematic uncertainties in the measurement of strange hadron production were evaluated from various sources. For signal extraction, the range of the fitting function was changed. Following this, the impact of particle identification was examined by modifying the nσ cut values from 4.0 to 3.6, although this source of uncertainty is

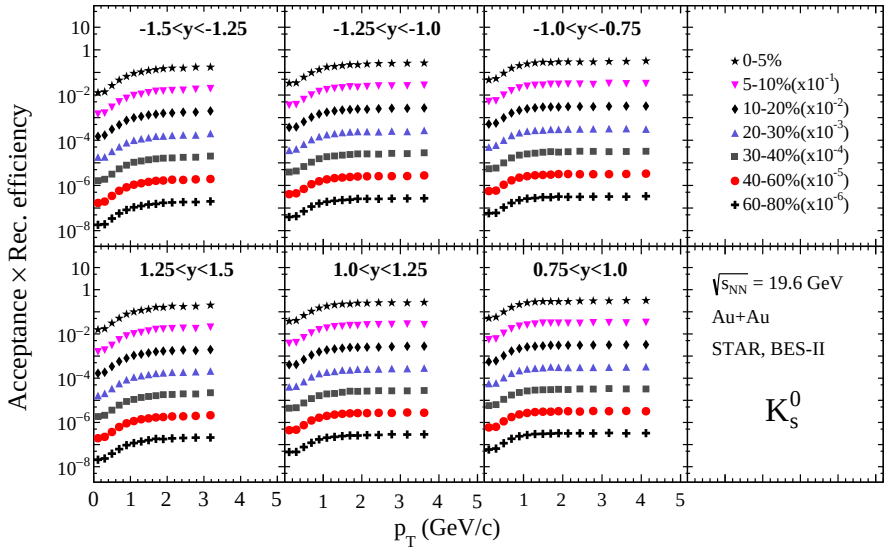

Figure 3.26: The acceptance × reconstruction efficiency of K_s^0 in Au+Au collisions at $\sqrt{s_{NN}}$ = 19.6 GeV in rapidity range [-1.5,-0.75] and [0.75,1.5].

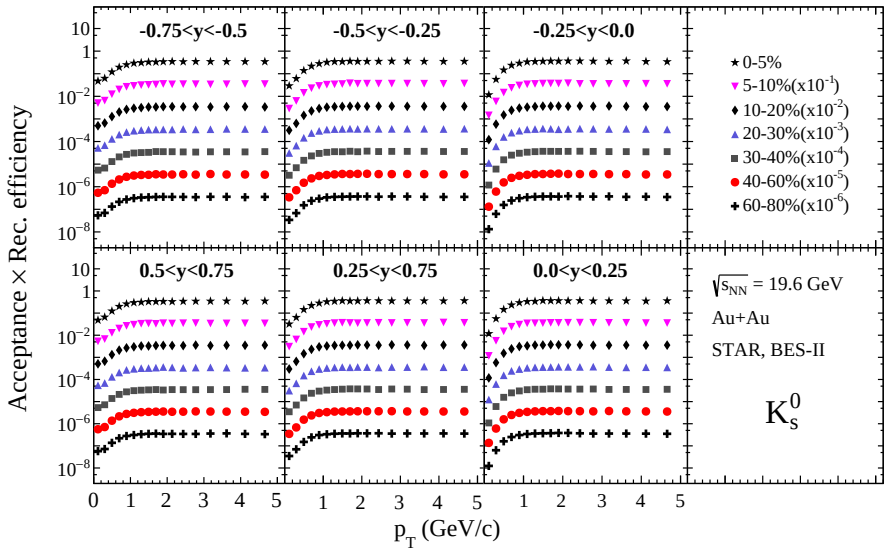

Figure 3.27: The acceptance × reconstruction efficiency of K_s^0 in Au+Au collisions at $\sqrt{s_{NN}}$ = 19.6 GeV in rapidity range [-0.75,0.75].

found to be minimal. Further, systematic errors related to tracking were investigated by varying the number of hits from 15 to 20, and the selection criteria for hit points used in the dE/dx calculations, which affects track reconstruction and, consequently, particle identification, was varied from 5 to 10.

The effect of varying the longitudinal vertex position (Vz) was considered from 145 cm to 125 cm, as changes in Vz can influence the acceptance and efficiency of detected particles. Finally, the systematic error analysis also includes a detailed review of topological cuts, altering each parameter sequentially to understand their effect on particle selection and background suppression. The systematic error due to these different topological variables was considered uncorrelated with one another and, therefore, added to the quadrature. The total systematic uncertainty for the p_T spectrum was determined by summing all individual sources quadratically, under the assumption that these sources are completely uncorrelated. Table 3.6 shows the variations in the topological reconstruction for K_s^0 and Λ ($\overline{\Lambda}$), and Table 3.7 details the variations in the topological reconstruction for Ξ^- ($\overline{\Xi}^+$) and Ω^- ($\overline{\Omega}^+$) in Au+Au collisions at $\sqrt{s_{NN}} = 19.6$ GeV. Figure 3.28 shows the percentage contribution arising from different sources for K_s^0 in the rapidity range [1.0,1.25] in Au+Au collisions at $\sqrt{s_{NN}} = 19.6$ GeV.

In the extrapolated low p_T region, systematic errors were calculated using different fitting functions. We fitted the default spectra of different particles with the blast-wave model [101] and the exponential function for this reason. The ultimate systematic errors in the extrapolation were derived as a quadratic sum of these two contributions.

It is difficult to estimate systematic variations due to various selection criteria when the number of reconstructed hadrons is small in given p_T and rapidity window. Therefore, to avoid overestimation of the errors, we used R. Barlow's method [102] to calculate the systematic uncertainty. This method makes a comparison of the estimated deviation with statistical fluctuations in the signal to avoid overestimation. Following steps are followed to assign systematic uncertainties when the number of

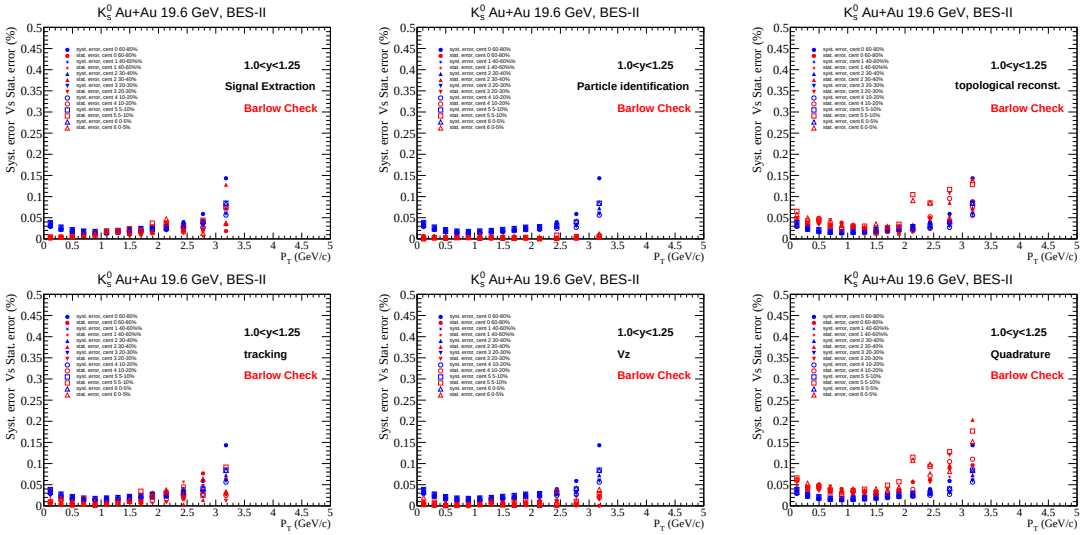

Figure 3.28: The figures show the percentage of the systematic errors plotted against the default statistical error for different systematic sources for K^0_s in the rapidity range [1.0, 1.25] in Au+Au collisions at $\sqrt{s_{NN}} = 19.6$ GeV.

reconstructed hadrons is small:

Step 1: $\Delta Y = |Y(i^{th}cut) - Y(def)|$

where Y(def) is the yield using default cuts and $Y(i^{th}cut)$ is a particular cut used for systematic analysis.

Step 2: $\Delta\sigma_{stat} = \sqrt{|\sigma^2_{stat}(i^{th}cut) - \sigma^2_{stat}(def)|}$

where $\sigma^2_{stat}(i^{th}cut)$ and $\sigma^2_{stat}(def)$ are the statistical uncertainty in the i^{th} cut and default cut respectively.

Step 3: if $(\Delta Y < \Delta\sigma_{stat})$, $\sigma_{sys}(i^{th}cut) = \Delta Y$

Step 4: if $(\Delta Y > \Delta\sigma_{stat})$, $\sigma_{sys}(i^{th}cut) = \sqrt{(\Delta Y)^2 - (\Delta\sigma_{stat})^2}$

3.5 Feed-down correction for Λ

Although a tight cut on the DCA of Λ candidates to the primary vertex is used to diminish the secondary Λ contributions from multistrange hyperons such as Ξ and Ξ^0, yet a fraction of the secondary Λ passes this criterion and reconstructed as a primary Λ candidate. The primary Λ candidates produced in the collisions

Table 3.6: Default cuts and their variations for K^0_s and Λ ($\overline{\Lambda}$).

Cuts	K^0_s		Λ ($\overline{\Lambda}$)	
	default cuts	variations	default cuts	variations
DCA of V0 to PV	< 0.8 cm	0.6-1.2 cm	< 0.8 cm	0.6-1.0 cm
DCA of daughters to PV	> 0.7 cm	0.6-0.8 cm	> 0.3 cm (proton)	0.3-0.45 cm (proton)
			> 1.0 cm (π)	1.0-2.0 cm (π)
DCA between daughters	> 0.8 cm	0.6-1.0 cm	> 0.8 cm	0.6-1.0 cm
V0 decay length	> 2.5 cm	2.5-3.3 cm	> 3.0 cm	3.0-4.5 cm

Table 3.7: Default cuts and their variations for Ξ^- ($\overline{\Xi}^+$) and Ω^- ($\overline{\Omega}^+$).

Cuts	Ξ^- ($\overline{\Xi}^+$)		Ω^- ($\overline{\Omega}^+$)	
	default cuts	variations	default cuts	variations
Xi decay length	> 3.4 cm	3.1-3.7 cm	> 3.0 cm	2.5-3.4 cm
V0 decay length	> 5.0 cm	4.8-5.5 cm	> 5.0 cm	4.0-6.0 cm
DCA of Xi to PV	< 0.8 cm	0.7-0.9 cm	< 0.4 cm	0.35-0.45 cm
DCA of bachelor π/K to PV	> 0.8 cm	0.6-1.0 cm	> 1.0 cm	0.9-1.1 cm
DCA of Λ to PV	> 0.2 cm	0.2-0.4 cm	> 0.4 cm	0.35-0.45 cm
DCA of Λ daughter p to PV	< 0.5 cm	0.4-0.6 cm	< 0.6 cm	0.5-0.70 cm
DCA of Λ daughter π to PV	< 1 cm	1.0-1.2 cm	< 2.0 cm	1.8-2.2 cm
DCA between Λ and bachelor π/K	< 0.8 cm	0.7-0.9 cm	< 0.7 cm	0.6-0.8 cm
DCA between Λ-daughters	< 0.8 cm	0.7-0.9 cm	< 0.7 cm	0.6-0.8 cm

help in understanding the production mechanisms and dynamics of Λ hyperons in the collisions. Therefore, the contribution from secondary Λ candidates needs to be removed. The contribution from secondary Λ candidates was assessed using Ξ and Ξ^0 Monte Carlo (MC) embedding data. Prompt Λ selection criteria were applied to reconstruct secondary MC Λ particles from the decay of MC Ξ and Ξ^0. The resulting number of these secondary MC Λ particles was subsequently scaled according to the corrected yields of the experimentally measured Ξ and Ξ^0 particles. Those scaled values represent the feed-down contribution and are deducted from the raw Λ yields [37]. The feed-down contribution to the uncorrected signal counts in the i-th p_T bin can be written as

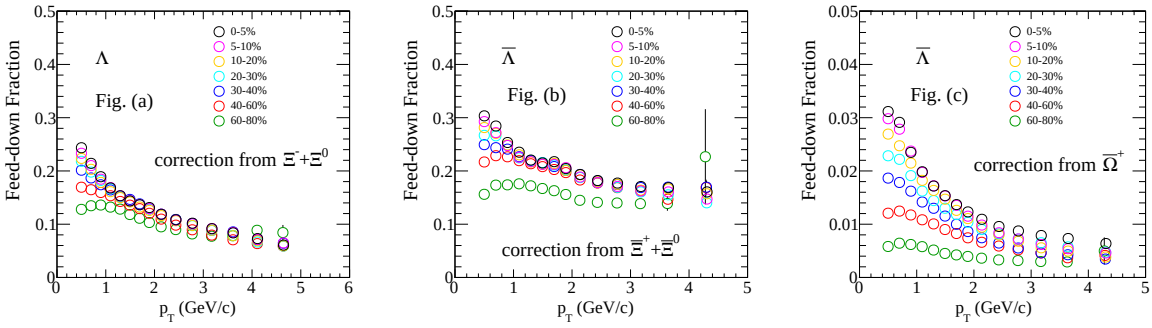

Figure 3.29: Fig. (a) shows the feed-down fraction for Λ. The plot shows the corrections applied due to the contributions from both Ξ^- and Ξ^0 particles. Fig. (b) shows feed-down fractions for $\overline{\Lambda}$. The plot shows the corrections applied due to the contributions from both $\overline{\Xi}^+$, $\overline{\Xi}^0$ particles. Fig. (c) shows feed-down fractions for $\overline{\Lambda}$. The plot shows the corrections applied due to the contributions from both $\overline{\Omega}^+$.

$$N^i_{\Lambda,FD} = N_{events}\left(\frac{N^i_{\Lambda\leftarrow\Xi}}{N_\Xi}\left.\frac{dN}{dy}\right|_\Xi \Delta y Br(\Xi\rightarrow\Lambda\pi) + \frac{N^i_{\Lambda\leftarrow\Xi^0}}{N_{\Xi^0}}\left.\frac{dN}{dy}\right|_{\Xi^0}\Delta y Br(\Xi^0\rightarrow\Lambda\pi)\right) \tag{3.5}$$

where Br are the corresponding branching ratios, Δy is the width of rapidity, dN/dy is the particle yield obtained from the integral of p_T spectra of Ξ or Ξ^0. For the Ξ^0, we assumed that its yield is the same as that of Ξ, as it cannot be directly measured by STAR. Consequently, a separate Ξ^0 embedding sample was produced for the Λ feed-down study. Given that the lifetime of Ξ^0 is significantly longer than that of Ξ, the distributions of the topological variables are also markedly different. Figure 3.29 shows the feed-down fractions for Λ and $\overline{\Lambda}$ at mid-rapidity (|y|<0.5) in Au+Au collisions at $\sqrt{s_{NN}}$ = 19.6 GeV. For $\overline{\Lambda}$, feed-down corrections from $\overline{\Omega}^+$, have also been considered.

3.6 Corrected p_T spectra

The efficiency-corrected transverse momentum spectra of strange and multi-strange particles refer to the distribution of efficiency-corrected yields of particles as a function of p_T in different collision centralities under a certain rapidity window. The transverse momentum spectra are important for studying the production mechanism

and properties of the particles.

Figures 3.30, 3.31, and 3.32 show the corrected transverse momentum spectra of K^0_s, $\Lambda(\overline{\Lambda})$, and $\Xi^-(\overline{\Xi}^+)$ respectively at mid-rapidity (|y|<0.5) and the comparison with that of the previous BES analysis. The p_T spectra of strange particles from previous BES analysis and current BES analysis at mid-rapidity (|y|<0.5) exhibit a good agreement between the two analyses. Figure 3.33 to 3.40 represent the corrected transverse momentum spectra of K^0_s, Λ, $\overline{\Lambda}$, Ξ^-, $\overline{\Xi}^+$, Ω^-, $\overline{\Omega}^+$ at different rapidity bins in Au+Au collisions at $\sqrt{s_{NN}}$ = 19.6 GeV.

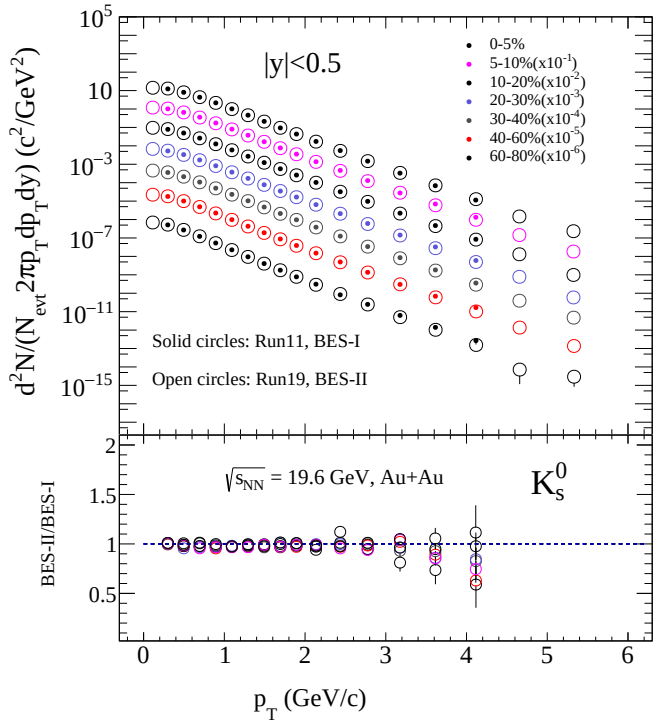

Figure 3.30: The corrected transverse momentum spectra of K^0_s at mid-rapidity (|y|<0.5) in Au+Au collisions at $\sqrt{s_{NN}}$ = 19.6 GeV. The open circles represent K^0_s corrected transverse momentum spectra from BES-II analysis, and the solid circles represent the corrected transverse momentum spectra from BES-I analysis. The lower panel provides a comparison between these two datasets.

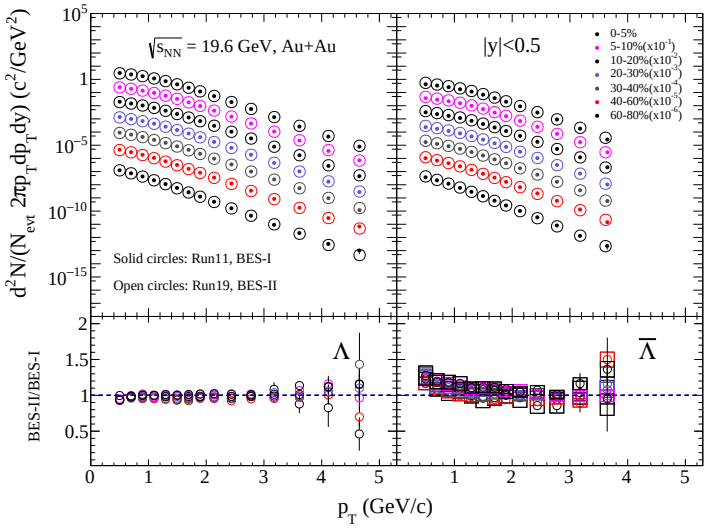

Figure 3.31: The corrected transverse momentum spectra of Λ and $\overline{\Lambda}$ at mid-rapidity (|y|<0.5) in Au+Au collisions at $\sqrt{s_{NN}}$ = 19.6 GeV. The open circles in both the panels represent Λ and $\overline{\Lambda}$ corrected transverse momentum spectra from BES-II analysis, and the solid circles represent the corrected transverse momentum spectra from BES-I analysis. The lower panels provide a comparison between these two datasets. The square boxes in case of $\overline{\Lambda}$ show systematic errors.

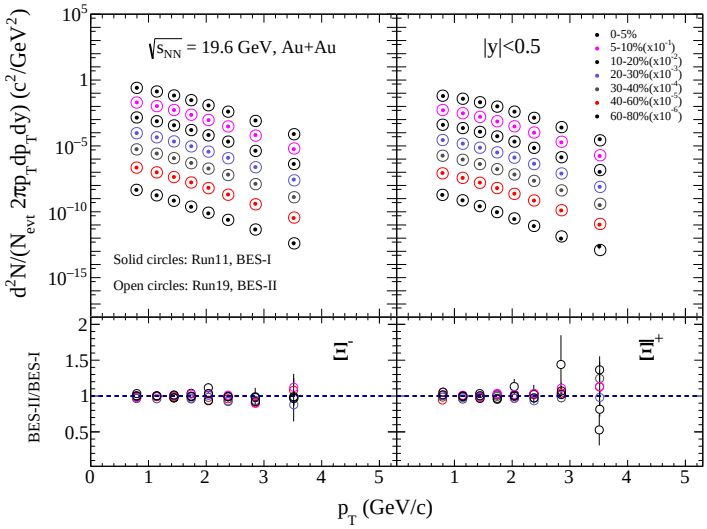

Figure 3.32: The corrected transverse momentum spectra of Ξ^- and $\overline{\Xi}^+$ at mid-rapidity (|y|<0.5) in Au+Au collisions at $\sqrt{s_{NN}}$ = 19.6 GeV. The open circles in both the panels represent Ξ^- and $\overline{\Xi}^+$ corrected transverse momentum spectra from BES-II analysis and the solid circles represent the corrected transverse momentum spectra from BES-I analysis. The lower panels provide a comparison between these two datasets.

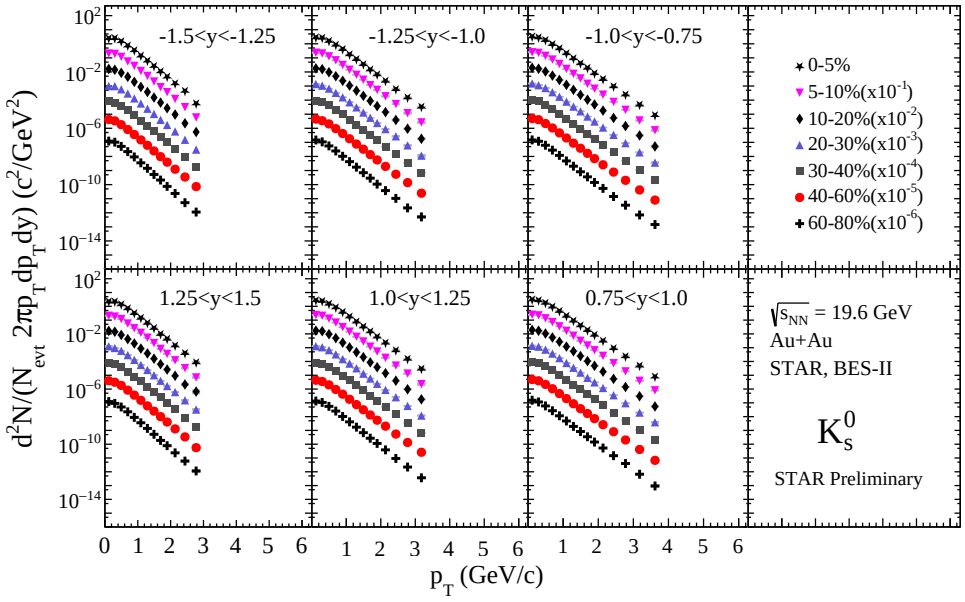

Figure 3.33: The corrected transverse momentum spectra of K_s^0 in rapidity range [-1.5,-0.75] and [0.75,1.5] in Au+Au collisions at $\sqrt{s_{NN}} = 19.6$ GeV. The vertical bars represent the statistical error, and the vertical bands represent the systematic errors.

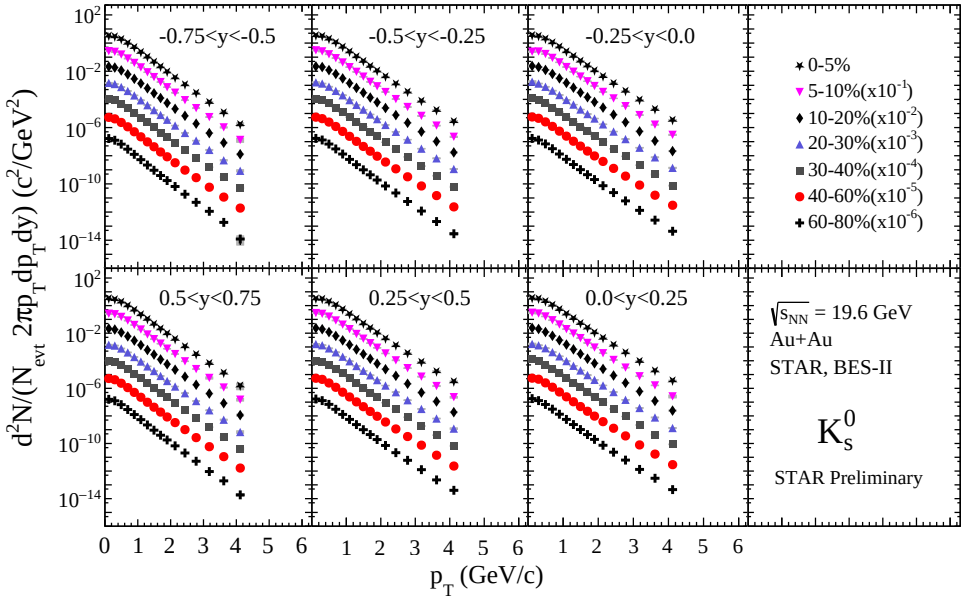

Figure 3.34: The corrected transverse momentum spectra of K_s^0 in rapidity range [-0.75,0.75] in Au+Au collisions at $\sqrt{s_{NN}} = 19.6$ GeV. The vertical bars represent the statistical error, and the vertical bands represent the systematic errors.

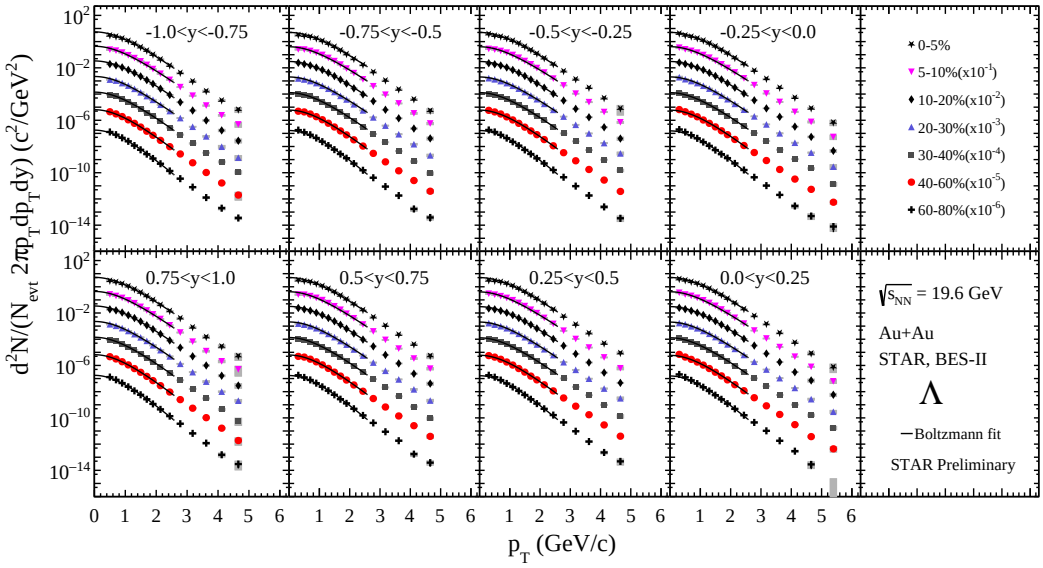

Figure 3.35: The corrected transverse momentum spectra of Λ in rapidity range [-1,1] in Au+Au collisions at $\sqrt{s_{NN}} = 19.6$ GeV. The vertical bars represent the statistical error, and the vertical bands represent the systematic errors.

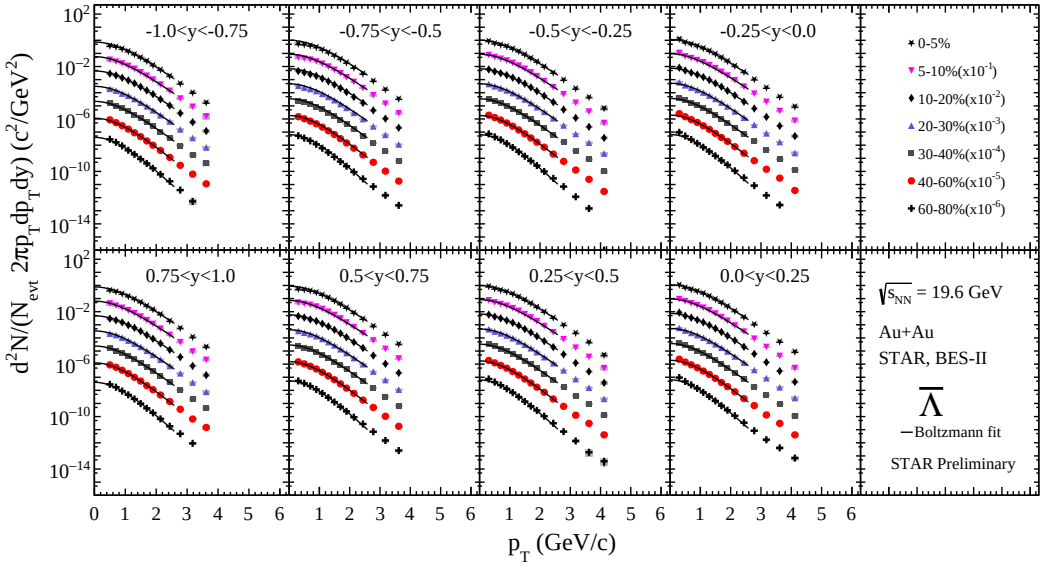

Figure 3.36: The corrected transverse momentum spectra of $\overline{\Lambda}$ in rapidity range [-1,1] in Au+Au collisions at $\sqrt{s_{NN}} = 19.6$ GeV. The vertical bars represent the statistical error, and the vertical bands represent the systematic errors.

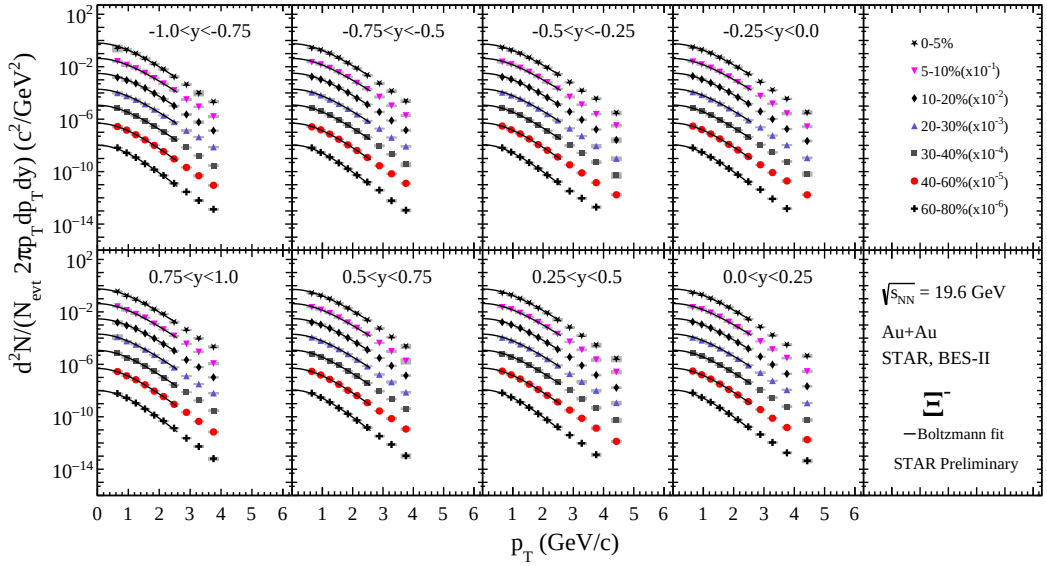

Figure 3.37: The corrected transverse momentum spectra of Ξ^- in rapidity range [-1,1] in Au+Au collisions at $\sqrt{s_{NN}}$ = 19.6 GeV. The vertical bars represent the statistical error, and the vertical bands represent the systematic errors.

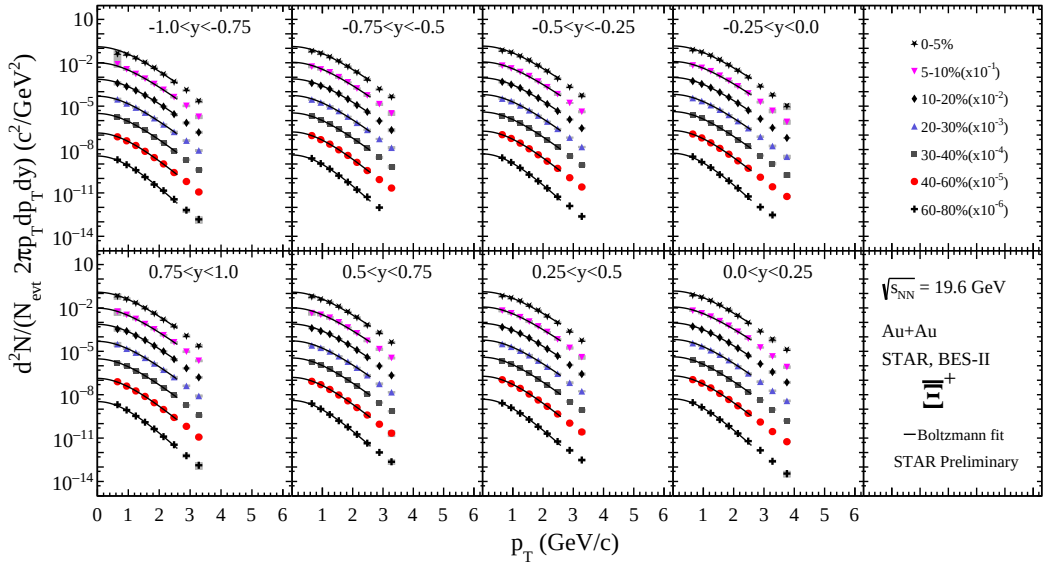

Figure 3.38: The corrected transverse momentum spectra of $\bar{\Xi}^+$ in rapidity range [-1,1] in Au+Au collisions at $\sqrt{s_{NN}}$ = 19.6 GeV. The vertical bars represent the statistical error, and the vertical bands represent the systematic errors.

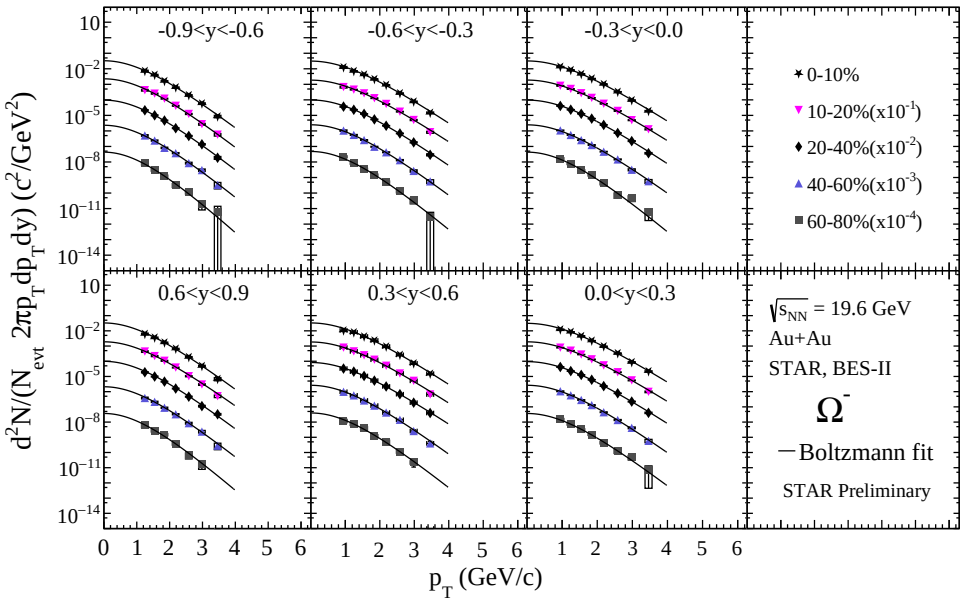

Figure 3.39: The corrected transverse momentum spectra of Ω^- in rapidity range [-0.9,0.9] in Au+Au collisions at $\sqrt{s_{NN}}$ = 19.6 GeV. The vertical bars represent the statistical error, and the vertical bands represent the systematic errors.

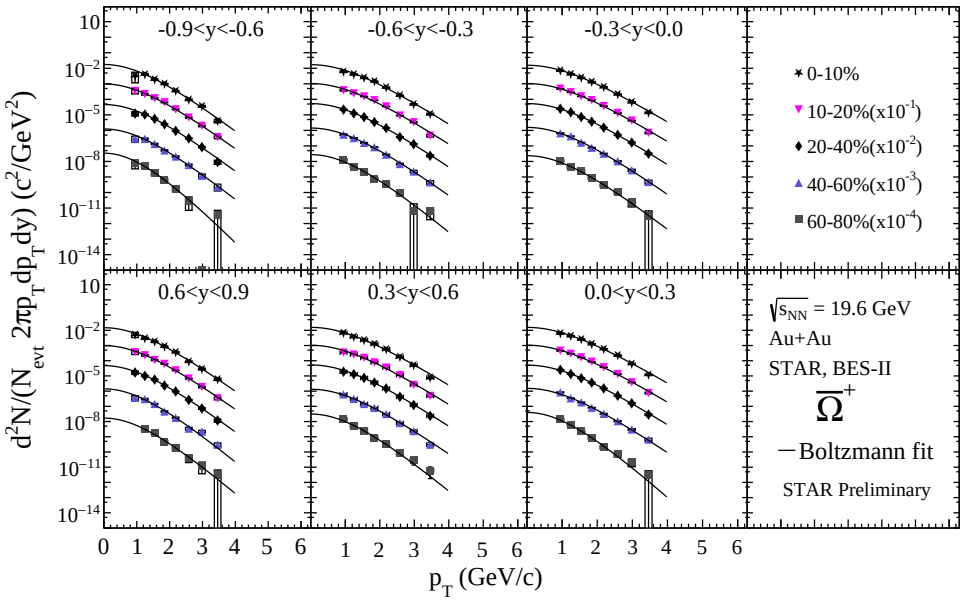

Figure 3.40: The corrected transverse momentum spectra of $\overline{\Omega}^+$ in rapidity range [-0.9,0.9] in Au+Au collisions at $\sqrt{s_{NN}}$ = 19.6 GeV. The vertical bars represent the statistical error, and the vertical bands represent the systematic errors.

Chapter 4

Results and discussions

In high-energy heavy-ion collisions, the study of strange and multi-strange particle production provides crucial insights into the properties of the QGP and the dynamics of the collision environment. Rapidity spectra, nuclear modification factor (R_{cp}), and baryon-to-meson ratios are one of the key observables that help in understanding the interplay between partonic and hadronic phases of matter. In this chapter, we will discuss the rapidity spectra, nuclear modification factor, and baryon-to-meson ratios of strange and multi-strange particles.

4.1 Rapidity spectra

Due to the detector acceptance, it is difficult to reconstruct strange baryons in the low p_T region. The extrapolation to the unmeasured region in the transverse momentum (p_T) spectra of strange and multi-strange particles was performed in order to obtain the p_T integrated yield ($\frac{dN}{dy}$) of the particles. The extrapolation at low p_T is crucial as it makes a significant contribution to the $\frac{dN}{dy}$ measurement, whereas the high p_T extrapolation contributes much less. The low p_T extrapolation to strange and multi-strange particles was done using the Boltzmann function of the form

$$\frac{d^2N}{2\pi p_T dp_T dy} \propto m_T e^{-\frac{m_T}{T}} \tag{4.1}$$

where $m_T = \sqrt{m^2 + p_T^2}$ denotes the transverse mass of the particles, dy is the

change in rapidity, T represents the temperature, p_T is the transverse momentum, and dp_T signifies the change in transverse momentum.

The integrated yield ($\frac{dN}{dy}$) obtained from the p_T spectra of particles and antiparticles was plotted as a function of rapidity (y) for different centrality ranges to obtain the rapidity spectra of strange hadrons. Figure 4.1 shows the rapidity spectra of K^0_s, Λ, $\overline{\Lambda}$, Ξ^-, $\overline{\Xi}^+$, Ω^-, and $\overline{\Omega}^+$ in Au+Au collisions at $\sqrt{s_{NN}} = 19.6$ GeV. For K^0_s, the rapidity spectra were calculated in the range [-1.5, 1.5] with a rapidity bin width $\Delta y = 0.25$. For Λ, $\overline{\Lambda}$, Ξ^-, and $\overline{\Xi}^+$, the rapidity spectra were calculated in the range $[-1.0, 1.0]$ with a bin width $\Delta y = 0.25$. For Ω^- and $\overline{\Omega}^+$, the rapidity spectra were calculated in the range $[-0.9, 0.9]$ with a bin width $\Delta y = 0.3$.

For K^0_s, the lowest p_T is ~ 0, hence extrapolation was not needed at low p_T. For Λ and $\overline{\Lambda}$ unmeasured p_T region (< 0.2 GeV/c), the Boltzmann function was fitted in the range [0.2,3.2] GeV/c for all the centralities. For Ξ^- and $\overline{\Xi}^+$ unmeasured p_T region (< 0.5 GeV/c), the Boltzmann function was fitted in the range [0.5,2.6] GeV/c. For Ω^- and $\overline{\Omega}^+$ unmeasured p_T region, Boltzmann function was fitted in the range [0.8,4.2] GeV/c. The blast-wave model [101] of the form

$$\frac{d^2N}{2\pi p_T dp_T dy} \propto \int_0^R r dr m_T I\left(\frac{p_T sinh\rho(r)}{T}\right) \times K\left(\frac{m_T cosh\rho(r)}{T}\right) \tag{4.2}$$

In the above equation, I and K are the modified Bessel functions and $\rho(\mathrm{r}) = \tanh^{-1}(\beta)$, where $\beta = \beta_S(r/R)^n$. Here, β_S is the surface velocity, and r/R and n represent the relative radial position and the velocity profile parameter, respectively. The value of n is set to 1. The exponential function of the form

$$\frac{d^2N}{2\pi p_T dp_T dy} \propto e^{-\frac{m_T}{T}} \tag{4.3}$$

was also used as an alternative function for the low p_T extrapolation to determine the systematic uncertainty for dN/dy.

The rapidity spectra of K^0_s, $\overline{\Lambda}$, and $\overline{\Xi}^+$ exhibit Gaussian-like distributions, whereas the spectra of Λ and Ξ^- show broader distributions. This is mainly attributed to the extra contributions from stopped baryons. At this energy, baryons and antibaryons

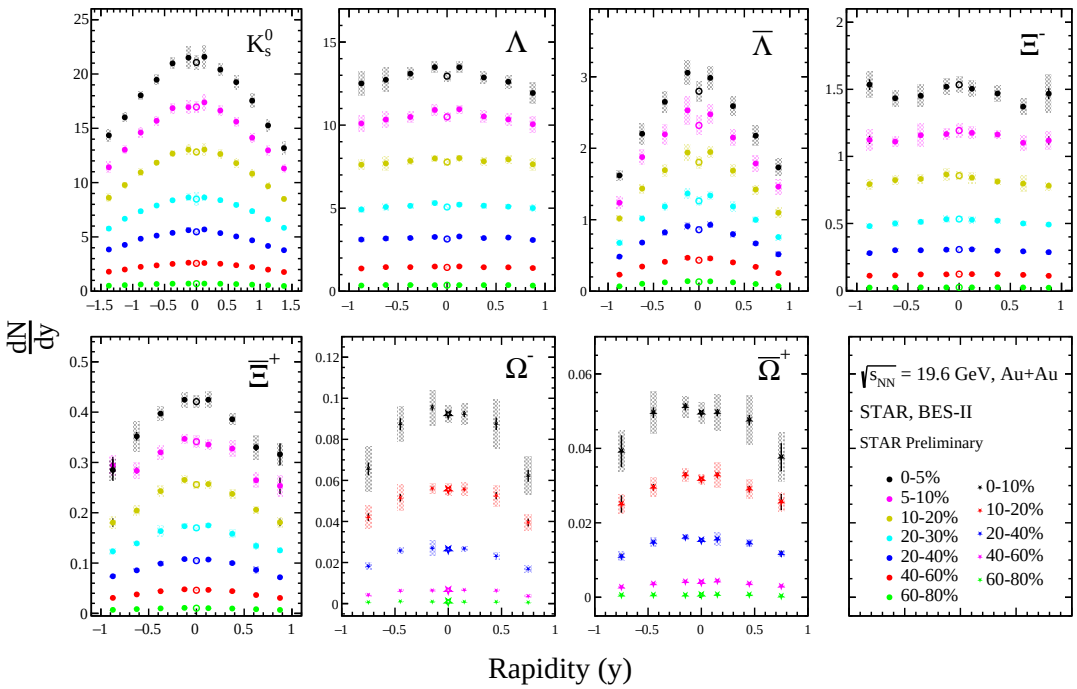

Figure 4.1: Rapidity spectra of K_s^0, Λ, $\overline{\Lambda}$, Ξ^-, $\overline{\Xi}^+$, Ω^-, and $\overline{\Omega}^+$ for different centrality ranges in Au+Au collisions at $\sqrt{s_{NN}} = 19.6$ GeV. Vertical bands indicate systematic errors.

can be produced via pair production, resulting in these effects. As a result, the distribution of baryons show a plateau at midrapidity, whereas antibaryon distribution remain Gaussian-like. The NA49 collaboration shows similar trends for baryons and antibaryons [81].

4.2 Particle yield

Figures 4.2 and 4.3 show the normalized particle yields $\mathrm{dN/dy}/(\langle N_{part}\rangle/2)$ as a function of the average number of participating nucleon pairs $\langle N_{\mathrm{part}}\rangle$ for various particles (K_s^0, Λ, $\overline{\Lambda}$, Ξ^-, $\overline{\Xi}^+$, Ω^-, $\overline{\Omega}^+$) across multiple rapidity intervals in Au+Au collisions at $\sqrt{s_{NN}} = 19.6$ GeV. Each panel represents a different particle type and is further divided to show data within specific rapidity ranges, illustrating how particle production varies with both the centrality and the rapidity of the collision. The normalization by $\langle N_{\mathrm{part}}\rangle/2$ adjusts for the average number of interacting nucleon pairs, providing a clearer comparison of particle production efficiencies across different colli-

sion centralities. These normalized yield increase from peripheral to central collisions at both negative and positive rapidities. This trend suggests a higher efficiency of particle production in more central collisions. Different rapidity ranges show consistent trends.

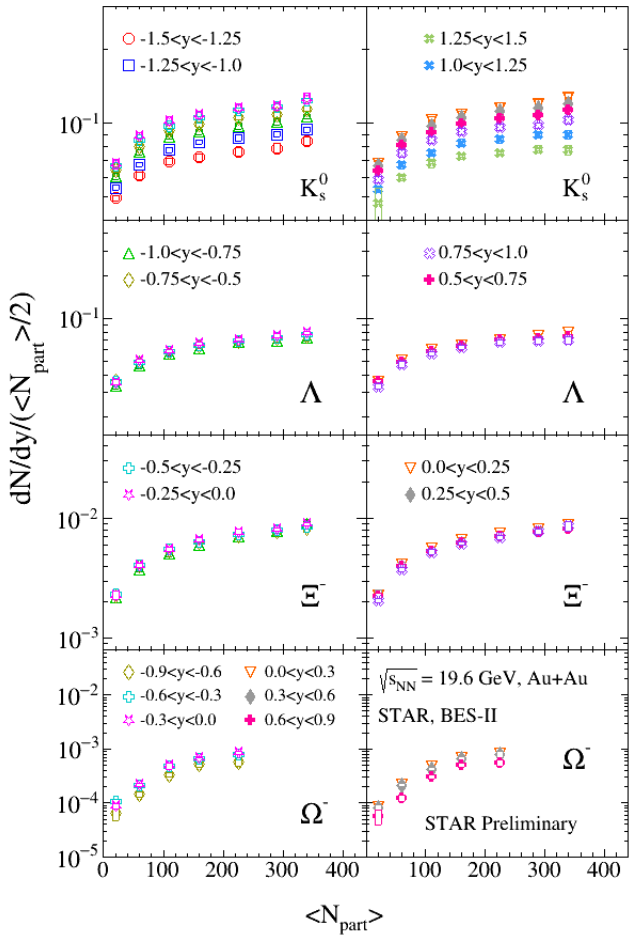

Figure 4.2: Particle yields denoted as $dN/dy/(\langle N_{\rm part}\rangle/2)$ as a function of the average number of participating nucleon pairs $\langle N_{\rm part}\rangle$ for K_s^0, Λ, Ξ^-, and Ω^- in Au+Au collisions at $\sqrt{s_{NN}}$ = 19.6 GeV. The left panels in the above figure represent $dN/dy/(\langle N_{\rm part}\rangle/2)$ in the negative rapidity region [-1.5,0] for K_s^0, [-1.0,0] for Λ, Ξ^-, and [-0.9,0] for Ω^-. The right panels represent $dN/dy/(\langle N_{\rm part}\rangle/2)$ in the positive rapidity region [0,1.5] for K_s^0, [0,1.0] for Λ, Ξ^-, and [0,0.9] for Ω^-. Systematic uncertainties are indicated by vertical bands.

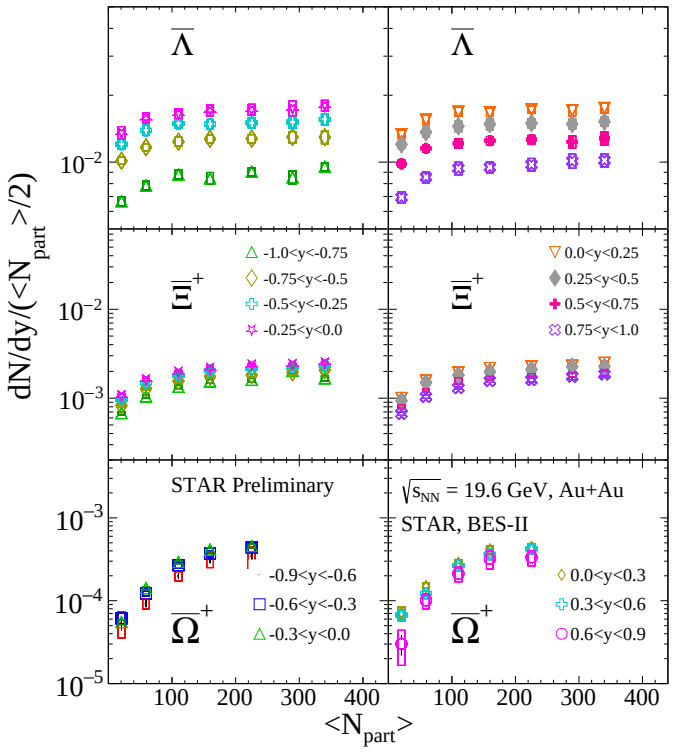

Figure 4.3: Particle yields denoted as $dN/dy/(\langle N_{\rm part}\rangle/2)$ as a function of the average number of participating nucleon pairs $\langle N_{\rm part}\rangle$ for $\overline{\Lambda}$, $\overline{\Xi}^{+}$, $\overline{\Omega}^{+}$ in Au+Au collisions at $\sqrt{s_{NN}}$ = 19.6 GeV. The left panels in the above figure represent $dN/dy/(\langle N_{\rm part}\rangle/2)$ in the negative rapidity region [-1.0,0] for $\overline{\Lambda}$, $\overline{\Xi}^{+}$, and [-0.9,0] for $\overline{\Omega}^{+}$. The right panels represent $dN/dy/(\langle N_{\rm part}\rangle/2)$ in the positive rapidity region [0,1.0] for $\overline{\Lambda}$, $\overline{\Xi}^{+}$, and [0,0.9] for $\overline{\Omega}^{+}$. Systematic uncertainties are indicated by vertical bands.

4.3 Nuclear Modification Factor (R_{cp})

Figure 4.4 shows the nuclear modification factor for K^0_s, Λ+$\overline{\Lambda}$, Ξ^-+$\overline{\Xi}^{+}$, and Ω^-+$\overline{\Omega}^{+}$ at mid-rapidity (|y|<0.5) and in a higher rapidity range (0.5<|y|<1.0) for Au+Au collisions at $\sqrt{s_{NN}}$ = 19.6 GeV. For p_T>2 GeV/c, the ratio is relatively flat and exceeds unity. This enhancement in the high p_T region could be attributed to the dominance of coalescence over fragmentation during hadronization. Apart from this, the R_{cp} values at mid-rapidity (|y|<0.5) are comparable to those at higher rapidity (0.5<|y|<1.0), suggesting minimal dependence on rapidity.

Figure 4.5 shows the R_{cp} for Λ, $\overline{\Lambda}$, Ξ^-, $\overline{\Xi}^{+}$, Ω^-, $\overline{\Omega}^{+}$ in Au+Au collisions at $\sqrt{s_{NN}}$ = 19.6 GeV. It also shows the R_{cp} results for π^-, π^+, K^+, K^-, p, and $\overline{p}$ taken from

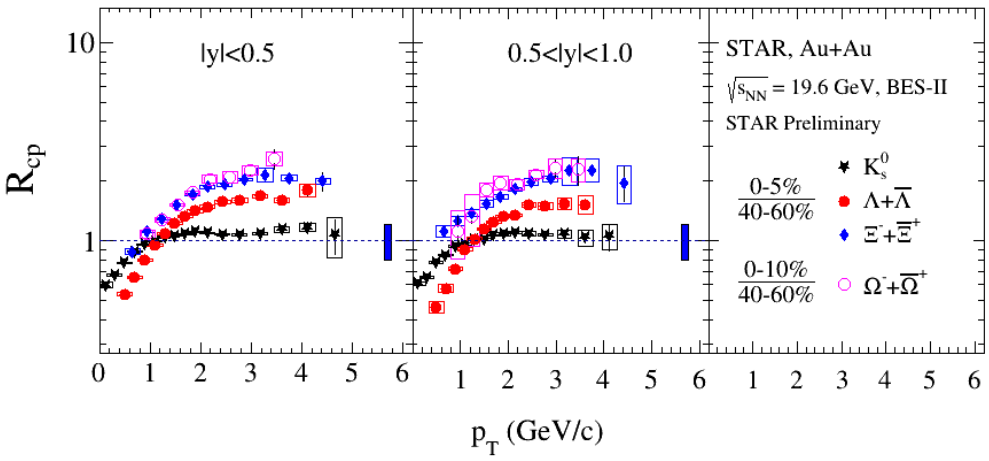

Figure 4.4: The R_{cp} values for K^0_s, $\Lambda+\overline{\Lambda}$, $\Xi^-+\overline{\Xi}^+$, and $\Omega^-+\overline{\Omega}^+$ at mid-rapidity (|y|<0.5) and higher rapidity (0.5<|y|<1.0) in Au+Au collisions at $\sqrt{s_{NN}}$ = 19.6 GeV.

[103]. We observe that the R_{cp} of particles and antiparticles of mesons are equal at low p_T region. However, the R_{cp} of antibaryons is lower than that of baryons at low p_T region. The lowering of R_{cp} of antibaryon than that of baryons may be due to the annihilation of antibaryons in a baryon-rich environment in Au+Au collisions at $\sqrt{s_{NN}}$ = 19.6 GeV.

Figure 4.6 shows the R_{cp} values for Λ and $\overline{\Lambda}$ at different collision energies. The R_{cp} of Λ, $\overline{\Lambda}$ at $\sqrt{s_{NN}}$ = 200 GeV is taken from [104]. The R_{cp} values of Λ, $\overline{\Lambda}$ at $\sqrt{s_{NN}}$ = 39 GeV and 27 GeV were calculated using the transverse momentum spectra of Λ and $\overline{\Lambda}$ taken from BES-I [37]. The R_{cp} values of Λ and $\overline{\Lambda}$ at $\sqrt{s_{NN}}$ = 19.6 GeV is calculated using the data from BES-II. We observe that the R_{cp} of Λ, $\overline{\Lambda}$ at $\sqrt{s_{NN}}$ = 200 GeV is similar to each other. For $\sqrt{s_{NN}}$ = 39 GeV and 27 GeV, the R_{cp} of $\overline{\Lambda}$ is lower than that of Λ in low p_T region. The difference between the Λ and $\overline{\Lambda}$ R_{cp} is more pronounced at $\sqrt{s_{NN}}$ = 19.6 GeV. This decrease of R_{cp} with decrease in collision energy may indicate the annihilation of antibaryons in a baryon-rich environment at low p_T.

Figure 4.7 shows a similar effect in the R_{cp} of Ξ^- and $\overline{\Xi}^+$ at different collision energies. The R_{cp} of Ξ^-, $\overline{\Xi}^+$ at $\sqrt{s_{NN}}$ = 200 GeV is taken from [104] and the R_{cp} at

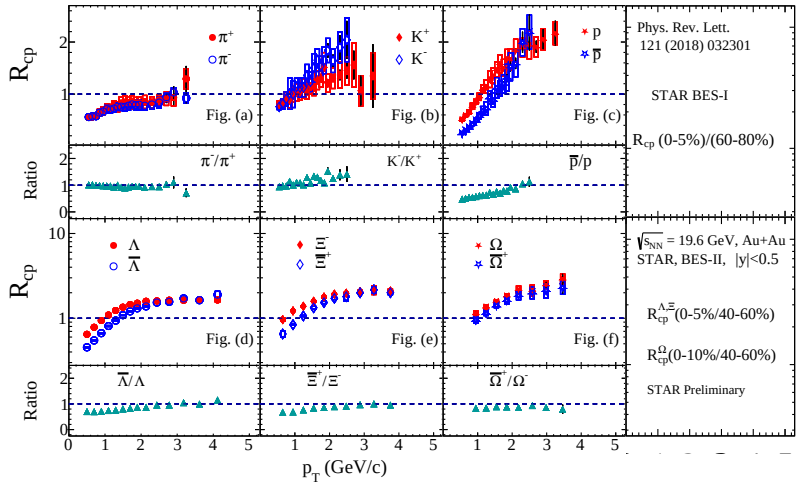

Figure 4.5: Fig. (a), Fig. (b), and Fig. (c) show the R_{cp} values for π^+, π^-, K^+, K^-, p, and $\overline{p}$ taken from [103]. Fig. (d), Fig. (e), Fig. (f) show the R_{cp} of Λ, $\overline{\Lambda}$, Ξ^-, $\overline{\Xi}^+$, Ω^-, $\overline{\Omega}^+$ in Au+Au collisions at $\sqrt{s_{NN}}$ = 19.6 GeV. The bottom panel shows ratio of antiparticle to particle.

$\sqrt{s_{NN}}$ = 2.76 TeV is calculated from the transverse momentum spectra taken from [105]. For $\sqrt{s_{NN}}$ = 39 GeV and 27 GeV, the R_{cp} of Ξ^- and $\overline{\Xi}^+$ were calculated using the transverse momentum spectra of Ξ^-, $\overline{\Xi}^+$ taken from [37]. We observe that the R_{cp} of Ξ^- and $\overline{\Xi}^+$ at $\sqrt{s_{NN}}$ = 200 GeV and 2.76 TeV is similar to each other. However, for $\sqrt{s_{NN}}$ = 39 GeV and 27 GeV, the R_{cp} of $\overline{\Xi}^+$ is lower than that of Ξ^- at low p_T region. The difference between Ξ^- and $\overline{\Xi}^+$ R_{cp} is more pronounced at $\sqrt{s_{NN}}$ = 19.6 GeV. This decrease of R_{cp} with decrease in collision energy may indicate the annihilation of antibaryons in a baryon-rich environment at low p_T.

4.4 Baryon-to-meson ratio

The baryon-to-meson (Λ/K^0_s, Ξ^-/K^0_s, Ω^-/K^0_s) ratios and antibaryon-to-meson ($\overline{\Lambda}/K^0_s$, $\overline{\Xi}^+/K^0_s$, $\overline{\Omega}^+/K^0_s$) ratios are studied at mid-rapidity (|y|<0.5) and the higher rapidity range (0.5<|y|<1.0). Figures 4.8 and 4.9 show the baryon-to-meson ratios and antibaryon-to-meson ratios, respectively, in Au+Au collisions at $\sqrt{s_{NN}}$ = 19.6 GeV. An enhancement in the baryon-to-meson ratios and antibaryon-to-meson ratios is observed at intermediate p_T in most central collisions compared to peripheral collisions. This enhancement may be significantly influenced by hadron formation through par-

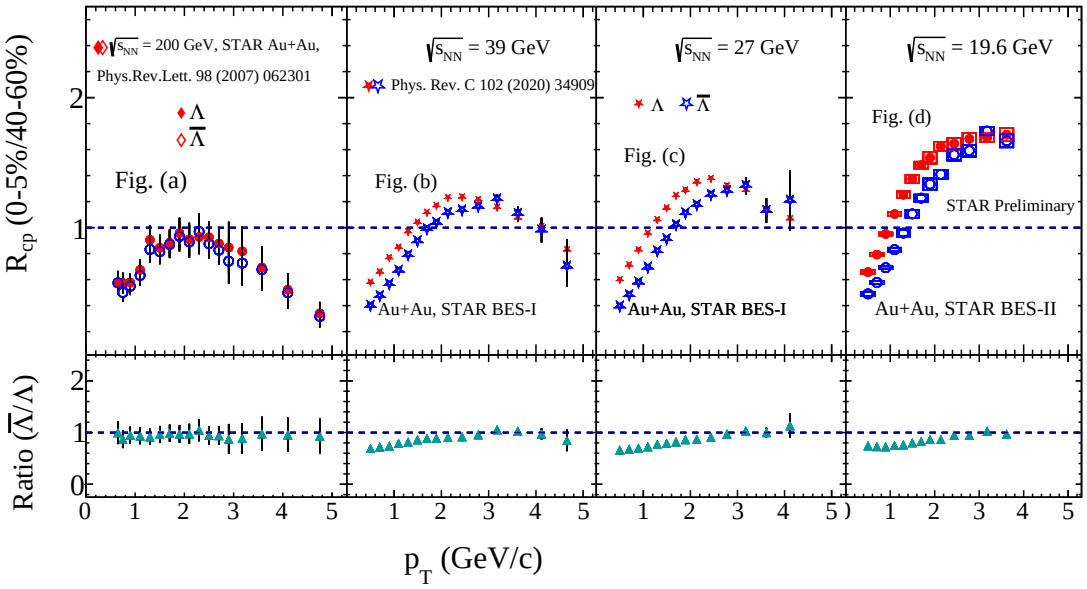

Figure 4.6: The R_{cp} of Λ, $\overline{\Lambda}$ at different collision energies from $\sqrt{s_{NN}}$ = 200 GeV, 39 GeV, 27 GeV, and 19.6 GeV. The lower panel compares the ratio of R_{cp} of Λ and $\overline{\Lambda}$.

ton recombination in the dense and thermalized medium of central collisions. The enhancement decrease progressively from Λ/K_s^0 ($\overline{\Lambda}/K_s^0$) ratio to Ξ^-/K_s^0 ($\overline{\Xi}^+/K_s^0$), and Ω^-/K_s^0 ($\overline{\Omega}^+/K_s^0$). This trend suggests a hierarchy in baryon production relative to meson production, influenced by the varying masses and quark compositions of these particles. Further, a clear rapidity dependence was observed between mid-rapidity ($|y|<0.5$) and the larger rapidity range ($0.5<|y|<1.0$) in both baryon-to-meson ratios and antibaryon-to-meson ratios.

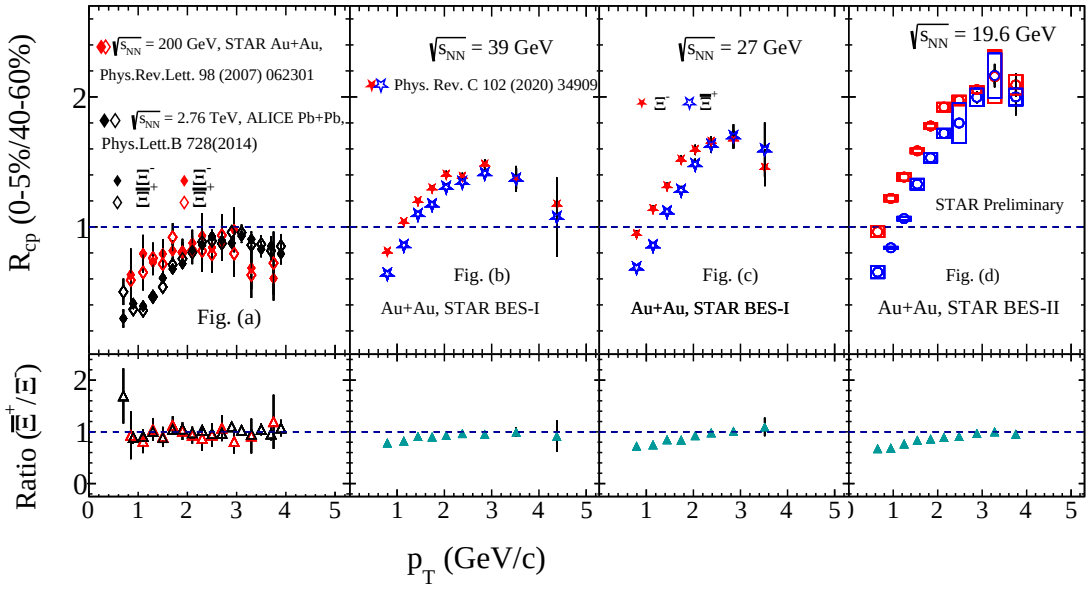

Figure 4.7: The R_{cp} of Ξ^-, $\overline{\Xi}^+$ at different collision energies from $\sqrt{s_{NN}} = 2.76$ TeV, 200 GeV, 39 GeV, 27 GeV, and 19.6 GeV. The lower panel compares the ratio of R_{cp} of Ξ^- and $\overline{\Xi}^+$.

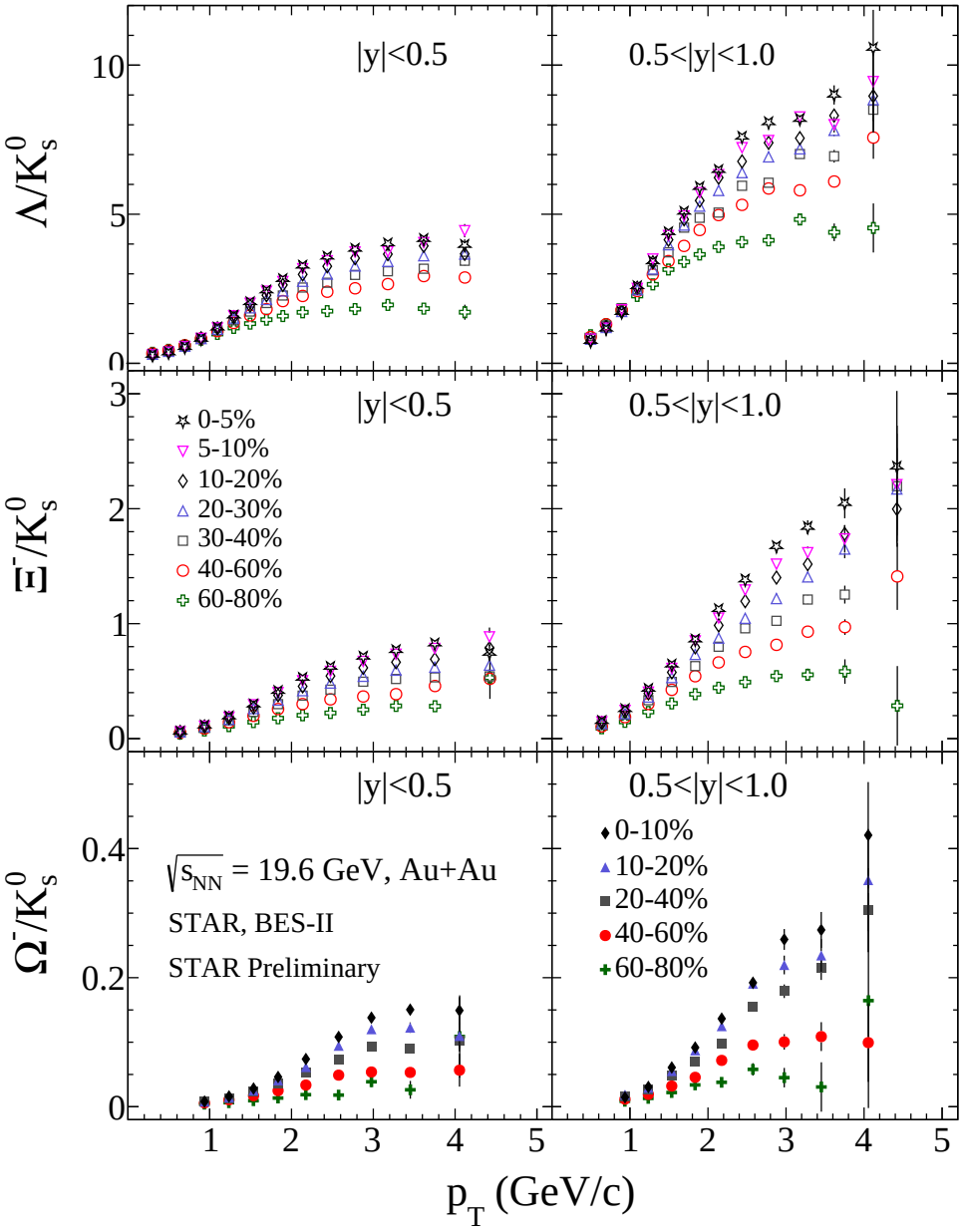

Figure 4.8: Λ/K^0_s, Ξ^-/K^0_s, Ω^-/K^0_s ratios at mid-rapidity (|y|<0.5) and higher rapidity (0.5<|y|<1.0), as a function of p_T in Au+Au collisions at $\sqrt{s_{NN}}$ = 19.6 GeV.

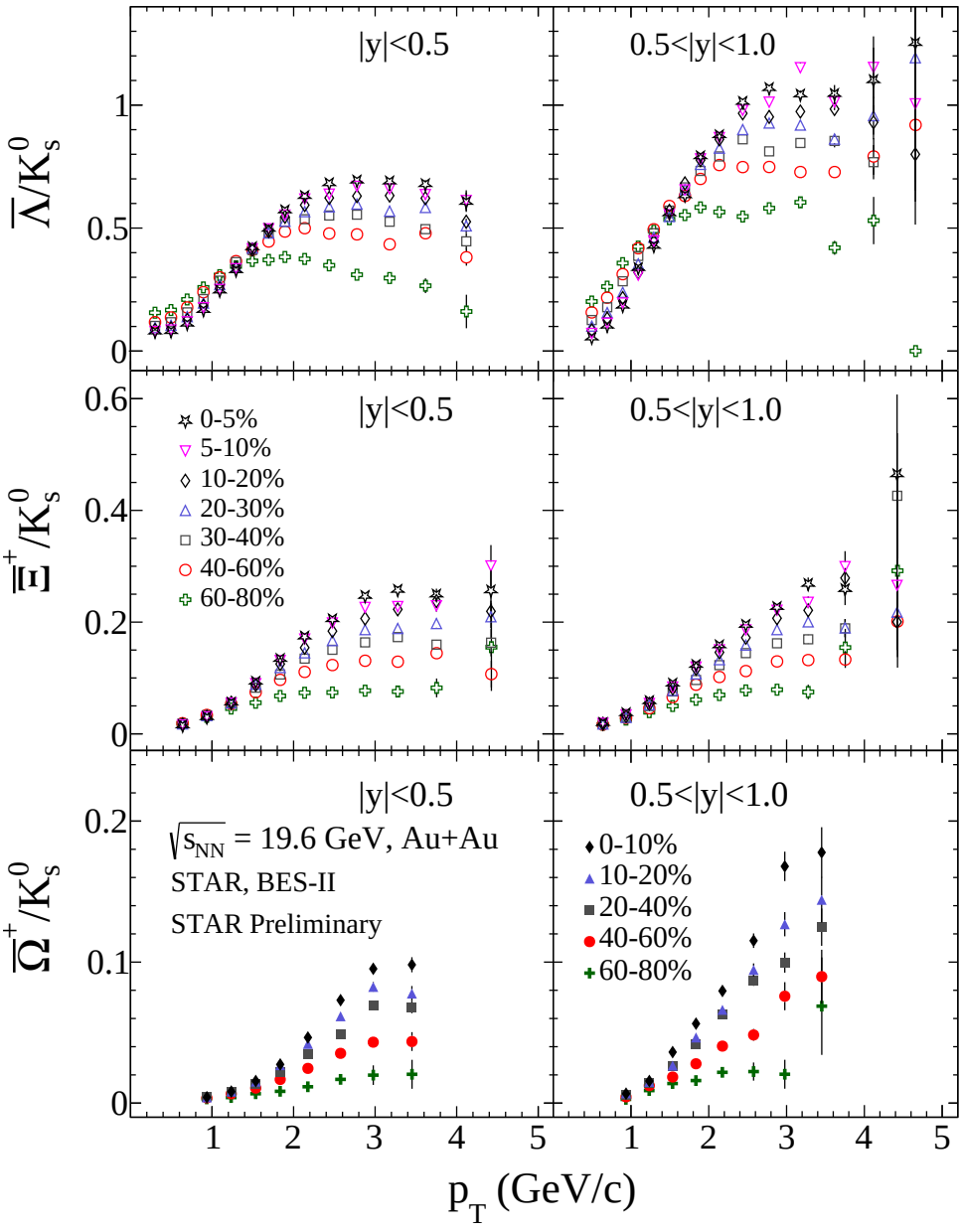

Figure 4.9: $\overline{\Lambda}/K^0_s$, $\overline{\Xi}^+/K^0_s$, $\overline{\Omega}^+/K^0_s$ ratios at mid-rapidity (|y|<0.5) and higher rapidity (0.5<|y|<1.0), as a function of p_T in Au+Au collisions at $\sqrt{s_{NN}}$ = 19.6 GeV.

This page is intentionally left blank

Chapter 5

Conclusion and outlook

In this thesis, we investigated the production of strange and multi-strange particles in Au+Au collisions at $\sqrt{s_{NN}} = 19.6$ GeV as part of the BES-II program. The significant upgrade in the inner Time Projection Chamber (iTPC) during BES-II has enabled us to extend the rapidity range from the previous BES analysis at mid-rapidity (|y|<0.5) to a higher range (|y|<1.0) for $\Lambda(\overline{\Lambda})$, $\Xi^{-}(\overline{\Xi}^{+})$ and for |y|<0.9 for $\Omega^{-}(\overline{\Omega}^{+})$.

We studied the rapidity spectra of strange and multi-strange particles. The results indicated that the rapidity spectra of particles are wider compared to those of antiparticles and K^0_s meson, which exhibited a more Gaussian-like distribution. This is mainly due to the extra contributions from stopped baryons, where baryons are more likely to be stopped in the collision zone, leading to a wider distribution. The baryon stopping is a process where incoming nucleons lose a significant portion of their longitudinal momentum, effectively becoming part of the hot, dense medium created in the collision. This mechanism results in a higher density of baryons at mid-rapidity, thus widening their rapidity distribution compared to that of K^0_s meson and antiparticles.

The R_{cp} at mid-rapidity (|y|<0.5) and higher rapidity (0.5<|y|<1.0) does not show much rapidity dependence. Apart from this, we also studied the R_{cp} of particles and antiparticles separately. We observed that the R_{cp} of antibaryons is lower than that of baryons at low p_T, indicating the annihilation of antibaryons in a baryon-rich

environment at low p_T. Moreover, this effect decreases from the R_{cp} of $\Lambda(\overline{\Lambda})$ to the R_{cp} of $\Xi^-(\overline{\Xi}^+)$ and $\Omega^-(\overline{\Omega}^+)$. We also compared the separate R_{cp} of baryons and antibaryons at different collision energies and observed that the R_{cp} of antibaryons show a distinct split at low p_T from that of baryons with decreasing collision energies.

We also studied the baryon-to-meson ratios (Λ/K^0_s, Ξ^-/K^0_s, Ω^-/K^0_s), and antibaryon-to-meson ratios ($\overline{\Lambda}/K^0_s$, $\overline{\Xi}^+/K^0_s$, $\overline{\Omega}^+/K^0_s$ at both mid-rapidity (|y|<0.5) and higher rapidity (0.5<|y|<1.0). We observed an enhancement in the ratio of Λ/K^0_s ($\overline{\Lambda}/K^0_s$) at intermediate p_T in the most central collisions compared to peripheral collisions at mid-rapidity (|y|<0.5) as well as at higher rapidity (0.5<|y|<1.0). This enhancement was found to decrease as we moved from Λ/K^0_s ($\overline{\Lambda}/K^0_s$) ratio to Ξ^-/K^0_s ($\overline{\Xi}^+/K^0s$), and Ω^-/K^0_s ($\overline{\Omega}^+/K^0_s$). This trend may indicate a hierarchy in the enhancement of baryon production relative to meson production, which is most pronounced for $\Lambda(\ \overline{\Lambda})$ and diminishes for $\Xi^-(\overline{\Xi}^+)$, and $\Omega^-(\overline{\Omega}^+)$. The decreasing enhancement could be due to the varying masses and quark compositions of these particles. Multi-strange baryons such as Ξ^-, $\overline{\Xi}^+$ and Ω^-, $\overline{\Omega}^+$ have higher masses and contain more strange quarks, making them less abundant and more sensitive to the conditions in the medium. Further, a clear rapidity dependence was observed between mid-rapidity (|y|<0.5) and the higher rapidity (0.5<|y|<1.0) in both baryon-to-meson ratios and antibaryon-to-meson ratios.

In conclusion, the observed split in R_{cp} of baryons and antibaryons at low p_T, the wider rapidity spectra of baryons compared to antibaryons, and the varying enhancements in baryon-to-meson ratios at different centralities for strange and multi-strange particles provide compelling evidence of the complex interplay between hadronic and partonic interactions in the dense medium created in Au+Au collisions at $\sqrt{s_{NN}}$ = 19.6 GeV.

The results presented in this thesis are restricted to rapidity |y|<1.0 for $\Lambda(\overline{\Lambda})$, $\Xi^-(\overline{\Xi}^+)$ and for |y|<0.9 for $\Omega^-(\overline{\Omega}^+)$. The rapidity range beyond ±1.0 for $\Lambda(\overline{\Lambda})$ and $\Xi^-(\overline{\Xi}^+)$ and beyond ±0.9 for $\Omega^-(\overline{\Omega}^+)$ does not provide a clear signal-to-background ratio, making signal extraction in these ranges challenging. The signal-to-background

ratio in the invariant mass distribution of strange hadrons at larger rapidity can be improved by using sophisticated machine learning techniques. One such effective approach is utilizing the TMVA (Toolkit for Multivariate Analysis) framework, which is a ROOT-based package. Moreover, the STAR experiment has taken data at other energies like the $\sqrt{s_{NN}}$ = 7.7, 9.2, 11.5, 14.5, and 17.3 GeV for Au+Au collisions. The enhancement in baryon-to-meson ratios and antibaryon-to-meson ratios in the most central collisions compared to peripheral collisions at intermediate p_T and their rapidity dependence can be further evaluated at these lower center-of-mass energies. The baryon-stopping effect observed in the case of particles in Au+Au collisions at $\sqrt{s_{NN}}$ = 19.6 GeV, as indicated by the rapidity spectra, can be evaluated at different collision energies.

This page is intentionally left blank

Conference proceedings

1. S.Aslam (for the STAR Collaboration), "Production of Λ and $\overline{\Lambda}$ in Au+Au collisions at $\sqrt{s_{NN}}$ = 19.6 GeV at RHIC", *Proceedings of the DAE Symp. on Nucl. Phys. 66* (2022) 944-945.

2. S.Aslam (for the STAR Collaboration), "Strange baryons production in Au+Au collisions at $\sqrt{s_{NN}}$ = 19.6 GeV from STAR", *Springer Proceedings in Physics*, (SPPHY, volume 304).

Conferences and workshops

1. "Strangeness production in Au+Au collisions at $\sqrt{s_{NN}}$ = 19.6 GeV with the STAR Experiment", 3^{rd} International Conference on Advancement in Core and Frontier of Physics (ACFP-2024), Department of Physics, GLA University, Mathura, India, 02-04 February 2024 (Talk) (**first best oral presentation award under Nuclear and High Energy Physics track**)

2. "Strange baryons production in Au+Au collisions at $\sqrt{s_{NN}}$ = 19.6 GeV from STAR", XXV DAE-BRNS High Energy Physics Symposium 2022, IISER Mohali, India, 12-16 December, 2022 (Poster).

3. "Production of Λ and $\bar{\Lambda}$ in Au+Au collisions at $\sqrt{s_{NN}}$ = 19.6 GeV at RHIC", 66th DAE Symposium on nuclear physics, Cotton University, Guwahati, India, 1-5 December 2022 (Poster).

4. "Strangeness production in Au+Au collisions at $\sqrt{s_{NN}}$ = 19.6 GeV from STAR", The $20th$ International Conference on Strangeness in Quark Matter (SQM), Busan, Republic of Korea, 13-17 June 2022 (Poster).

5. SERB Sponsored One Week Online High-End Workshop (Karyashala) on "Software Tools and Techniques used in EHEP and its Applications", Organized by Department of Physics & ECE, Malaviya National Institute of Technology Jaipur, India, July 12-19 2021 (attended).

6. IV ALICE India school on Quark-Gluon Plasma, organized by ALICE-India Collaboration, 8-20 Nov, 2021 (attended).

7. 1st workshop on "Physics performance studies at FAIR and NICA (FANI-2020)", Online, 24-28 August 2020 (attended).

This page is intentionally left blank

Appendix A

Appendix

A.1 Acceptance × Reconstruction Efficiency

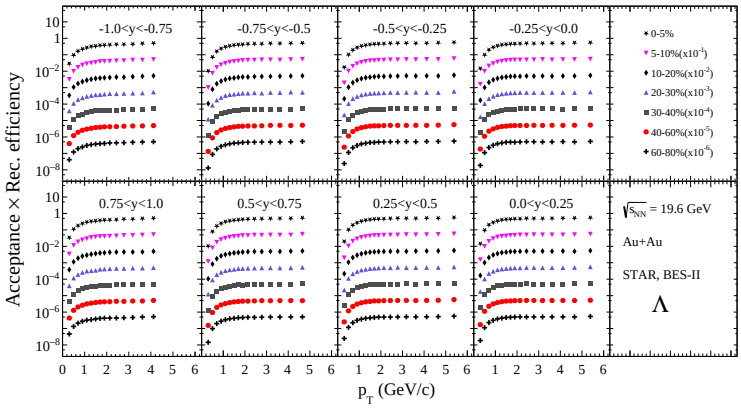

Figure A.1: The acceptance × reconstruction efficiencies of Λ under the rapidity range [-1,1] in different collision centralities in Au+Au collisions at $\sqrt{s_{NN}}$ = 19.6 GeV.

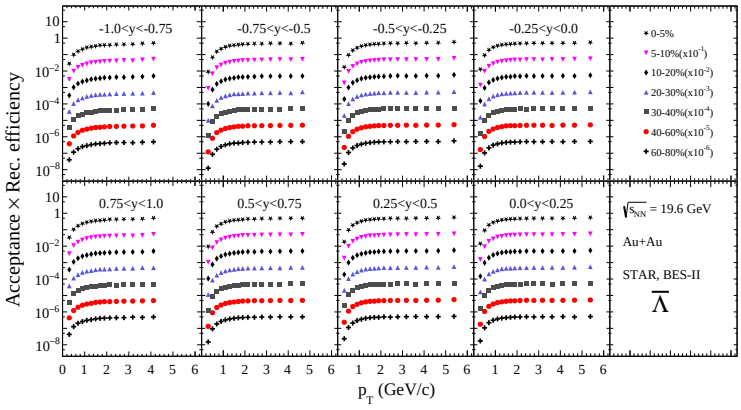

Figure A.2: The acceptance × reconstruction efficiencies of $\overline{\Lambda}$ under the rapidity range [-1,1] in different collision centralities in Au+Au collisions at $\sqrt{s_{NN}}$ = 19.6 GeV.

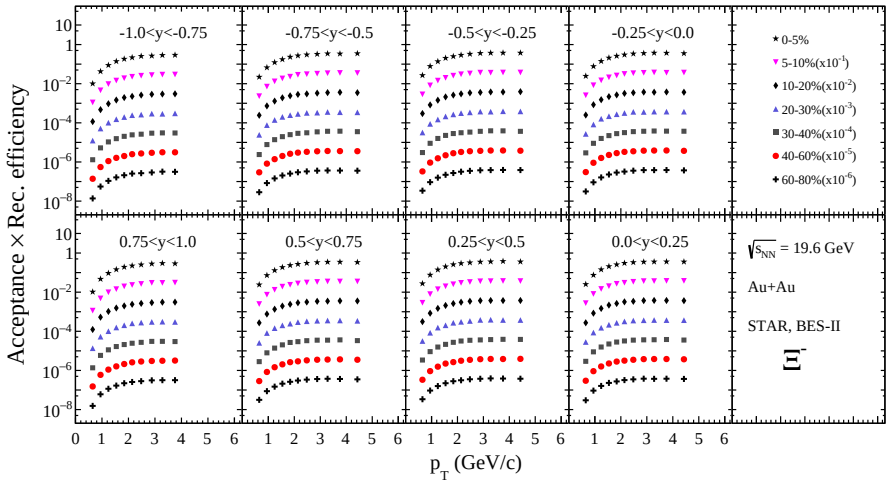

Figure A.3: The acceptance × reconstruction efficiencies of Ξ^- under the rapidity range [-1.0,1.0] in different collision centralities in Au+Au collisions at $\sqrt{s_{NN}} = 19.6$ GeV.

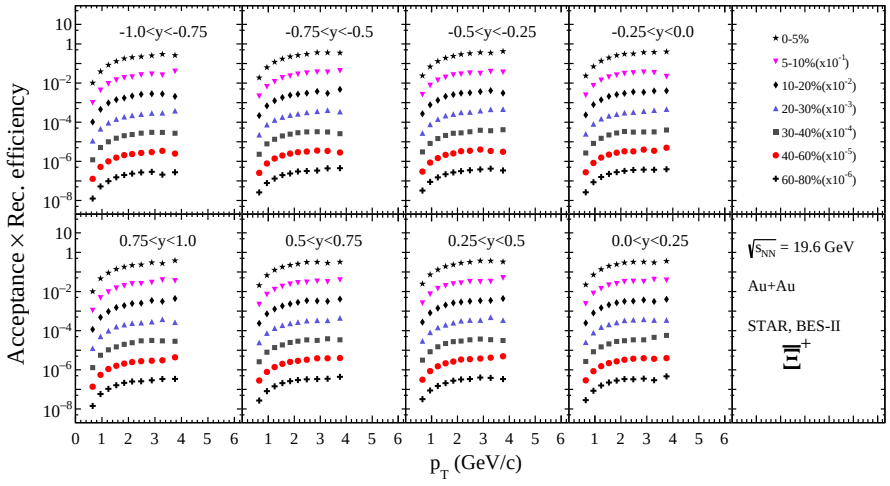

Figure A.4: The acceptance × reconstruction efficiencies of $\overline{\Xi}^+$ under the rapidity range [-1.0,1.0] in different collision centralities in Au+Au collisions at $\sqrt{s_{NN}} = 19.6$ GeV.

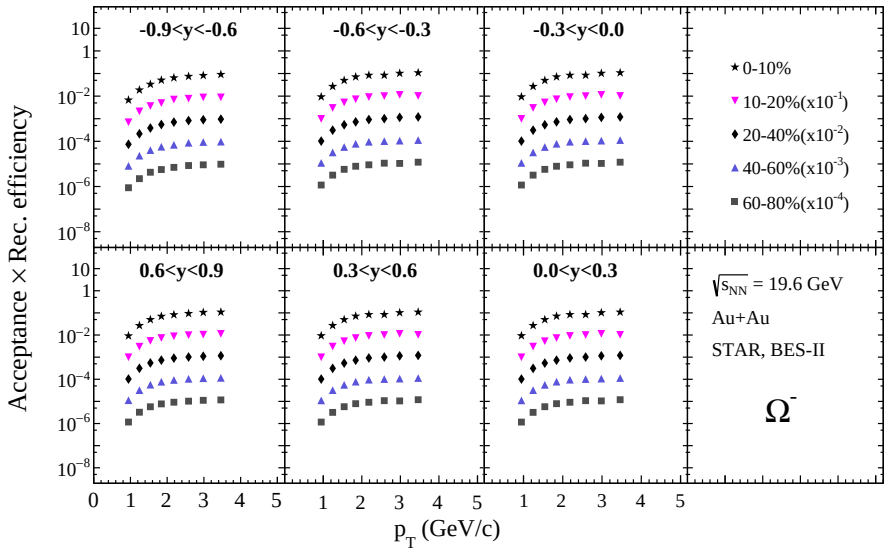

Figure A.5: The acceptance × reconstruction efficiencies of Ω^- under the rapidity range [-0.9, 0.9] in different collision centralities in Au+Au collisions at $\sqrt{s_{NN}} = 19.6$ GeV.

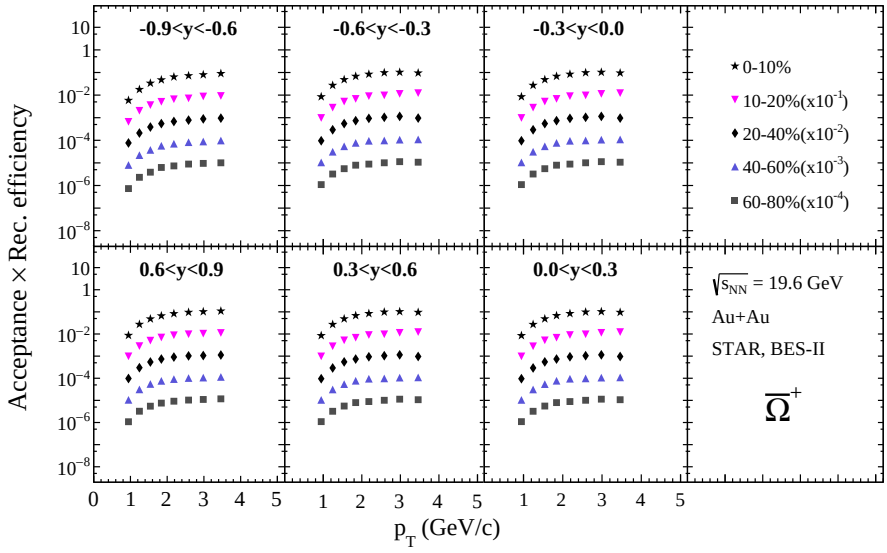

Figure A.6: The acceptance × reconstruction efficiencies of $\overline{\Omega}^+$ under the rapidity range [-0.9, 0.9] in different collision centralities in Au+Au collisions at $\sqrt{s_{NN}} = 19.6$ GeV.

This page is intentionally left blank

Bibliography

[1] K. Adcox *et al.*, "Formation of dense partonic matter in relativistic nucleus–nucleus collisions at RHIC: experimental evaluation by the PHENIX collaboration," *Nucl. Phys. A*, vol. 757, no. 1-2, pp. 184–283, 2005.

[2] S. L. Glashow, "Partial-symmetries of weak interactions," *Nucl. Phys.*, vol. 22, no. 4, pp. 579–588, 1961.

[3] S. Weinberg, "A model of leptons," *Phys. Rev. Lett.*, vol. 19, no. 21, p. 1264, 1967.

[4] A. Salam and J. Ward, "Electromagnetic and weak interactions," *Phys. Lett.*, vol. 13, pp. 168–171, 1964.

[5] G. Aad *et al.*, "Observation of a new particle in the search of the Standard Model Higgs boson with the ATLAS detector at the LHC," *Phys. Lett. B*, vol. 716, pp. 1–29, 2012.

[6] S. Chatrchyan *et al.*, "Observation of a new boson at a mass of 125 GeV with the CMS experiment at the LHC," *Phys. Lett. B*, vol. 716, pp. 30–61, 2012.

[7] D. J. Gross and F. Wilczek, "Asymptotically free gauge theories-I," *Phys. Rev. D*, vol. 8, no. 10, p. 3633, 1973.

[8] K. G. Wilson, "Confinement of quarks," *Phys. Rev. D*, vol. 10, no. 8, p. 2445, 1974.

[9] A. Deur, S. J. Brodsky, and G. F. de Teramond, "Connecting the hadron mass scale to the fundamental mass scale of quantum chromodynamics," *Phys. Lett. B*, vol. 750, pp. 528–532, 2015.

[10] Y. Akiba *et al.*, "The hot QCD white paper: exploring the phases of QCD at RHIC and the LHC," *arXiv preprint arXiv:1502.02730*, 2015.

[11] Y. Hatta and T. Ikeda, "Universality, the QCD critical and tricritical point, and the quark number susceptibility," *Phys. Rev. D*, vol. 67, no. 1, p. 014028, 2003.

[12] S. Gupta, X. Luo, B. Mohanty, H. G. Ritter, and N. Xu, "Scale for the phase diagram of quantum chromodynamics," *Science*, vol. 332, no. 6037, pp. 1525–1528, 2011.

[13] Y. Hatta and M. Stephanov, "Proton-number fluctuation as a signal of the QCD critical end point," *Phys. Rev. Lett.*, vol. 91, no. 10, p. 102003, 2003.

[14] J. D. Bjorken, "Highly relativistic nucleus-nucleus collisions: The central rapidity region," *Phys. Rev. D*, vol. 27, no. 1, p. 140, 1983.

[15] https://particlesandfriends.wordpress.com/2016/10/14/evolution-of-collisions-and qgp/.

[16] J. Rafelski and B. Müller, "Strangeness production in the quark-gluon plasma," *Phys. Rev. Lett.*, vol. 48, no. 16, p. 1066, 1982.

[17] J. Adams *et al.*, "Experimental and theoretical challenges in the search for the quark-gluon plasma: The STAR Collaboration's critical assessment of the evidence from RHIC collisions," *Nucl. Phys. A*, vol. 757, no. 1-2, pp. 102–183, 2005.

[18] Abelev *et al.*, "Enhanced strange baryon production in Au+Au collisions compared to p+p at $\sqrt{s_{\mathrm{NN}}} = 200\,\mathrm{GeV}$," *Phys. Rev. C*, vol. 77, no. 4, p. 044908, 2008.

[19] J. Adams, Adler *et al.*, "Transverse-Momentum and Collision-Energy Dependence of High-pT Hadron Suppression in Au+Au Collisions at Ultrarelativistic Energies," *Phys. Rev. Lett.*, vol. 91, no. 17, p. 172302, 2003.

[20] K. Adcox, Adler *et al.*, "Centrality dependence of the high pT charged hadron suppression in Au+Au collisions at $\sqrt{s_{\mathrm{NN}}} = 130\,\mathrm{GeV}$," *Phys. Lett. B*, vol. 561, no. 1-2, p. 82, 2003.

[21] J. Adams, Adler *et al.*, "Evidence from d+Au Measurements for Final-State Suppression of High-pT Hadrons in Au+Au Collisions at RHIC," *Phys. Rev. Lett.*, vol. 91, no. 7, p. 072304, 2003.

[22] C. Adler *et al.*, "Disappearance of Back-To-Back High-pT Hadron Correlations in Central Au+Au Collisions at $\sqrt{s_{\mathrm{NN}}} = 200\,\mathrm{GeV}$," *Phys. Rev. Lett.*, vol. 90, no. 8, p. 082302, 2003.

[23] J. Adams *et al.*, "Azimuthal anisotropy in Au+Au collisions at $\sqrt{s_{\mathrm{NN}}} = 200\,\mathrm{GeV}$," *Phys. Rev. C*, vol. 72, no. 1, p. 014904, 2005.

[24] Abelev *et al.*, "Centrality dependence of charged hadron and strange hadron elliptic flow from $\sqrt{s_{\mathrm{NN}}} = 200\,\mathrm{GeV}$ Au+Au collisions," *Phys. Rev. C Nuclear Physics*, vol. 77, no. 5, p. 054901, 2008.

[25] J. Adams *et al.*, "Scaling properties of hyperon production in Au+Au collisions at $\sqrt{s_{\mathrm{NN}}} = 200\,\mathrm{GeV}$," *Phys. Rev. Lett.*, vol. 98, no. 6, p. 062301, 2007.

[26] Afanasiev *et al.*, "Elliptic flow for ϕ mesons and (anti)deuterons in Au+Au collisions at $\sqrt{s_{\mathrm{NN}}} = 200\,\mathrm{GeV}$," *Phys. Rev. Lett.*, vol. 99, no. 5, p. 052301, 2007.

[27] J. Adams *et al.*, "Azimuthal anisotropy at the relativistic heavy ion collider: the first and fourth harmonics," *Phys. Rev. Lett.*, vol. 92, no. 6, p. 062301, 2004.

[28] L. Adamczyk *et al.*, "Direct virtual photon production in Au+Au collisions at $\sqrt{s_{\rm NN}} = 200\,\text{GeV}$," *Phys. Lett. B*, vol. 770, pp. 451–458, 2017.

[29] Aggarwal *et al.*, "An Experimental Exploration of the QCD Phase Diagram: The Search for the Critical Point and the Onset of De-confinement," *arXiv preprint arXiv:1007.2613*, 2010.

[30] https://drupal.star.bnl.gov/STAR/files/BES_WPII_ver6.9_Cover.pdf.

[31] Adamczyk *et al.*, "Energy Dependence of Moments of Net-Proton Multiplicity distributions at RHIC," *Phys. Rev. Lett.*, vol. 112, no. 3, p. 032302, 2014.

[32] R. Esha *et al.*, "Measurement of the cumulants of net-proton multiplicity distribution in Au+Au collisions at $\sqrt{s_{\rm NN}} = 7.7 - 200\,\text{GeV}$ from the STAR experiment," *Nuclear Physics A*, vol. 967, pp. 457–460, 2017.

[33] Adamczyk *et al.*, "Beam energy dependence of moments of the net-charge multiplicity distributions in Au+Au collisions at RHIC," *Phys. Rev. Lett.*, vol. 113, no. 9, p. 092301, 2014.

[34] L. Adamczyk *et al.*, "Beam-Energy Dependence of the Directed Flow of Protons, Antiprotons, and Pions in Au+Au collisions," *Phys. Rev. Lett.*, vol. 112, no. 16, p. 162301, 2014.

[35] A. M. Poskanzer and S. A. Voloshin, "Methods for analyzing anisotropic flow in relativistic nuclear collisions," *Phys. Rev. C*, vol. 58, no. 3, p. 1671, 1998.

[36] L. Adamczyk *et al.*, "Elliptic flow of identified hadrons in Au+Au collisions at $\sqrt{s_{\rm NN}} = 7.7 - 62.4\,\text{GeV}$ GeV," *Phys. Rev. C Nuclear Physics*, vol. 88, no. 1, p. 014902, 2013.

[37] J. Adam *et al.*, "Strange hadron production in Au+Au collisions at $\sqrt{s_{\rm NN}} = 7.7 - 39\,\text{GeV}$," *Phys. Rev. C*, vol. 102, no. 3, p. 034909, 2020.

[38] L. Adamczyk *et al.*, "Beam Energy Dependence of Jet-Quenching Effects in Au+ Au Collisions at $\sqrt{s_{\rm NN}} = 7.7 - 62.4\,\text{GeV}$," *Phys. Rev. Lett.*, vol. 121, no. 3, p. 032301, 2018.

[39] G. Odyniec, "Future of the beam energy scan program at RHIC," in *EPJ Web of Conferences*, vol. 95. EDP Sciences, 2015, p. 03027.

[40] S. Collaboration, "A Proposal for STAR Inner TPC Sector Upgrade (iTPC)," *STAR Note*, vol. 619, 2015.

[41] G. Odyniec, "The RHIC Beam Energy Scan program in STAR and what's next...," in *Journal of Physics: Conference Series*, vol. 455, no. 1. IOP Publishing, 2013, p. 012037.

[42] K. Redlich and A. Tounsi, "Strangeness enhancement and energy dependence in heavy ion collisions," *The European Physical Journal C-Particles and Fields*, vol. 24, no. 4, pp. 589–594, 2002.

[43] Abelev *et al.*, "Energy and system size dependence of ϕ meson production in Cu+Cu and Au+Au collisions," *Phys. Lett. B*, vol. 673, no. 3, pp. 183–191, 2009.

[44] J. Adams *et al.*, "ϕ meson production in Au+Au and p+p collisions at $\sqrt{s_{\mathrm{NN}}} = 200\,\mathrm{GeV}$," *Phys. Lett. B*, vol. 612, no. 3-4, pp. 181–189, 2005.

[45] T. Åkesson *et al.*, "Inclusive vector-meson production in the central region of pp collisions at $\sqrt{s} = 63\,\mathrm{GeV}$," *Nucl. Phys. B*, vol. 203, no. 1, pp. 27–39, 1982.

[46] X.-N. Wang and M. Gyulassy, "Gluon shadowing and jet quenching in A+A collisions at $\sqrt{s} = 200A\,\mathrm{GeV}$," *Phys. Rev. Lett.*, vol. 68, no. 10, p. 1480, 1992.

[47] C. Adler *et al.*, "Centrality dependence of high-pT hadron suppression in Au+Au collisions at $\sqrt{s_{\mathrm{NN}}} = 200\,\mathrm{GeV}$," *Phys. Rev. Lett.*, vol. 89, no. 20, p. 202301, 2002.

[48] R. Baier, Y. L. Dokshitzer, A. H. Mueller, S. Peigne, and D. Schiff, "Radiative energy loss of high energy quarks and gluons in a finite-volume quark-gluon plasma," *Nucl. Phys. B*, vol. 483, no. 1-2, pp. 291–320, 1997.

[49] M. Gyulassy and M. Plumer, "Jet quenching in dense matter," *Phys. Lett. B*, vol. 243, p. 432, 1990.

[50] J. Adams *et al.*, "Evidence from d+Au Measurements for Final-State Suppression of High-pT Hadrons in Au+Au Collisions at RHIC," *Phys. Rev. Lett.*, vol. 91, no. 7, p. 072304, 2003.

[51] C. Adler *et al.*, "Disappearance of Back-To-Back High-pT Hadron Correlations in Central Au+Au Collisions at $\sqrt{s_{\mathrm{NN}}} = 200\,\mathrm{GeV}$," *Phys. Rev. Lett.*, vol. 90, no. 8, p. 082302, 2003.

[52] P. Huovinen, P. F. Kolb, U. Heinz, P. Ruuskanen, and S. A. Voloshin, "Radial and elliptic flow at RHIC: Further predictions," *Phys. Lett. B*, vol. 503, no. 1-2, pp. 58–64, 2001.

[53] R. Nouicer, "New state of nuclear matter: Nearly perfect fluid of quarks and gluons in heavy-ion collisions at RHIC energies: From charged particle density to jet quenching," *The European Physical Journal Plus*, vol. 131, no. 3, p. 70, 2016.

[54] R. Snellings, "Elliptic flow: a brief review," *New Journal of Physics*, vol. 13, no. 5, p. 055008, 2011.

[55] J. Adams *et al.*, "Directed flow in Au+Au collisions at $\sqrt{s_{\mathrm{NN}}} = 62.4\,\mathrm{GeV}$," *Phys. Rev. C*, vol. 73, no. 3, p. 034903, 2006.

[56] L. Bravina, N. Amelin, L. Csernai, P. Levai, and D. Strottman, "Fluid dynamics and Quark-Gluon string model—What we can expect for Au+Au collisions at 11.6 AGeVc," *Nucl. Phys. A*, vol. 566, pp. 461–464, 1994.

[57] L. Bravina, L. Csernai, P. Levai, and D. Strottman, "Collective global dynamics in Au+Au collisions at the BNL AGS," *Phys. Rev. C*, vol. 50, no. 4, p. 2161, 1994.

[58] L. P. Csernai and D. Röhrich, "Third flow component as QGP signal," *Phys. Lett. B*, vol. 458, no. 4, pp. 454–459, 1999.

[59] Z.-w. Lin and C. M. Ko, "Partonic effects on the elliptic flow at relativistic heavy ion collisions," *Phys. Rev. C*, vol. 65, no. 3, p. 034904, 2002.

[60] L.-W. Chen and C. M. Ko, "Partonic effects on anisotropic flows at RHIC," *Journal of Physics G: Nuclear and Particle Physics*, vol. 31, no. 4, p. S49, 2005.

[61] H. Sorge, "Elliptical flow: A Signature for early pressure in ultrarelativistic nucleus-nucleus collisions," *Phys. Rev. Lett.*, vol. 78, no. 12, p. 2309, 1997.

[62] S. Bass *et al.*, "Microscopic models for ultrarelativistic heavy ion collisions," *Progress in Particle and Nuclear Physics*, vol. 41, pp. 255–369, 1998.

[63] M. Bleicher *et al.*, "Relativistic hadron-hadron collisions in the ultra-relativistic quantum molecular dynamics model," *Journal of Physics G: Nuclear and Particle Physics*, vol. 25, no. 9, p. 1859, 1999.

[64] P. F. Kolb and U. Heinz, "Hydrodynamic description of ultrarelativistic heavy-ion collisions," pp. 634–714, 2004.

[65] J. Adams *et al.*, "Azimuthal anisotropy in Au+ Au collisions at $\sqrt{s_{\mathrm{NN}}} = 200\,\mathrm{GeV}$," *Phys. Rev. C*, vol. 72, no. 1, p. 014904, 2005.

[66] F. Retiere and M. A. Lisa, "Observable implications of geometrical and dynamical aspects of freeze-out in heavy ion collisions," *Phys. Rev. C*, vol. 70, no. 4, p. 044907, 2004.

[67] U. Heinz and P. Kolb, "Early thermalization at RHIC," *Nucl. Phys. A*, vol. 702, p. 269, 2002.

[68] D. Molnar and S. A. Voloshin, "Elliptic flow at large transverse momenta from quark coalescence," *Phys. Rev. Lett.*, vol. 91, no. 9, p. 092301, 2003.

[69] M. Gao, "Debye screening in the QCD gluonic plasma," *Phys. Rev. D*, vol. 41, no. 2, p. 626, 1990.

[70] T. Matsui and H. Satz, "J/ψ suppression by quark-gluon plasma formation," *Phys. Lett. B*, vol. 178, no. 4, pp. 416–422, 1986.

[71] B. Abelev *et al.*, "J/ψ suppression at forward rapidity in Pb-Pb collisions at $\sqrt{s_{\mathrm{NN}}} = 2.76\,\mathrm{TeV}$," *Phys. Rev. Lett.*, vol. 109, no. 7, p. 072301, 2012.

[72] M. Girard, Ł. Graczykowski, M. Janik, A. Kisiel, J. Oleniacz, P. Ostrowski, T. Pawlak, J. Pluta, M. Szymański, and H. Zbroszczyk, "Coherent J/ψ photoproduction in ultra-peripheral Pb-Pb collisions at $\sqrt{s_{\rm NN}} = 2.76\,\text{TeV}$," *Phys. Lett. B*, vol. 718, 2013.

[73] A. Collaboration, "Centrality, rapidity and transverse momentum dependence of J/ψ suppression in Pb-Pb collisions at $\sqrt{s_{\rm NN}} = 2.76\,\text{TeV}$," *Phys. Lett. B*, vol. 734, pp. 314–327, 2014.

[74] A. Adare *et al.*, "J/ψ suppression at forward rapidity in Au+Au collisions at $\sqrt{s_{\rm NN}} = 200\,\text{GeV}$," *Phys. Rev. C*, vol. 84, no. 5, p. 054912, 2011.

[75] A. Kurepin and N. Topilskaya, "Solving the problem of anomalous J/ψ suppression by the MPD experiment on the NICA collider," *The European Physical Journal A*, vol. 52, no. 8, p. 260, 2016.

[76] "Global Λ hyperon polarization in nuclear collisions," *Nature*, vol. 548, no. 7665, pp. 62–65, 2017.

[77] J. Adam *et al.*, "Global polarization of Λ hyperons in Au+Au collisions at $\sqrt{s_{\rm NN}}$ = 200 GeV," *Phys. Rev. C*, vol. 98, no. 1, p. 014910, 2018.

[78] M. S. Abdallah *et al.*, "Global Λ-hyperon polarization in Au+Au collisions at $\sqrt{s_{\rm NN}} = 3$ GeV," *Phys. Rev. C*, vol. 104, 2021.

[79] M. I. Abdulhamid *et al.*, "Global polarization of Λ and $\overline{\Lambda}$ hyperons in Au + Au collisions at $\sqrt{s_{\rm NN}} = 19.6$ GeV and 27 GeV," *Phys. Rev. C*, vol. 108, no. 014910, 2023.

[80] M. Abdulhamid, Aboona *et al.*, "Event-by-event correlation between $\Lambda(\overline{\Lambda})$ hyperon global polarization and handedness with charged hadron azimuthal separation in Au+Au collisions at $\sqrt{s_{\rm NN}} = 27$ GeV from STAR," *Phys. Rev. C*, vol. 108, no. 1, p. 014909, 2023.

[81] C. Alt *et al.*, "Energy dependence of Λ and Ξ production in central Pb+Pb collisions at 20A, 30A, 40A, 80A, and 158A GeV measured at the CERN Super Proton Synchrotron," *Phys. Rev. C*, vol. 78, no. 3, p. 034918, 2008.

[82] K. Adcox *et al.*, "PHENIX detector overview," *Nucl. Instrum. Meth. A*, vol. 499, no. 2-3, pp. 469–479, 2003.

[83] B. B Back *et al.*, "The PHOBOS detector at RHIC," *Nucl. Instrum. Meth. A*, vol. 499, no. 2-3, pp. 603–623, 2003.

[84] M. Adamczyk *et al.*, "The BRAHMS experiment at RHIC," *Nucl. Instrum. Meth. A*, vol. 499, no. 2-3, pp. 437–468, 2003.

[85] https://www.bnl.gov/newsroom/news.php?a=221190.

[86] C. J. Gardner *et al.*, "Operation of the RHIC Injector Chain with Ions from EBIS," Brookhaven National Lab.(BNL), Upton, NY (United States), Tech. Rep., 2015.

[87] J. Alessi *et al.*, "High performance EBIS for RHIC," in *2007 IEEE Particle Accelerator Conference (PAC)*. IEEE, 2007, pp. 3782–3785.

[88] K. Ackermann *et al.*, "STAR detector overview," *Nucl. Instrum. Meth. A*, vol. 499, no. 2-3, pp. 624–632, 2003.

[89] K. C. Meehan, "The fixed-target experiment at STAR," in *Journal of Physics: Conference Series*, vol. 742, no. 1. IOP Publishing, 2016, p. 012022.

[90] M. Beddo *et al.*, "The STAR barrel electromagnetic calorimeter," *Nucl. Instrum. Meth. A*, vol. 499, no. 2-3, pp. 725–739, 2003.

[91] C. Adler, A. Denisov, E. Garcia, M. Murray, H. Stroebele, and S. White, "The RHIC zero degree calorimeters," *Nucl. Instrum. Meth. A*, vol. 470, no. 3, pp. 488–499, 2001.

[92] M. Anderson *et al.*, "The STAR time projection chamber: a unique tool for studying high multiplicity events at RHIC," *Nucl. Instrum. Meth. A*, vol. 499, no. 2-3, pp. 659–678, 2003.

[93] L. Kotchenda *et al.*, "STAR TPC gas system," *Nucl. Instrum. Meth. A*, vol. 499, no. 2-3, pp. 703–712, 2003.

[94] W.-M. Yao *et al.*, "Review of particle physics," *Journal of Physics G: Nuclear and Particle Physics*, vol. 33, no. 1, p. 1, 2006.

[95] P. D. Group, R. Workman, V. Burkert, V. Crede, E. Klempt, U. Thoma, L. Tiator, K. Agashe, G. Aielli, B. Allanach *et al.*, "Review of particle physics," *Progress of theoretical and experimental physics*, vol. 2022, no. 8, p. 083C01, 2022.

[96] H. Jiang, "Strange Hadron (K^0_s, Λ and Ξ) Production in d+Au Collisions at $\sqrt{s_{\mathrm{NN}}} = 200\,\mathrm{GeV}$ at RHIC," Ph.D. dissertation, University of California, Los Angeles, 2005.

[97] H. Bichsel, "A method to improve tracking and particle identification in TPCs and silicon detectors," *Nucl. Instrum. Meth. A*, vol. 562, no. 1, pp. 154–197, 2006.

[98] H. Long, "Mid-rapidity Λ and $\overline{\Lambda}$ Production in Au+Au Collisions at the Relativistic Heavy Ion Collider," Ph.D. dissertation, University of California, Los Angeles, 2002.

[99] M. Zyzak, I. Kisel, and P. Senger, "Online selection of short-lived particles on many-core computer architectures in the CBM experiment at FAIR," 2016.

[100] V. Fine and P. Nevski, *Proc. CHEP*, p. 2000, 2000.

[101] E. Schnedermann, J. Sollfrank, and U. Heinz, "Thermal phenomenology of hadrons from 200A GeV S+S collisions," *Phys. Rev. C*, vol. 48, no. 5, p. 2462, 1993.

[102] R. Barlow, "Systematic errors: facts and fictions," *arXiv preprint hep-ex/0207026*, 2002.

[103] L. Adamczyk *et al.*, "Beam energy dependence of jet-quenching effects in Au+Au collisions at $\sqrt{s_{\mathrm{NN}}} = 7.7, 11.5, 14.5, 19.6, 27, 39,$ and $62.4\,\mathrm{GeV}$," *Phys. Rev. Lett.*, vol. 121, no. 3, p. 032301, 2018.

[104] J. Adams *et al.*, "Scaling properties of hyperon production in Au+Au collisions at $\sqrt{s_{\mathrm{NN}}} = 200\,\mathrm{GeV}$," *Phys. Rev. Lett.*, vol. 98, no. 6, p. 062301, 2007.

[105] B. Abelev *et al.*, "Multi-strange baryon production at mid-rapidity in Pb-Pb collisions at $\sqrt{s_{\mathrm{NN}}} = 2.76\,\mathrm{TeV}$," *Phy. Lett. B*, vol. 728, p. 216, 2014.